Posiva

Modelling Changes in Climate over the Next 1 Million Years

Posiva Oy

January 2020

Modelling Changes in Climate over the Next 1 Million Years

Posiva Oy

January 2020

Posiva

Tekijä(t) – Author(s)

Dr. Natalie S. Lord, Prof. Dan Lunt University of Bristol
Dr. Mike Thorne Mike Thorne and Associates Limited

Nimeke – Title

MODELLING CHANGES IN CLIMATE OVER THE NEXT 1 MILLION YEARS

Tiivistelmä – Abstract

The extended timescales involved in the decay of radioactive wastes to safe levels mean that geological disposal facilities must continue to function effectively long into the future. It is therefore essential to consider long-term climate evolution in post-closure safety assessments in order to evaluate a geological disposal system's response to, and robustness against, a variety of potential environmental changes. In this report, a combination of Earth system modelling techniques has been used to simulate the possible evolution of future climate over the next 1 million years (Myr) for a range of anthropogenic carbon dioxide (CO_2) emissions scenarios. Two of these models calculate future changes in variables that drive climate variations: a carbon cycle impulse response function is used to project the future evolution of atmospheric CO_2 concentration in response to anthropogenic CO_2 emissions, and a conceptual model estimates future changes in global sea level (GSL; as a proxy for the glacial-interglacial cycles) forced by orbital and atmospheric CO_2 variations. A statistical climate emulator is then used to project the future evolution of a number of climate variables forced by atmospheric CO_2 concentration, orbital variations, and global ice sheet volume changes. Finally, a bias-correction downscaling technique is applied to increase the spatial resolution of the climate projections, with a focus on the regions surrounding Olkiluoto, Finland and Forsmark, Sweden. This is also compared to an alternative physical-statistical downscaling technique in order to assess the uncertainty in the downscaled projections.

Future climate is shown to vary in response to the CO_2 (both anthropogenic and natural) and orbital forcings. The period of anthropogenic CO_2 emissions in each emissions scenario is accompanied by a period of warming (along with associated climate changes) which lasts for up to 50 thousand years (kyr) into the future. This is followed by an increased dominance of orbital forcing on climate, and fluctuations between interglacial and glacial states. The results suggest that the timing of the next glacial inception, which is a key climate issue in safety assessments performed for the Olkiluoto and Forsmark sites, may be strongly affected by anthropogenic CO_2 emissions. Scenarios with relatively low emissions are projected to undergo glacial inception in ~50 kyr (from present), whilst relatively high emissions are suggested to extend the current interglacial for approximately 170 kyr after present-day. It should be noted that, based on a comparison of the climate model and palaeo proxy climate data, the SAT projections for glacial conditions that are presented in this report could be considered as worst-case, i.e. if the palaeoclimate that was reconstructed using proxy data is correct then the cooling and associated impacts (e.g. permafrost) may not be quite as severe as projected in this report. The data presented here can be utilized to inform further modelling studies (e.g. landscape, permafrost, surface denudation, etc.) performed as part of a post-closure performance assessment for a radioactive waste repository.

Posiva

Tekijä(t) – Author(s)

Dr. Natalie S. Lord, Prof. Dan Lunt University of Bristol
Dr. Mike Thorne Mike Thorne and Associates Limited

Toimeksiantaja(t) – Commissioned by

Posiva Oy

Nimeke – Title

ILMASTOMUUTOSTEN MALLINNUS SEURAAVAN MILJOONAN VUODEN AIKANA

Tiivistelmä – Abstract

Koska radioaktiivisen, käytetyn polttoaineen hajoaminen turvalliselle tasolle vie pitkän aikaa, maanalaisten loppusijoitustilojen pitää toimia hyvin pitkälle tulevaisuuteen. Tästä syystä loppusijoituslaitoksen turvallisuusperustelussa on tärkeää ottaa huomioon ilmaston muuttuminen pitkällä ajanjaksolla (yhteen miljoonaan vuoteen saakka). Turvallisuusperustelussa tullaan arvioimaan, minkälaisia vaikutuksia erilaisilla mahdollisilla ympäristömuutoksilla on maanalaiseen loppusijoitusjärjestelmään ja miten hyvin järjestelmä kestää näitä muutoksia.

Tässä työssä ilmaston mahdollista muuttumista seuraavien miljoonan vuoden aikana on simuloitu erilaisten mallinnustekniikoiden, sekä erilaisilla ihmisperäisiä hiilidioksidipäästöjä koskevien skenaarioiden, avulla. Eri mallilla arvioitiin, minkälaisia muutoksia tulee tapahtumaan niissä muuttujissa, jotka aiheuttavat ilmaston muutoksia: hiilikierron impulssivastefunktion avulla ennustettiin ihmisperäisten päästöjen aiheuttaman ilmakehän hiilidioksidipitoisuuden tulevia muutoksia, ja konseptuaalisella mallilla arvioitiin maapallon kiertoradan ja ilmakehän hiilidioksidipitoisuuden vaihtelun aiheuttamia tulevia merenpinnan muutoksia maailmanlaajuisesti (jääkausien ja interglasiaalikausien vaihtelun merkkinä). Sen jälkeen ilmastoemulaattorin avulla ennustettiin useiden ilmakehän hiilidioksidipitoisuuden, maapallon kiertoradan vaihteluiden ja maapalloa peittävien jäätikköjen koon muutosten aiheuttamien ilmastomuuttujien tulevaa kehitystä tilastollisen. Lopuksi keskityttiin Olkiluotoa ja Ruotsin Forsmarkia ympäröiviin alueisiin hyödyntäen vääristymää korjaavaa alueellistamistekniikkaa, joka lisää ilmastoennusteiden spatiaalista resoluutiota. Vertailun vuoksi hyödynnettiin myös vaihtoehtoista fyysis-tilastollista alueellistamistekniikkaa alueellisten ennusteiden epävarmuuksien arvioimiseksi.

Ilmaston on osoitettu vaihtelevan tulevaisuudessa hiilidioksidin (sekä ihmisperäisten päästöjen aiheuttaman että luonnollisen) ja maapallon kiertoradan muutosten vuoksi. Kaikissa päästöskenaarioissa ihmisperäisten hiilidioksidipäästöjen kautta seuraa jopa 50 000 vuotta kestävä lämpenemiskausi siihen liittyvine ilmaston muutoksineen. Sitä seuraa kausi, jolloin ilmastoon vaikuttavat lähinnä maapallon kiertoradan muutokset sekä interglasiaali- ja jääkausien vaihtelu. Tulokset viittaavat siihen, että ihmisperäiset hiilidioksidipäästöt saattavat vaikuttaa merkittävästi seuraavan jääkauden alkuun – mikä on olennainen ilmastoon liittyvä seikka Olkiluodossa ja Forsmarkissa tehdyissä turvallisuusarvioissa. Skenaarioissa, joissa päästöt ovat suhteellisen pieniä, jääkauden ennustetaan alkavan noin 50 000 vuoden kuluttua (nykyhetkestä) ja skenaarioissa, joissa päästöt ovat suhteellisen suuria, tämänhetkisen interglasiaalikauden ennustetaan kestävän noin 170 000 vuotta nykyhetkestä. On huomattava, että ilmastomallin ja muinaisilmastoa edustavien ilmastotietojen vertailun perusteella tässä raportissa esitettäviä jääkauden ehtojen SAT-ennusteita voi pitää pahimpana mahdollisena uhkakuvana. Toisin sanoen, jos tietojen perusteella rekonstruoitu muinaisilmasto on todenmukainen, ilmaston jäähtyminen ja siihen liittyvät vaikutukset (kuten ikirouta) eivät välttämättä ole yhtä vakavia kuin tässä raportissa ennustetaan. Tässä annettuja tietoja voidaan käyttää alkutietoina muissa mallinnuksissa (esim. maisema-, ikirouta- ja eroosiomallinnuksissa), joita suoritetaan osana radioaktiivisen jätteen loppusijoitustilan sulkemisen jälkeistä aikaa koskevassa toimintakyvyn arvioinnissa.

TABLE OF CONTENTS

1 CONTEXT

1.1 Background

Posiva is responsible for the final disposal of spent nuclear fuel from the Loviisa and Olkiluoto power plants in Finland, and SKB is responsible for the handling of all nuclear waste produced within Sweden. In 2000, Olkiluoto Island in south-western Finland was selected as the site for final disposal in a deep geological repository. The Forsmark site in south-central Sweden was selected as the location of the spent nuclear fuel repository in 2009.

The significant timescales involved in the decay to safe levels of radionuclides incorporated in radioactive wastes means that geological disposal facilities containing low- and intermediate-level wastes must continue to function effectively for up to 100 kyr. For high-level wastes, including spent nuclear fuel, repositories must remain functional for up to 1 Myr (e.g. SKB 2011). It is therefore essential to consider long-term climate evolution in post-closure performance assessments in order to evaluate a geological disposal system's response to, and robustness against, a variety of potential environmental changes.

 One such environmental change which is crucial to consider is the occurrence of future glacial and periglacial conditions. During past glaciations, the Fennoscandian ice sheet covered both the Olkiluoto and Forsmark sites, resulting in increased land surface erosion and changes to the hydrological and hydrogeological regime in the areas. The formation of permafrost during periglacial conditions is also of interest, particularly regarding the depth below ground level to which it extends. In this context, major uncertainties relate to the impacts of anthropogenic CO_2 emissions on climate, which are explored in the research presented here, and sea level, although this is beyond the scope of this report.

With this in mind, key questions related to long-term climate change at Olkiluoto and Forsmark include:

> (Q1) When will the next glaciation occur?

> (Q2) How might future anthropogenic warming affect climate and the timing of the next glacial inception?

> (Q3) Which climates are possible in the future and how do periglacial, glacial and interglacial climates affect the repositories (geosphere and biosphere)?

This report, whose aims and scope are outlined below, will provide a contribution towards addressing some aspects of these questions.

1.2 Aims and scope

This report presents the results of new research into future climate change occurring over the next million years at the Olkiluoto and Forsmark sites.

Chapter 2 provides an introduction to the modelling of long-term (~1 Myr) climate change. This includes a discussion of the principal forcings of long-term climate change, primarily atmospheric CO_2 and changes in insolation resulting from astronomical variations (Section 2.1); the climate feedbacks (both physical and biogeochemical) which mediate these forcings (Section 2.2); and a summary of previous relevant modelling studies of long-term climate evolution (Section 2.3).

A description of the methodology used to model long-term climate is given in Chapter 3, including the different models used, how they were developed, and the data that they produce. These models include a carbon cycle impulse response function used to project atmospheric CO_2 concentration in response to anthropogenic CO_2 emissions, a conceptual model which estimates future changes in global sea level forced by orbital and atmospheric CO_2 variations, and a statistical climate emulator used to project the future evolution of a range of climate variables forced by atmospheric CO_2 concentration, orbital variations and global ice sheet volume changes. Palaeo-evaluation of the emulator is presented, based on comparing emulated climate changes over the last 800 kyr to palaeo-proxy climate data, as a method of validating the emulator results. Details about the bias-correction and physical-statistical downscaling techniques that were applied to increase the spatial resolution of the emulated climate results are also provided.

Chapter 4 presents the results of the modelling of long-term future climate at Olkiluoto and Forsmark, including the emulator results and the downscaled climate projections. A number of anthropogenic CO_2 emissions scenarios were adopted, with emissions ranging from zero up to a high-emissions scenario. The primary climate variables that are modelled are surface air temperature and precipitation, although a wider range of climate variables have been modelled as part of the project. Climate changes occurring close to the Olkiluoto and Forsmark sites and in the wider European region are examined.

A discussion of the results and comparison to previous studies is provided in Chapter 5, particularly relating to the initiation of the next glacial period. The possible implications of the simulated climate changes for a spent nuclear fuel repository at the sites are also discussed in this chapter. The results of a number of alternative downscaling techniques (including physical-statistical) are compared and the uncertainties discussed, along with the limitations of the overall modelling approach that has been adopted and the uncertainties associated with it.

Finally, a summary of the report and the main conclusions is provided in Chapter 6, along with brief details of the further research that could be carried out following this report.

2 INTRODUCTION TO MODELLING OF LONG-TERM CLIMATE CHANGE

As previously mentioned, the evolution of future climate is critical for the assessment of the safety of long-term disposal of nuclear waste in geological repositories. However, in contrast to climates that occurred in the past, no observational data exist for the future; as such, scientists are reliant entirely on models for their predictions, or, more correctly, alternative projections (or scenarios) under various assumptions, notably in respect to anthropogenic emissions of greenhouse gases. This necessitates a careful consideration of the uncertainties inherent in the projections, which encompass the evolution of atmospheric CO_2 concentrations on both short (10^1–10^2 years) and long (10^4–10^6 years) timescales in response to carbon cycle processes, and the climatic response to CO_2 and variations in Earth's orbital parameters. In this chapter, a summary of the main forcings and feedbacks affecting future climate change occurring on timescales of up to 1 million years is provided (Sections 2.1 and 2.2).

2.1 Forcings of long-term future climate change

2.1.1 Orbital parameters

On timescales of up to 1 Myr, the primary external forcing of the Earth system is variation in incoming solar radiation at the top of the atmosphere. This variation results from changes in the Earth's astronomical parameters, which determine the seasonal and latitudinal distribution of incoming solar radiation (insolation). For example, Figure 1 (bottom panel; Berger 1978, Berger and Loutre 1991) illustrates fluctuations in insolation at 60 degrees North (° N) in June for the last 1 Myr. The key astronomical parameters are eccentricity (the extent to which the orbit of the Earth around the sun is elliptical), obliquity (the angle of the axis of rotation relative to the plane of the orbit of the Earth around the Sun), and the precession (the timing of aphelion or perihelion relative to the vernal equinox). Due primarily to the gravitational effects of other bodies in the solar system, these three astronomical parameters vary on timescales of ~400 kyr and ~100 kyr (eccentricity), ~40 kyr (obliquity), and ~20 kyr (precession). Precession and obliquity modify the latitudinal and seasonal distribution of incoming radiation but do not affect the total global annual mean insolation. Eccentricity affects both the distribution of radiation and the total amount of radiation (albeit to a small degree), and also modulates the precession parameter.
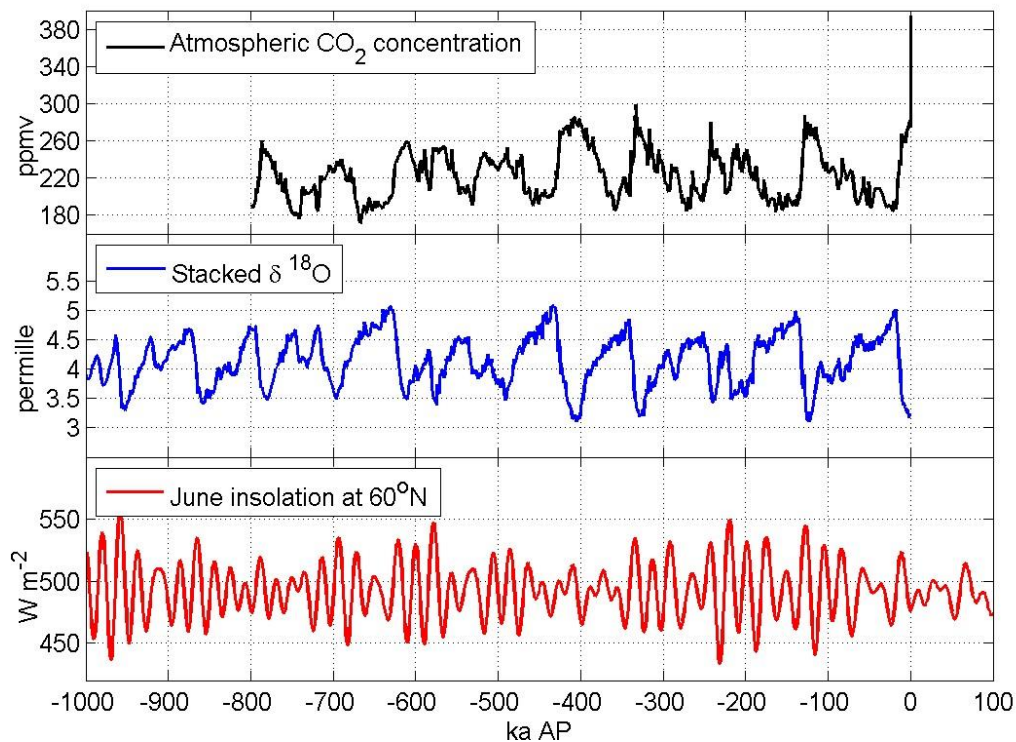
Figure 1. *Top panel: CO₂ composite record for the last 1 Myr (Luthi et al. 2008), and the observed annual average atmospheric CO₂ concentration of 393.8 parts per million by volume (ppmv) in 2012 common era (AD) (www.esrl.noaa.gov). High values of CO₂ correspond to a warmer climate (interglacial state). Middle panel: Stack of 57 benthic oxygen isotope (δ¹⁸O) records for the last 1 Myr (Lisiecki and Raymo 2005), which is used a proxy for global ice volume and temperature. High values of δ¹⁸O correspond to a colder climate (glacial state). Bottom panel: June insolation at 60° N for the last 1 Myr and the next 100 kyr (Berger 1978, Berger and Loutre 1991). Source: Taken from Figure 3.1 (p. 34) of MODARIA Working Group 6 (2016).*

For both the past and future, the development of the three orbital parameters (precession, obliquity and eccentricity) can be calculated with relatively little uncertainty for up to tens of millions of years (e.g. Laskar et al. 2004). For the next ~100 kyr, the eccentricity of the Earth's orbit will be relatively low, which will reduce the impact of precessional changes and will result in obliquity having a greater influence on climate (e.g. Ganopolski et al. 2016). Minima in June insolation at 65° N in the next 100 kyr occur at approximately 16, 53, 77 and 97 kyr after present (AP), making glacial inception more likely around these times. However, as will be discussed later, increased radiative forcing due to higher atmospheric CO_2 concentrations may result in a delay in glacial inception for one glacial cycle or more. After 100 kyr in the future, the eccentricity forcing becomes stronger and precessional changes will begin to have greater influence.

2.1.2 Atmospheric CO_2

As a result of the astronomical forcing, Earth's climate has swung between glacial and interglacial states over at least the last 1 Myr (Figure 1; middle panel; Lisiecki and Raymo 2005), despite the changes in orbital characteristics having a relatively modest impact on global annual mean radiative forcing. The reason for the large response is likely due to positive feedbacks in the Earth system that amplify the seasonal orbital forcing. The primary feedback is associated with the carbon cycle. Ice-core records indicate that glacial periods are associated with relatively low concentrations of CO_2 (Figure 1; top panel; Luthi et al. 2008) and methane (CH_4). Whilst it is believed that several mechanisms are responsible for the CO_2 changes associated with the glacial-interglacial cycles, they are not yet fully understood. Likely contributing effects are physical processes such as temperature dependence of the solubility of CO_2 in the ocean, ocean circulation affecting the lifetime of CO_2 in the ocean, and biogeochemical processes associated with the biological pump, such as iron fertilisation in the Southern Ocean increasing during glacial episodes (See Figure 6.5 of Ciais et al. 2013). Feedbacks associated with the carbon cycle are so poorly understood that it is common practice to consider CO_2 changes in the past as a forcing on the climate system, rather than a feedback, and to impose CO_2 concentrations in long-term palaeoclimate simulations (e.g. Singarayer and Valdes 2010, Ganopolski and Calov 2011, Abe-Ouchi et al. 2013). Furthermore, anthropogenic emissions of CO_2 provide a genuine external climate forcing. Therefore, for the remainder of this report, CO_2 will generally be considered as a forcing on the climate system, although a simple approximation of the feedback between global temperature and atmospheric CO_2 concentration is also calculated in Section 3.1.3.

There is a significant amount of uncertainty relating to the future evolution of atmospheric CO_2 concentration. Firstly, it is not possible to know how anthropogenic CO_2 emissions will develop over the next few hundred years or longer in response to human activities, particularly combustion of fossil fuels, cement production and land use change. However, it is likely that, at least for the next few decades, CO_2 will continue to be released to the atmosphere, and thus the atmospheric CO_2 concentration will continue to increase (IPCC 2013). CO_2 emissions scenarios are often developed for use in modelling studies, based on different assumptions about future socioeconomic developments that aim to cover the range of possible futures. For example, the Fifth Assessment Report (AR5) of the Intergovernmental Panel on Climate Change (IPCC) uses four Representative Concentration Pathways (RCPs), which describe changes in radiative forcing over time, and have different year 2100 radiative forcing values, of 2.6, 4.5, 6.0 and 8.5 Watts per square metre (W m^{-2}) (IPCC 2013). These pathways roughly represent low (RCP2.6), medium (RCP4.5 and RCP6.0) and high (RCP8.5) levels of anthropogenic climate forcing, and extensions to the scenarios also exist that project emissions to 2300 Common Era (AD) (Meinshausen et al. 2011).

Secondly, there is uncertainty about the atmospheric lifetime of emitted anthropogenic CO_2, related to how long it will remain in the atmosphere before it is removed by the natural carbon cycle, thus returning CO_2 concentrations back towards pre-industrial values. There is increasing evidence that a significant proportion will remain in the atmosphere for very long timescales, due to its removal over tens to hundreds of thousands of years by a range of carbon cycle processes (Archer et al. 1997, Archer and

Ganopolski 2005, Lenton and Britton 2006, Ridgwell and Hargreaves 2007). Transient simulations performed using Earth system Models of Intermediate Complexity (EMICs) containing representations of the long-term carbon cycle suggest that, even 10 kyr after CO_2 emissions have ceased, between 15 and 30% of emissions remain in the atmosphere following total cumulative emissions of approximately 200–5000 petagrams of carbon (Pg C; 1 Pg = 10^{15} g) (Eby et al. 2009). It is estimated that, neglecting natural carbon cycle variations, it may take up to 1 Myr or more for pre-industrial CO_2 values to be restored following an anthropogenic CO_2 perturbation (Lenton and Britton 2006, Colbourn et al. 2015), with higher total emissions taking a greater amount of time to be removed. The long-term evolution of an atmospheric CO_2 perturbation is found to be dependent on the total emissions released, rather than the rate of release (Eby et al. 2009), hence the amount of CO_2 released over the coming centuries will affect the lifetime of the perturbation. Based on current emissions trends, CO_2 originating from anthropogenic activities is expected to act as a significant forcing on climate for the next few tens of thousands of years or longer, in combination with variations in the orbital parameters. Notwithstanding this, it is also important to consider scenarios in which humanity carries out large-scale carbon-cycle geoengineering, in which anthropogenic CO_2 is effectively reduced to zero, and the system follows a "natural" trajectory as it would have in the absence of human industrialisation.

A third source of uncertainty is associated with natural variations in the carbon cycle. In the absence of anthropogenic emissions, atmospheric CO_2 concentrations have fluctuated over the past few million years, often demonstrating a strong correlation with temperature (Petit et al. 1999, Luthi et al. 2008). During the late Quaternary, atmospheric CO_2 has varied between ~180 and 280 ppmv on glacial-interglacial timescales (Petit et al. 1999, Siegenthaler et al. 2005, Luthi et al. 2008), and it is expected that fluctuations will continue into the future, although of an unknown magnitude. For reference, pre-industrial concentrations of atmospheric CO_2 were ~280 ppmv, and present day concentrations are just above 400 ppmv (Dlugokencky and Tans 2018).

2.1.3 Other forcings

Other external forcings include palaeogeographical (changes in topography and bathymetry due to plate tectonics) and solar luminosity changes, but these act on much longer timescales than 1 Myr and as such can be neglected (unless the period considered includes a significant change in ocean gateways, such as the closure of the Panama Seaway that occurred in the past). In addition, the 11-year sunspot cycle, and longer timescale luminosity changes, such as those associated with the Maunder Minimum, can also be neglected as they occur on timescales shorter than those of relevance here. A similar comment applies to volcanic forcing, although the possibility of a supervolcano occurring over the timescale of interest is non-zero. Finally, an underlying assumption of all our work is that after the fossil-fuel era, humans will no longer have any direct or indirect effect on climate change.

2.2 Climate feedbacks

There are multiple feedbacks, both positive and negative, that mediate the climate system response to the orbital and CO_2 forcings.

As stated previously, over the last million years the Northern Hemisphere ice sheets (and the smaller Alpine, Himalayan and Patagonian glaciers) have fluctuated in approximate synchrony with CO_2 variations, paced by astronomical forcings. The link between orbital pacing and the glacial cycles is still not well understood, but the essence of Milankovic theory is thought to be broadly correct. That is, that the insolation in Northern Hemisphere summer is critical for determining the state of the Earth system, as this governs the likelihood of snow surviving summer ablation in regions where there is sufficient continental area to build up a large ice sheet. Thus, periods of low summer insolation in the Northern Hemisphere are generally associated with increasing ice volume. However, the system is highly non-linear and state dependent; for example, the Last Glacial Maximum (LGM), one of the periods of greatest ice volume in the last 2 Myr, had similar astronomical forcing to the present day. These ice sheets play an important role in the atmosphere and ocean systems. They affect the radiation balance due to their high albedo (relative to vegetation or bare soil), affect atmospheric circulation directly by their height through modification of Rossby waves and due to their effect on temperature, affect precipitation due to their orography, and can also affect ocean properties and circulation through interaction with the atmosphere and through the input of fresh melt-water. In this report, changes in the ice sheets are represented (through modelling of global sea level, and prescription of appropriate extents and heights in a climate model), and the implications for the two sites are discussed.

Ocean circulation changes also play a role in the Earth system and their effect is important both for regional and millennial-scale variability. Of particular relevance to glacial changes are millennial scale variations in temperature, which are recorded in ice- and marine sediment cores, in particular in the North Atlantic region during the last glacial-interglacial cycle. Antarctic and Greenland ice-cores show a "bipolar seesaw", whereby one pole warms as the other cools or remains at a steady temperature, before the pattern reverses (e.g. Broecker 1998, Stenni et al. 2010). The mechanisms behind these events are not fully understood and are not captured by all model simulations (e.g. Smith and Gregory 2012), but are likely linked to changes in ocean circulation and the strength of overturning in the North Atlantic (Wolff et al. 2009) associated with the inputs of freshwater resulting from the decay of ice sheets. The modelling techniques applied here do not include an interactive ice sheet model, meaning that the impacts of meltwater on ocean circulation are not considered. It is however unlikely that freshwater-driven changes would have a prolonged and significant impact on the projections of Fennoscandian climate at the timescales being considered here. For instance, proxy data covering the period from the LGM to present day show a number of abrupt and short-lived cooling events in the Northern Hemisphere. One theory is that these were caused by a weakening of ocean circulation in the North Atlantic due to a huge and sudden input of freshwater that occurred during the deglaciation of North America following the LGM (e.g. Broecker 2006), although other driving mechanisms have also been suggested. One such event was the Younger Dryas (YD), which occurred ~12.9 kyr BP and lasted for approximately 1 kyr. During this period, proxy data and modelling studies suggest that

SAT in the region of Fennoscandia was several degrees cooler than the relatively warm conditions preceding this, particularly during winter (Renssen and Isarin 2001), resulting in a return to periglacial conditions and the spread of vegetation typically found in cold climates (Vasari 1999). A study by Schenk and Wohlfarth (2019) presented a slightly different reconstruction of climate during the YD, based on analysis of multi-proxy palaeoclimate records from Europe and high-resolution climate model simulations. Their results suggested that, whilst severe cooling occurred in spring, autumn, and winter during this period, summer temperatures in southern Sweden remained relatively high ($\geq$16 °C) due to atmospheric blocking of westerly winds over the Fennoscandian ice sheet during summer. According to ice sheet modelling carried out by Patton et al. (2017) the cooling was accompanied by a "short-lived but dynamic re-advance" of the Fennoscandian ice sheet, lasting for approximately 600 years in the model. Following this, warming during the early Holocene forced terminal retreat of the ice sheet, which finally disappeared at ~8.7 kyr BP.

Other processes such as changes in atmospheric dust likely played some role in shaping the exact nature of the glacial cycles. Dust is known to have varied over these timescales (Mahowald et al. 1999, Lambert et al. 2008) and could interact with the climate system through affecting the albedo of fresh snow (Warren 1984), absorption and/or scattering of radiation in the atmosphere (Tegen 2003), and ocean fertilisation (Jickells et al. 2005) for example. These processes may be very important, but the extent of their effect(s) is much more uncertain than the effects of orbital and CO_2 changes, and their consideration is beyond the scope of this study.

2.3 Previous modelling of long-term future climate change

Many previous studies have addressed the evolution of future climate change, based on various assumptions about future boundary conditions (e.g. CO_2 forcing, ice sheet extents) and using a range of modelling approaches. These studies have focussed on both relatively short timescales of several hundred years, and longer timescales of up to a million years. A range of model complexities have been employed, depending on the length of time and aspect of climate being considered.

In general, results from ensembles of models have only been obtained on timescales of hundreds of years and up to several thousand years. When modelling periods of several hundred years, state-of-the-art Earth System Models (ESMs) and General Circulation Models (GCMs) have been used in the context of the IPCC (e.g. IPCC 2013). These models are the most complex of the range of available models, in terms of the processes and physics included, and have relatively high spatial and temporal resolutions. However, they are extremely computationally expensive and relatively slow, meaning they are more suited to running relatively short transient simulations of several hundred years to a few millennia.

On longer timescales, results from single models, or a small number of models, have been reported. Simulations of up to 50 kyr have often focussed on CO_2-induced climate warming and may ignore orbital forcings (e.g. Mikolajewicz et al. 2007, Charbit et al. 2008, Eby et al. 2009, Zickfeld et al. 2013), whilst those simulations up to 100 kyr have

focussed on the onset of the next glaciation (e.g. Imbrie and Imbrie 1980, Berger et al. 2003, Pimenoff et al. 2011, Tzedakis et al. 2012a, Ganopolski et al. 2016). When modelling timescales of several millennia or longer, reduced complexity models are often employed, such as EMICs. These generally have lower resolutions and include more parameterisations, and consequently require significantly less computing power and time than GCMs, making it feasible to run long-term continuous simulations and large ensembles of simulations. Finally, simulations covering timescales of up to 1 Myr have used EMICs and/or conceptual models to predict future glacial-interglacial cycles (e.g. BIOCLIM 2001, Berger and Loutre 2002, Archer and Ganopolski 2005, Huybrechts 2010). Conceptual models are highly simplified models based on a small number of parameters, and generally do not include any physical processes, which makes them very quick to run. Where GCMs have been applied to assess changes occurring on multi-millennial timescales or longer, "snapshot" simulations have been performed, representing specific future time-slices or climatic conditions (e.g. BIOCLIM 2003b).

As mentioned in previous sections, there are several uncertainties associated with future climate forcings, particularly relating to the future evolution of atmospheric CO_2 concentration. In addition to these, the responses of the Greenland and Antarctic ice sheets (GrIS, AIS) to changes in surface air temperature (SAT) and precipitation are also uncertain, as are the resulting impacts on climate, ocean circulation and global sea level. However, changes in sea level directly driven by changes in the ice sheets are beyond the scope of this work.

As a result of these uncertainties, modelling studies must make a range of assumptions or empirical estimates about the future, which may include, but are not limited to, anthropogenic CO_2 emissions (total emissions and timescale of release), the timing and magnitude of natural CO_2 variations, the evolution of atmospheric CO_2 in response to anthropogenic and natural variations (in the absence of an interactive coupled carbon cycle model), and the response of the ice sheets to climate change (in the absence of an interactive coupled thermodynamical ice sheet model).

Studies of future climate generally agree that mean global temperatures are likely to continue to increase for at least the remaining part of the 21st century, with the ultimate extent and timescale of warming being dependent on future anthropogenic CO_2 emissions and the natural carbon cycle (e.g. Friedlingstein et al. 2006, Collins et al. 2013). On longer timescales, the next glacial inception is generally projected to occur approximately 50 kyr AP under pre-industrial CO_2 concentrations (e.g. Berger and Loutre 2002, Texier et al. 2003, Cochelin et al. 2006, Ganopolski et al. 2016). However, many studies suggest that atmospheric CO_2 concentrations, and thus mean global temperatures, may remain elevated above natural values due to anthropogenic CO_2 emissions for hundreds of thousands of years (e.g. Archer 2005, Colbourn et al. 2015, Lord et al. 2017). This may result in the onset of the next glaciation being delayed for tens of thousands of years or longer, depending on the degree of warming, the effect of which needs to be analysed in assessments of long-term safety for spent nuclear fuel repositories (e.g. Berger and Loutre 2002, Archer and Ganopolski 2005, Ganopolski et al. 2016).

3 METHODS

In this report, long-term climate change is assessed following the framework approach described by Lord (2017). The framework is similar to one developed by Working Group 6 (WG6) of the MODARIA (MOdelling and DAta for Radiological Impact Assessments) international research programme, which was sponsored by the IAEA and ran from 2012 to 2015 (MODARIA Working Group 6 2016). The flow chart that was developed and presented in the final report of WG6 (MODARIA Working Group 6 2016) is illustrated in Figure 2. It shows how different climate models can be applied to investigate climate changes occurring over different timescales in the context of post-closure radiological impact assessments for nuclear waste repositories. Due to the relatively long timescales being considered here, i.e. hundreds of thousands of years and longer, the right-hand branch of the chart in Figure 2 is applicable, which is highlighted in red. These highlighted steps generally follow a similar methodology to previous studies of long-term climate change, by using EMICs to model a larger ensemble of simulations sampling different future conditions and/or transient simulations, before using GCMs to simulate a smaller number of particular climate states of interest.

The flow chart shown in Figure 2 was modified and updated by Lord (2017), before being further developed in the present study. The updated framework for addressing long-term climate change that is applied in this report is presented in Figure 3. The three columns represent the main forcings on climate that are relevant on the timescales of interest for the disposal of radioactive wastes (from several thousand years up to 1 Myr), being atmospheric CO_2 concentration (left column) and orbital variations (right column), which were discussed in Section 2.1. Global ice volume, in the form of global sea level, is also represented (central column). Whilst it is not strictly a climate forcing because periods of glaciation are thought to result in a negative feedback with atmospheric CO_2 (see Section 2.1.2), it acts as a forcing on emulated climate, since the emulator (and underlying GCM) are unable to explicitly model changes in the continental ice sheets. Changes in global ice volume, and thus glacial-interglacial cycles, must therefore be prescribed, following the methodology presented in Section 3.1.3.
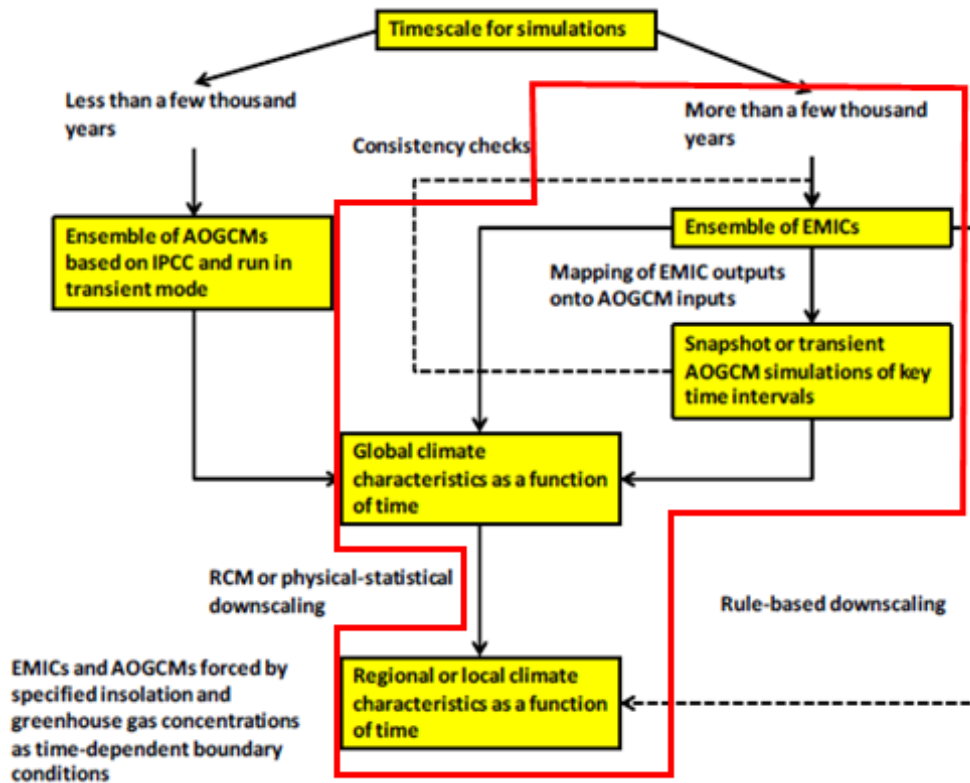
Figure 2. *Selection of climate models for use in post-closure radiological impact assessments for nuclear waste repositories. The red box indicates the steps addressed in this report. Source: Modified from Figure 4.1 (p. 47) of MODARIA Working Group 6 (2016), and taken from Figure 1.7 (p. 29) of Lord (2017).*

The blue boxes in Figure 3 represent the modelling tools applied in this study. Two were developed and described by Lord (2017) and accompanying publications, being a carbon cycle impulse response function (Lord et al. 2016, Lord et al. 2015), and a climate emulator (Lord et al. 2017). Other tools that were utilized here include a CGSLM and regression analysis, both of which are described in more detail in Section 3.1.3. When used together, these tools can be applied to produce the climate data required for post-closure safety assessments for nuclear waste repositories, represented by the yellow box. Due to the modelling approach used, this can be climate data for a specific point in time, or data projecting the continuous evolution of climate over a longer time period. It can also be in the form of climate data for the whole global grid, or for a specific grid box. The advantages and limitations of each of these tools, as well as the climate data that they can produce, are discussed in detail in the relevant publications (Lord et al. 2016, Lord et al. 2017) and in Section 5.4.
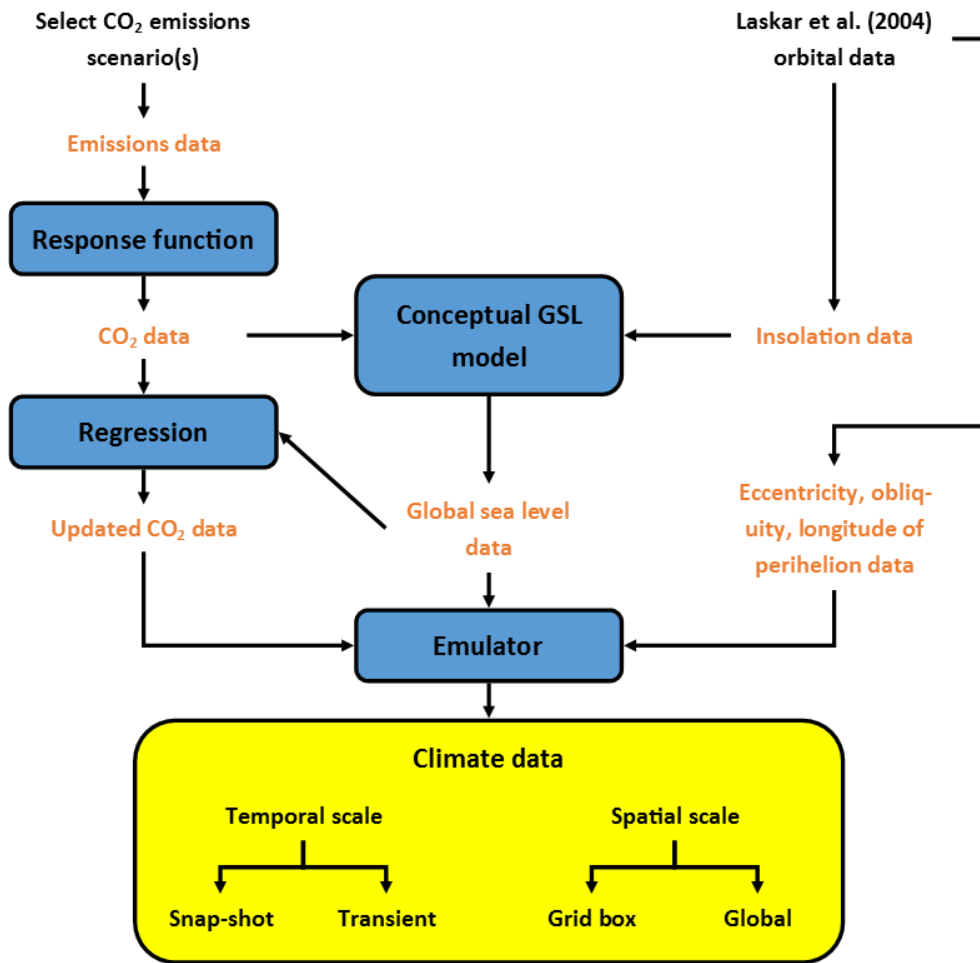
Figure 3. Framework utilized for addressing long-term climate change in the context of post-closure performance assessments for radioactive waste repositories. Source: Modified from Figure 1.8 (p. 30) of Lord (2017).

3.1 Climate forcing data for the next 1 Myr

The primary tool used for projecting the evolution of long-term future climate is the climate emulator, which is described in full detail in Lord et al. (2017). Briefly, this is a statistical model that is calibrated on data from a more complex climate model, in this case a GCM. It gives a projection of the climate resulting from a certain set of input conditions (climate forcings), along with an estimation of the uncertainty associated with the projection. In this case, the climate forcings that are applied are atmospheric CO_2 concentration, orbital parameters, and GSL; for one single combination of values for these forcings, the emulator simulates the corresponding state of a particular climate variable, such as SAT. This is carried out for the full 1 Myr time period, giving a projection of climate evolution covering a significantly longer timescale than could be achieved using a conventional GCM.

In order to run the emulator, a number of steps needed to be completed first, shown in orange text in Figure 3. Broadly, these steps provided the future climate forcing data,

including atmospheric CO_2 concentration, orbital data and global sea level data. Each of these steps will be described in more detail in the following sections. It should be noted that the previously published research describing the emulator methodology used four input dimensions (climate forcings) (Lord et al. 2017). These were atmospheric CO_2 concentration and the three main orbital parameters of longitude of perihelion, obliquity and eccentricity. The methods used to produce this data for these four variables are detailed in the referenced publications. However, here, an additional fifth input variable was used which represents the glacial-interglacial cycles – global sea level (as a proxy for global ice volume). The approach that was adopted to calculate this data, and the emulator configuration used, have not been described or published anywhere other than this report at the time of its writing.

3.1.1 Atmospheric CO_2

In order to produce a time series of future atmospheric CO_2 concentration data to use as a climate forcing in the emulator, several IPCC CO_2 emissions scenarios were selected, and then the carbon cycle impulse response function was used to project the long-term response of atmospheric CO_2 concentration to the prescribed emissions. The results of the impulse response function are described in Section 4.1.

CO_2 impulse response function

As mentioned previously, a carbon cycle impulse response function (IRF), which is fully described in Lord et al. (2016), was used to produce future atmospheric CO_2 concentration data. The response function was developed based on an ensemble of simulations run using the *c*GENIE EMIC, with total anthropogenic CO_2 emissions ranging from 1000 Pg C to 20,000 Pg C. Based on a user-prescribed CO_2 emissions scenario, the response function calculates the response of atmospheric CO_2 concentration to the emissions over a specified time period (e.g. 1 Myr). In general, for scenarios with anthropogenic emissions, the CO_2 concentration is projected to increase during the emissions period, before gradually decreasing back towards the pre-industrial atmospheric CO_2 concentration (~280 ppmv) over the course of the simulation, as various carbon cycle processes draw excess CO_2 down from the atmosphere. This return towards pre-industrial values was prescribed in the response function, which was itself based on the results of the *c*GENIE model. For a detailed description of the relevant carbon cycle processes and their impact on an atmospheric CO_2 perturbation please see Lord et al. (2016).

CO_2 emissions scenarios

The anthropogenic CO_2 emissions scenarios that were selected constitute the RCP scenarios used in the IPCC's AR5 (IPCC 2013). The RCP pathways describe changes in radiative forcing over time, driven by all anthropogenic forcing agents, including CO_2, methane, and aerosols. The pathways have different year 2100 radiative forcing values, of 2.6, 4.5, 6.0 and 8.5 W/m^2, roughly representing low (RCP2.6), intermediate (RCP4.5 and RCP6.0) and high (RCP8.5) levels of anthropogenic climate forcing. Here, only the CO_2 component of the radiative forcing pathways was taken into account; all other anthropogenic forcings are kept constant at pre-industrial values. Extended versions of the scenarios were used which project CO_2 emissions to 2500 AD, and RCP6 was

excluded due to an intermediate scenario being represented by RCP4.5. Meinshausen et al. (2011) provide a detailed description of the extended RCP scenarios, including the original references for each of the scenarios. Briefly, emissions follow the IPCC's AR5 scenarios to 2100 or 2150 AD (depending on the scenario), followed by a smooth transition either to constant negative emissions (in the case of RCP2.6) or constant atmospheric CO_2 concentrations (for the other scenarios). These constant conditions persist until 2500 AD, after which emissions are set to zero in all scenarios.

Between the years 2000 and 2500, total CO_2 emissions of approximately 5000 Pg C are released in the RCP8.5 scenario, and ~1000 Pg C in RCP4.5. For RCP2.6, ~440 Pg C are emitted followed by negative emissions of 370 Pg C, resulting in total net emissions by 2500 AD of ~70 Pg C. These total emissions for the three scenarios are in addition to the fossil fuel carbon emissions released since 1750 AD of approximately 350 Pg C. To put these values into context, remaining fossil fuel reserves that are currently potentially technically and economically viable have been estimated to be approximately 800 Pg C (McGlade and Ekins 2015). However, fossil fuel resources (where economic extraction may be feasible in the future, not including fossil fuel reserves) are estimated at ~2200 Pg C (McGlade and Ekins 2015), and nonconventional resources such as methane clathrates could be as high as 20–25,000 Pg C (Rogner 1997). It should be noted that estimates of fossil fuel resources may vary significantly between different sources, and that the values quoted in this report are relatively low compared to some other estimates (for example, BGR 2012, IEA 2011, 2013, Rogner et al. 2012). Some of the reasons for this discrepancy are discussed in McGlade and Ekins (2015), and include differences in the definitions of "reserves" and "resources" between sources, variations in whether certain categories of fossil fuel are included in the estimate, and issues associated with a lack of reliable estimates of the potential resources of certain categories of fossil fuels and differences in methods of estimation. Considering the significant reserves of fossil fuels still available, the worst-case emissions scenario presented here was selected so that the emissions pathway that ultimately is followed will likely be bounded by this scenario.

A "natural" CO_2 scenario was also adopted, which assumes no anthropogenic CO_2 emissions, resulting in a constant pre-industrial atmospheric CO_2 concentration of 280 ppmv. This was included to allow comparison of the natural evolution of the climate system to its evolution following various CO_2 emissions pathways. It can also be considered as representing a scenario under which carbon dioxide removal (CDR) geoengineering takes place to such an extent that pre-industrial CO_2 is recovered.

The carbon cycle impulse response function was used to calculate the evolution of atmospheric CO_2 concentration based on these four emissions scenarios, which is illustrated in Figure 4a. Atmospheric CO_2 reaches a peak within the first 1 kyr (i.e. immediately following the emissions period) in the three anthropogenic emissions scenarios, with a maximum of 1358 ppmv for the RCP8.5 scenario. It should be noted that the maximum atmospheric CO_2 concentration projected by the response function for RCP8.5 was 1971 ppmv, reached in year 2234. However, due to the 1 kyr temporal resolution of the emulator, this maximum is not captured in the emulation of future climate. However, atmospheric CO_2 would only be at this very high level for a relatively short period of time (hundreds of years) compared to the timescales being considered here, since atmospheric CO_2 declines relatively rapidly immediately following the

emissions period, and then more slowly over longer timescales of hundreds of thousands of years. At 1 Myr AP, the atmospheric CO_2 perturbation has almost entirely decayed in all scenarios, restoring the CO_2 concentration to 282 ppmv in the RCP8.5 scenario, close to pre-industrial values. These projections calculated using the response function do not account for the impact of future glacial cycles on CO_2, which is addressed in Section 3.1.3.

3.1.2 Orbital variations

As discussed in Section 2.1.1, the three main orbital parameters of longitude of perihelion (ϖ), obliquity (ε), and eccentricity (e) can act as significant forcings on climate over long timescales. The future evolutions of these astronomical parameters were calculated using the solution of Laskar et al. (2004), and are described in Section 4.1. As in Lord et al. (2017), longitude of perihelion and eccentricity were combined under the forms $e\sin\varpi$ and $e\cos\varpi$ for input into the emulator.

3.1.3 Global sea level

The fifth and final climate forcing used in the emulator essentially aims to capture the transition of the Earth system through the glacial-interglacial cycles. A full cycle may involve the expansion and retreat of the existing GrIS and AIS, as well as the northern European and North American ice sheets that have formed during past glaciations. The emulator requires a single value for each input variable for each time slice that is to be emulated, such as a single atmospheric CO_2 concentration or obliquity value. Consequently, global ice volume is chosen to represent the glacial-interglacial cycles, and for simplicity global sea level (also termed eustatic sea level) is used as a proxy for this.

Conceptual GSL model (CGSLM)

To calculate the future evolution of GSL, a conceptual GSL model (CGSLM) was developed. This relatively simple model is based on the insolation threshold model of Archer and Ganopolski (2005), which itself was developed from the model of Paillard (1998). The model predicts transitions between three climate regimes: interglacial, mild glacial, and full glacial. The forcing for the model is summer insolation (averaged between June 21 and July 20) at 65° N as computed by Laskar et al. (2004), which has been normalized to zero mean and unit variance. Transitions between the climate regimes occur when the insolation forcing crosses different thresholds, and are also assumed to be affected by the calculated ice volume. The value of the critical insolation (i_0) threshold that results in initiation of a glaciation is dependent on atmospheric CO_2 concentration, and is calculated using a relationship derived from simulations run using the CLIMBER-2 EMIC (Archer and Ganopolski 2005). The model contains a total of eight tunable parameters, which are detailed in Table 1. The forcing data for the CGSLM and the critical insolation threshold to initiate a glaciation (i_0) are illustrated in Figure 4, for the period 500 kyr BP (before present) to 1 Myr AP. The impact of anthropogenic CO_2 on the value i_0 can clearly be observed, when the constant threshold value of the natural scenario is compared with the future thresholds for the RCP scenarios (Figure 4b), which

are highly perturbed over the first 50 kyr AP or so due to the relatively high atmospheric CO_2 concentration over this period (Figure 4a).

Whilst the model calculates the global ice volume, this data was converted to global mean temperature, in order to evaluate the results of the CGSLM as well as to account for the radiative forcing impact of anthropogenic atmospheric CO_2 perturbations. Temperature was derived following a similar approach to Archer and Ganopolski (2005); by scaling the global ice volume data to the difference between LGM and pre-industrial global mean temperature, estimated to be approximately 4 °C (Annan and Hargreaves 2013). For future temperature, the anthropogenic temperature forcing was added to the glaciation forcing, using a climate sensitivity ΔT_{2x} of 3 °C for a doubling of CO_2, following the methodology of Archer and Ganopolski (2005). For reference, the most recent IPCC report suggested that the likely range for equilibrium climate sensitivity is 1.5 °C to 4.5 °C (IPCC 2013), whilst Cox et al. (2018) suggested a central estimate of 2.8 °C (2.2 – 3.4 °C) based on an ensemble of climate models. Thus 3 °C represents the approximate middle point of these ranges. It should be noted that changing these values of 3 °C (climate sensitivity) and 4 °C (LGM temperature) does not have a large impact on emulated climate as the temperature data is not used to directly force the emulator. Instead, these values are used to scale the output of the CGSLM to temperature, meaning that the maxima and minima do not change, but the intermediate values may vary slightly. This scaling is necessary as it allows the glacial-interglacial variations and the anthropogenic perturbation to be combined, but the parameter values used do not affect the projected timing of glacial-interglacial cycles. The actual sensitivity of the Earth system to changes in radiative forcing that is simulated by the emulator is defined by the climate sensitivity in the underlying GCM.

Table 1. *Description of the eight tunable parameters in the CGSLM.*

Parameter	Description
1	Time constant for interglacial regime (*ig*)
2	Time constant for mild glacial regime (*g*)
3	Time constant for full glacial regime (*G*)
4	Time constant
5	Truncation parameter
6	Initial ice volume of model
7	Insolation threshold for ig to g transition (*i_0*)
8	Insolation threshold for G to ig transition (*i_1*)

The evolution of palaeo- and future global temperature anomaly (compared with pre-industrial) is presented in Figure 5a. Also shown on this figure is past global temperature estimated from palaeo $\delta^{18}O$ data (Lisiecki and Raymo 2005), which has also been scaled to the difference between pre-industrial and LGM temperature. These data were used as a comparison in order to evaluate the results of the CGSLM, following the approach of Archer and Ganopolski (2005), to ensure that the model is capturing the timing and variability of the past glacial cycles.
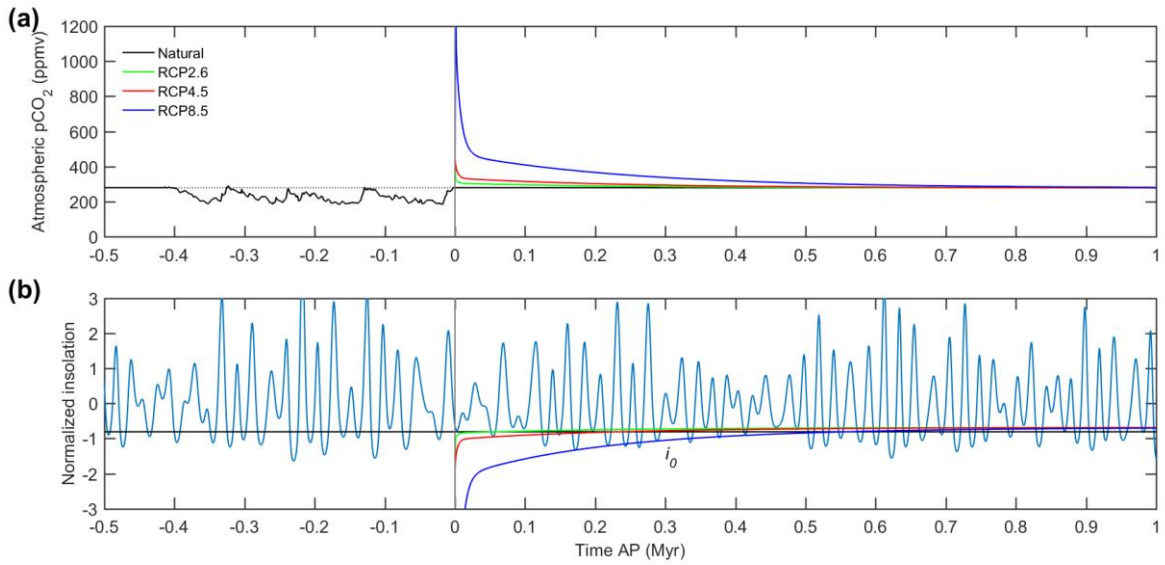
Figure 4. *Climate forcing data used as input to the CGSLM for the last 500 kyr and the next million years. (a) Time series of observed past atmospheric CO_2 concentration (ppmv) (Luthi et al. 2008), and projected future atmospheric CO_2 concentration for the natural (black line), RCP2.6 (green line), RCP4.5 (red line), and RCP8.5 (blue line) emissions scenarios, calculated using the carbon cycle impulse response function of Lord et al. (2016). The pre-industrial CO_2 concentration is also shown (grey dotted line). (b) Time series of normalized summer insolation at 65 °N (light blue line) (Laskar et al. 2004). Also shown is the critical insolation threshold (i_0) for the global response function for the past (black line) and for the future for the four emissions scenarios (green, red, and blue lines).*
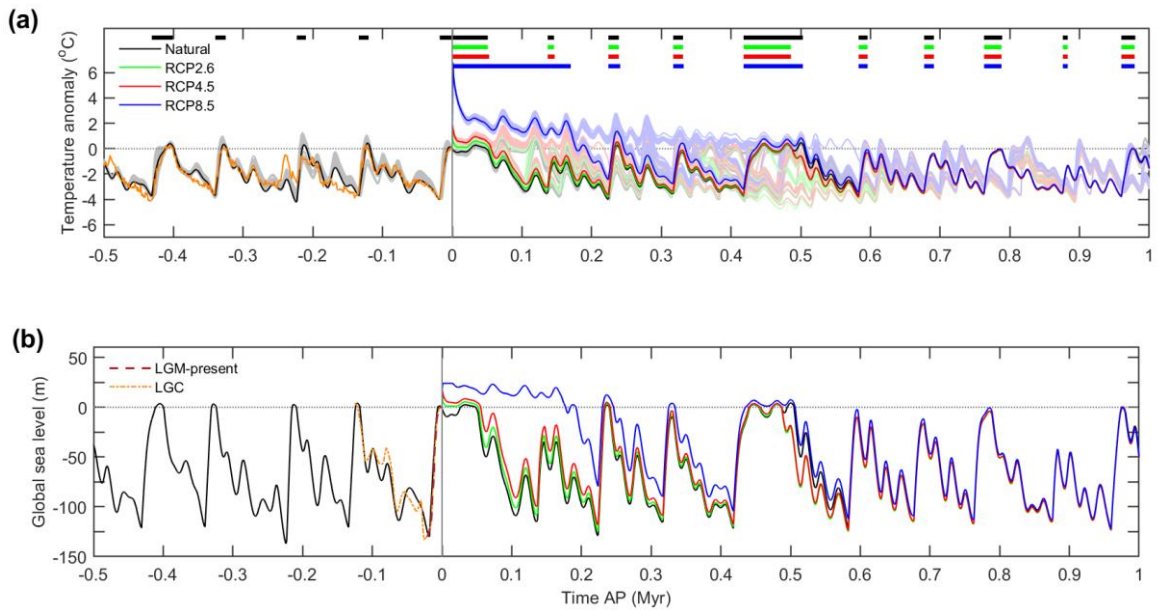
Figure 5. Climate results produced by the CGSLM for the last 500 kyr and the next million years. (a) Time series of the global temperature anomaly (°C) for the natural (black line), RCP2.6 (green line), RCP4.5 (red line), and RCP8.5 (blue line) emissions scenarios, calculated using the CGSLM. The darker coloured lines represent the tuned model configuration that best matched the global temperature data estimated from palaeo proxy data (orange line) (Lisiecki and Raymo 2005). There is one lighter coloured line for each of the other model configurations that also reproduced the proxy temperature data at least as well as the independently tuned version. Due to the density of the lines, these sometimes appear as a shaded band. The differences in the projections represented by the light and dark lines are explained in the main text. Periods of interglacial conditions for each emissions scenario as projected by the CGSLM are indicated by thick horizontal bands in the upper part of the panel. (b) Time series of global sea level (m) for the past (black line) and for the future for the four emissions scenarios, calculated using the CGSLM (based on the tuned model configuration). Also shown is reconstructed GSL for the last glacial cycle (LGC; orange dotted line; 120–0 kyr BP) (Singarayer and Valdes 2010), and for the LGM to present day (brown dashed line; 21–0 kyr BP) (Singarayer and Valdes 2010).

In order to assess the sensitivity of the model to the fitted parameter values of the CGSLM, a sensitivity analysis was carried out in two parts. Firstly, a range of values for each of the fitted parameters were systematically selected, and the model was then run with one parameter being varied at a time (i.e. independently). The model simulations were evaluated by comparison to the proxy data for the LGM (Lisiecki and Raymo 2005), shown in Figure 6. Each panel of this figure represents one of the eight parameters described in Table 1, and shows the systematically-sampled range of values that were tested (normalized to between 0 and 1 for visual comparison). The performance of each simulation was assessed by comparing the projected ice volume at the LGM to that reconstructed from palaeo proxy data, and the timing of the maximum global ice volume during the LGM, estimated to have occurred at approximately 18 kyr BP based on the palaeo data (Lisiecki and Raymo 2005). The projected temperature data for the last 500 kyr for the simulations was also compared to the reconstructed temperature proxy data (Lisiecki and Raymo 2005) and the root mean squared error (RMSE) was calculated. The results of the best performing model configuration with the lowest RMSE are represented by the solid markers on Figure 6.
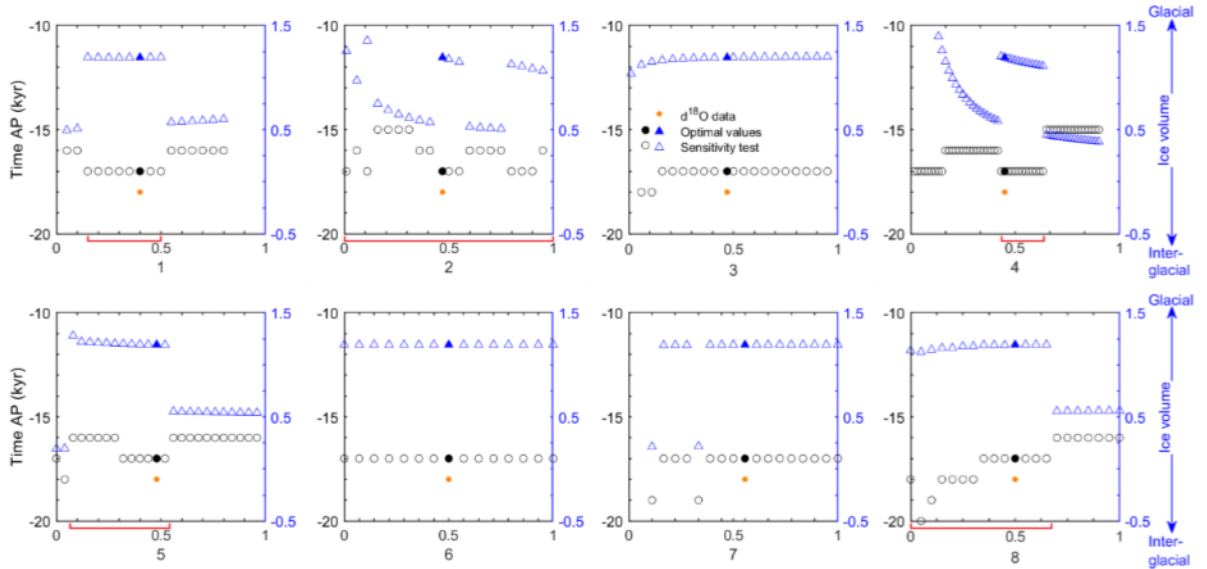
Figure 6. Sensitivity analysis of eight parameters from the CGSLM. Parameter values were varied, and the sensitivity of the timing of the LGM (left axes; black; kyr) and modelled ice volume at the LGM (right axes; blue; values between approximately 0 and 1.5, where >1 represents full glacial conditions, ~0.5 represent mild glacial conditions, and ~0 represents present-day interglacial conditions). Solid black and blue markers represent the optimal parameter values based on the parameters being optimised independently and systematically, selected because they provided the closest match to the palaeo proxy $d^{18}O$ temperature data (Figure 5a, orange line). The timing of the LGM as estimated from this palaeo proxy data is also shown (left axes; orange) (Lisiecki and Raymo 2005). Parameter values have been normalised to between 0 and 1 to facilitate visual comparison. Red lines highlight the parameter ranges for variables 1,2,4,5,8 that were applied in the LHC sampling during further testing of the sensitivity of the model. The 8 parameters are: (1) time constant for interglacial regime (i), (2) time constant for mild glacial regime (g), (3) time constant for full glacial regime (G), (4) time constant, (5) truncation parameter, (6) initial ice volume in model, (7) insolation threshold for ig-g transition (i_0), (8) insolation threshold for G-ig transition (i_1).

Based on this initial sensitivity analysis, the model was found to be reasonably robust to the parameters, with generally small changes to projected temperature resulting from varying the parameter values within a reasonably wide range, as evident in Figure 6. Varying the values of the parameters had a limited impact on the timing of the LGM, represented by black markers, generally shifting it by 1 or 2 kyr. The modelled ice volume was slightly more sensitive to certain parameters, although demonstrated a similar pattern of change to the timing of the LGM, with the model switching between several distinct states (here, mild glacial and full glacial) as the parameter values changed, as seen for parameters 1, 2, 4, 5, and 8 in Figure 6. This type of model sensitivity, which features distinct states, means that nearly identical results may be produced for a range of parameter values, and tuning to palaeo proxy data (as performed here) can be used to identify parameter values which produce unrealistic results, such as projecting mild glacial rather than full glacial conditions at the LGM (e.g. Figure 6, parameter 1). The model was generally not sensitive to the values of parameters 3, 6, and 7, with large ranges in their values having little or no impact on the modelled projections of ice volume at the LGM, a trend that was also to be true for other time periods. This robustness to the parameters was also found by Paillard (1998) for his similar model. He also found that using different insolation forcing data did not have a large impact on the results.

In order to further assess the sensitivity of the model, the parameters that were found to have a significant impact on the model results (parameters 1, 2, 4, 5, and 8) were then varied randomly and concurrently (i.e. a multivariate sensitivity analysis, as opposed to the univariate, independent analysis). Latin hypercube (LHC) sampling was used to produce one thousand different sets of values for the five parameters. Figure 6 was used to identify the range of values to be sampled for each parameter, highlighted by the red lines. LHC sampling is a method of efficiently sampling a parameter space, and in this case produces one thousand different values for each of the parameters, which are then randomly combined to give one thousand sample sets, each containing one value for each of the five parameters. The LHC sampling function also includes an option to maximise the minimum distance between all pairs of points (the maxi–min criterion), which is utilised here to ensure the set of sensitivity experiments is optimally space filling.

The CGSLM was then run using each sample set in turn, and the model results again evaluated by comparison to the palaeo proxy data for the last 500 kyr (Lisiecki and Raymo 2005). Firstly, the projected ice volume at the LGM was considered, and any simulations that projected mild glacial conditions at this time were excluded. Based on the proxy data, the maximum ice volume during the LGM was estimated to occur at ~18 kyr BP, as shown in Figure 6. Therefore, any simulations which projected the LGM maximum to be greater than 1 kyr before or after this year were also excluded; for reference, it can be seen from Figure 6 that the best performing model from the first stage of the sensitivity assessment, during which the parameters were optimised independently of each other, projected the maximum ice volume to occur at 17 kyr BP. Following this, any simulations with a RMSE greater than that of the independently-optimised model configuration were also excluded. This resulted in ninety simulations from the original thousand being retained, and the temperature projections for these ensemble simulations are shown by the lighter lines on Figure 5a, illustrating the sensitivity of the projected temperature to the parameters. The model configuration with the lowest RMSE that best matched the palaeo data was selected

as the optimal version and was used in the remainder of this report; the results of this are represented by the darker coloured lines on Figure 5a.

For the last 500 kyr, it can be seen that the optimally tuned model does a reasonably good job of reproducing the proxy data, and that the other sensitivity simulations produce fairly similar results, particularly in terms of the timing of the glacial cycles (Figure 5a). In the future, however, the spread of temperature projections is larger, with different parameter sets resulting in different timings for glacial and interglacial conditions, although several distinct temperature pathways followed by multiple scenarios are evident, presumably associated with similar parameter values as also seen to occur in Figure 6. The difference in future pathways is a result of varying the parameters, which control settings in the model such as insolation thresholds for moving between different climate states and minimum lengths of time that the model must remain in a certain state before moving to the next. The period between approximately 300 and 500 kyr AP appears to be particularly sensitive to the parameters, with several different pathways for each emissions scenario. At this time insolation variations are relatively small, meaning that several of the insolation minima during this period come close to the insolation threshold for triggering a mild glacial (Figure 4b), as well as potentially the other insolation thresholds. As a result, relatively small variations in the model parameters may mean that a threshold is or is not passed, leading to significantly different future projections. In the same way, it can be seen that the optimal ensemble member diverges from many of the others between ~680 kyr AP and 960 kyr AP, as do other ensemble members at other times (e.g. 520 to 580 kyr AP). This is a result of the relative simplicity and threshold nature of the conceptual model, and given that the future evolution of temperature is not known, the tuned model configuration that best reproduced the palaeo data was selected as the final model. Overall, it was found that the final tuned model is able to reproduce the approximate 100 kyr cycles in global temperature observed in the proxy data for the last 500 kyr, including the approximate timings and magnitudes of the variations.

This global temperature anomaly data was then converted into GSL, which was used as input to the emulator. This was achieved using a similar approach to the conversion of CGSLM output to global mean temperature performed earlier. In this case, however, the temperature data was scaled according to GSL data for the period of the LGM to present day from Singarayer and Valdes (2010). These palaeo GSL reconstructions for the last 21 kyr were calculated based on the ICE-5G model of Peltier (2004), with a rise in GSL indicating ice sheet retreat, whilst a lowering of GSL is a sign of ice sheet growth. According to these reconstructions, the maximum GSL drop over this period occurred at the LGM (21 kyr BP) and is estimated to be approximately -130 m compared with present-day sea level. Hence, the temperature at the LGM was assigned a GSL value of -130 m, both the temperature and GSL at present-day were assigned a value of 0 because these variables are an anomaly compared to present-day, and all other values were scaled linearly around this anomaly (0 to -130 m). As a consequence of the global temperature data being used to derive GSL, the future GSL data also includes an estimate of the forcing from anthropogenic CO_2.

Future GSL changes occurring in response to anthropogenic CO_2 forcing were capped at +24 m. Various studies have investigated the possible impact of anthropogenic climate change on the stability of the continental ice sheets, generally suggesting that warmer

climate conditions persisting for a long period of time could result in significant melting of the GrIS and West Antarctic ice sheet (WAIS) over timescales of 10^3–10^4 years (Charbit et al. 2008, Stone et al. 2010, Winkelmann et al. 2015). There is more uncertainty associated with the response of the East Antarctic ice sheet (EAIS). Several studies have suggested that it may be relatively stable, making it unlikely to undergo significant retreat in response to anthropogenic warming (e.g. Pollard and DeConto 2009, Huybrechts and de Wolde 1999, Huybrechts et al. 2011), whilst others contradict this conclusion (e.g. Clark et al. 2016, Rignot et al. 2019), projecting, for example, that significant melting of the EAIS following high CO_2 emissions (~5000 PgC) could result in an increase in global sea level of ~ 50 m by 10 kyr AP (Clark et al. 2016). The PRISM4 Pliocene reconstruction of the continental ice sheets (Dowsett et al. 2016) was used as the basis for the reduced ice sheet (*lowice*) HadCM3 simulations which were presented in Lord et al. (2017) and are used here as calibration data for the emulator. These ice sheet configurations were estimated to be accompanied by ~24 m of GSL rise (Dowsett et al. 2016), hence this value was adopted as the maximum GSL rise resulting from melting of the GrIS and WAIS. Figure 5b shows GSL from 500 kyr BP to 1 Myr AP, as calculated for the four emissions scenarios by the CGSLM. Also shown is reconstructed GSL for the last glacial cycle (120 kyr BP to present day) (Singarayer and Valdes 2010), and for the LGM (21 kyr BP) to present day, on which the global temperature data from the CGSLM was scaled. A summary of the different data processing steps carried by the CGSLM is shown in Figure 7, and the results of the model are discussed in more detail in Section 4.1.

GSL threshold approach

In the results for future climate presented later in Section 4.2.2, periods when the ice sheet is projected to be covering the Forsmark and Olkiluoto repository sites are highlighted, which were calculated using a relatively simple threshold approach. In order to validate this threshold method, it was applied to the Last Glacial Cycle, covering -120 to 0 kyr AP, as illustrated in Figure 8. Using this method, periods of higher confidence ice coverage (purple bands in Figures 8b and 8c) were calculated by identifying the highest GSL for which ice is present at the sites in the Singarayer and Valdes (2010) ensemble, which was -73 m, and then assuming that future periods with sea level lower than this threshold (minus 20 m to account for uncertainty in the threshold) have ice present at the site in question. The higher confidence GSL threshold was therefore -93 m. Periods of lower confidence ice coverage were also identified (cyan bands), which had GSL values greater than the higher confidence threshold, but lower than the lowest GSL with no ice coverage at the sites in the Singarayer and Valdes (2010) ensemble (-46 m). For this, 20 m was added on to the value of -73 m (highest GSL in simulations with ice present at sites), resulting in a lower confidence GSL threshold of -53 m. It is more uncertain whether the sites were ice covered during these periods, as the actual threshold for ice coverage is not well-defined – it lies between -46 and -73 m according to the Singarayer and Valdes (2010) ensemble. This means that the maximum possible uncertainty in the threshold value, based on the Singarayer and Valdes (2010) reconstruction, is 27 m. As such, we take ±20 m as a representative measure of the uncertainty in the threshold. The ice sheet extents corresponding to -46 m and -73 m are illustrated in Figure 9, and show the expansion of the ice sheet over the two sites.
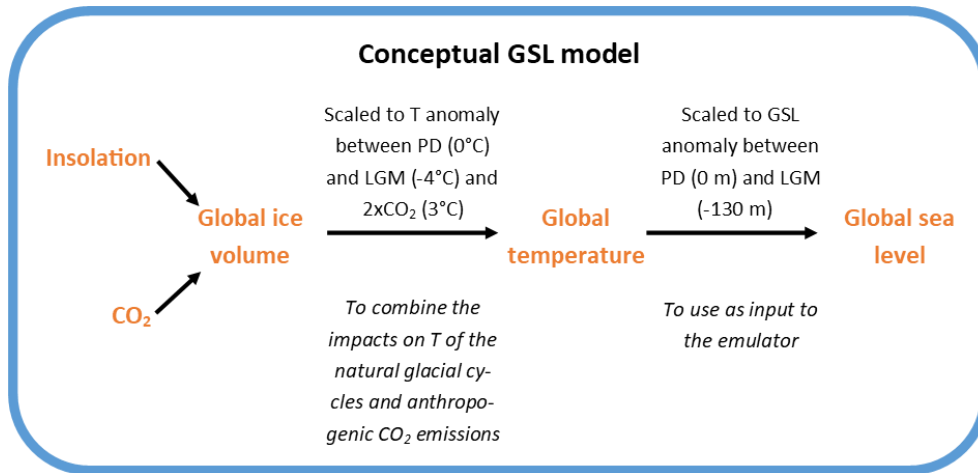
Figure 7. *Data processing steps carried out within the CGSLM. Insolation and CO_2 data were provided as input to the model, which output global ice volume data. This was then converted to global temperature anomaly (°C; T), which was then converted to GSL. The motivations for the conversions are detailed in italic text. Acronyms are present-day (PD) and Last Glacial Maximum (LGM).*
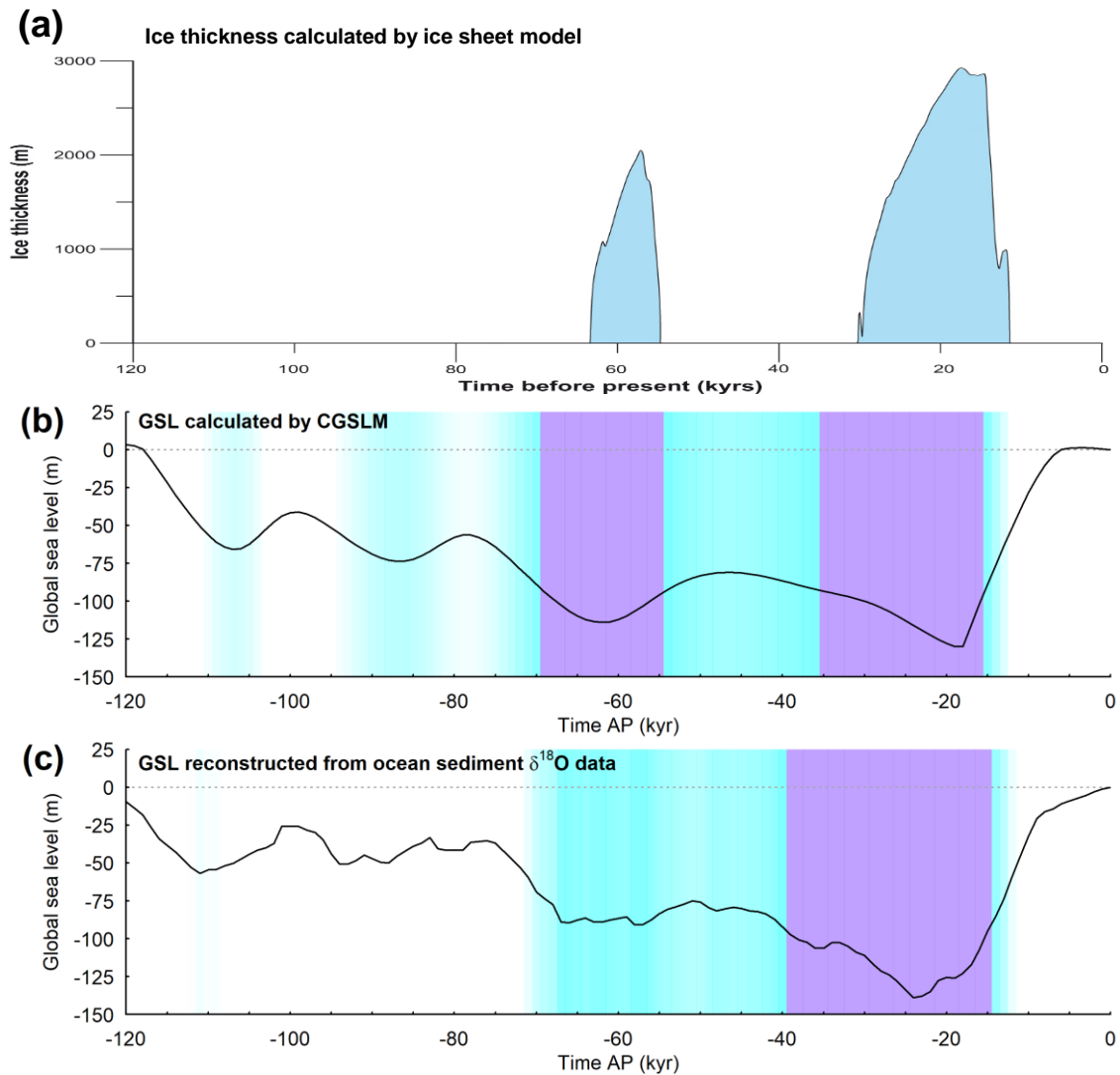
Figure 8. Evaluation of the GSL threshold method used to estimate the timing of ice coverage at the Olkiluoto and Forsmark sites, based on global ice sheet data for the last 120 kyr. (a) Ice sheet thickness over Forsmark reconstructed using UMISM (SKB 2010). Source: Taken from Figure 4-18 (p. 189) of SKB (2010). (b) Global sea level (m) calculated using the CGSLM. Vertical bands represent periods when the Fennoscandian ice sheet is projected to cover the sites, with purple shading indicating higher confidence (GSL < -93 m) and cyan shading indicating lower confidence (-93 m < GSL < -53 m) ice coverage. A higher degree of cyan shading indicates lower uncertainty. (c) Global sea level (m) reconstructed from ocean sediment core $\delta^{18}O$ data (Spratt and Lisiecki 2016). Vertical bands represent periods when the Fennoscandian ice sheet is projected to cover the sites.

Figure 8b applies the threshold method to GSL data calculated using the CGSLM, whilst Figure 8c applies it to GSL data reconstructed from ocean sediment core $\delta^{18}O$ data (Spratt and Lisiecki 2016), which is used to force the emulator in Section 3.2.3. These results were compared to projections of ice sheet coverage and thickness at Forsmark (Figure 8a), calculated using the University of Maine Ice Sheet Model (UNISM) and calibrated in part against known Weichselian ice marginal positions as interpreted from glacial morphological observations and datings (SKB 2010). In SKB (2010) this model was used to project changes in the Weichselian ice sheet over the last 120 kyr, in response to proxy air temperature data from the Greenland GRIP ice core (Dansgaard et al. 1993) and to sea level changes. It can be seen that the periods of ice coverage at the two sites identified using the GSL threshold (Figures 8b and 8c) are in reasonable agreement with the results of the ice sheet model reconstruction (Figure 8a) which show the presence of ice between approximately -64 to -55 kyr AP, during Marine Isotope Stage (MIS) 4, and -30 to -11 kyr AP, during MIS 2 (LGM). When the threshold approach is applied to the GSL results calculated by the CGSLM (Figure 8b), higher confidence ice coverage (purple shading) is projected to occur between approximately -69 and -55 kyr AP and -35 and -16 kyr AP, in relatively close agreement with the ice sheet model reconstruction. Periods of lower confidence ice coverage (cyan shading) are projected to occur before and after these episodes, along with very low confidence ice coverage (light cyan shading) projected at approximately -110 kyr and -94 kyr AP. In contrast, the proxy GSL data (Figure 8c) suggests that a higher confidence ice-covered period occurs from approximately -39 to -15 kyr AP, suggesting that for this data the ice sheet advances slightly too early compared to the modelled reconstruction. Lower confidence ice coverage (cyan shading) is projected to occur from -71 to -40 kyr AP, although for much of this time a lower degree of cyan shading is evident indicating lower certainty. Several bands of higher-degree cyan shading (indicating relatively higher certainty, although not as high as periods of purple shading) occur between approximately -67 and -55 kyr AP, in general agreement with the ice sheet modelling results.
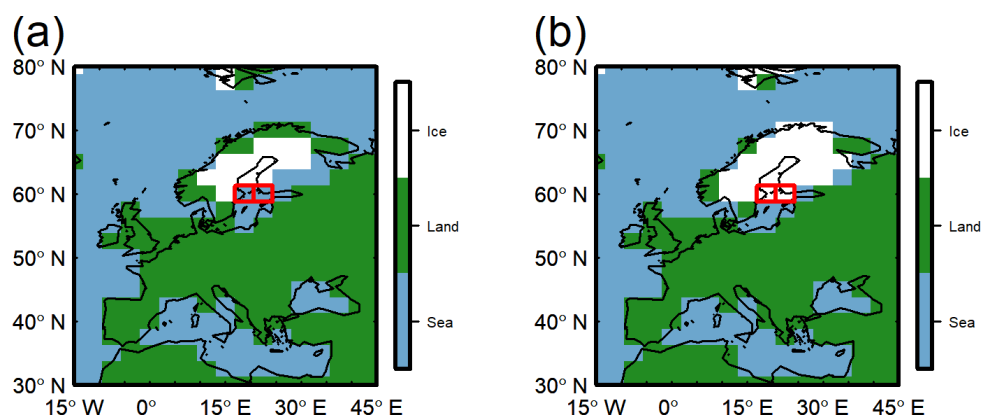
Figure 9. *Surface types for the region of Europe showing land/sea boundaries and ice sheet extent. The two site grid boxes are also shown in red. Snapshots have GSL values of: (a) -46 m and (b) -73 m.*

There is some uncertainty associated with the GSL projections of the CGSLM due to it being a relatively simple conceptual model, thus it increases our confidence in both the conceptual model and the GSL threshold method that our results are in reasonable agreement with the ice sheet modelling results of SKB (2010), and GSL records reconstructed from proxy data.

Updated atmospheric CO_2 concentration

As described in Section 3.1.1, the carbon cycle impulse response function estimates the future evolution of atmospheric CO_2 concentration following anthropogenic CO_2 emissions, modelling it as a smooth decline back towards pre-industrial over hundreds of thousands of years or more. However, as discussed in Lord et al. (2017), a limitation of this projection of CO_2 is that it does not account for interactions between the glacial-interglacial cycles and atmospheric CO_2. These include natural changes in CO_2 that have been found to accompany past glacial–interglacial cycles, with glacial periods over the last 800 kyr exhibiting CO_2 concentrations of approximately 180 to 200 ppmv (Petit et al. 1999), whereas interglacial periods demonstrated concentrations of 240 to 290 ppmv (Luthi et al. 2008). Therefore, the atmospheric CO_2 concentration data was updated to include a representation of the natural decline in concentration that has accompanied past glacial periods. An overview of the method used is shown in Figure 3 (labelled "Regression"). Atmospheric CO_2 concentration data for the last 800 kyr (Luthi et al. 2008) was regressed against reconstructed global temperature data for the same period (Jouzel et al. 1993), both of which were derived from palaeo climate proxies. The resulting function represents the relationship between these variables, and thus the relationship between CO_2 and glacial-interglacial transitions, which generally vary in synchrony with global temperature. There are other methods by which the relationship between the glacial cycles and CO_2 could be accounted for, such as by using an EMIC coupled to an ice sheet model which includes ice sheet-CO_2 feedbacks, for example CLIMBER-2 (e.g. Ganopolski and Brovkin 2017). However, the *c*GENIE model was selected to simulate atmospheric CO_2 because it contains a relatively complete representation of the long-term carbon cycle, and the carbon cycle response function provides a quick and effective tool for simulating CO_2 variations occurring over hundreds of thousands of years.

The regression function was then applied to update the future atmospheric CO_2 concentration data for the RCP scenarios in response to the projected global temperature anomaly data produced by the CGSLM. When temperature fell below 0 °C (anomaly compared with present-day), atmospheric CO_2 was calculated based on its identified relationship with global temperature. When temperature was greater than 0 °C, and thus in an interglacial state, the original results from the carbon cycle response function were used, capturing only anthropogenic forcing. The updated CO_2 projections for the four emissions scenarios are presented in Section 3.2.3.

3.2 Emulator configuration

As previously mentioned, a statistical emulator was used to project the future evolution of global climate over the next 1 Myr. The theoretical basis for the emulator, along with its calibration, optimisation, and limitations are fully discussed in Lord et al. (2017).

3.2.1 GCM simulations

The emulator was calibrated based on a large ensemble of simulations with varying climate conditions, run using the HadCM3 GCM. Since the emulator configuration presented here was modified from that in Lord et al. (2017) to include five, rather than four, input dimensions (three orbital parameters, CO_2 concentration, as well as GSL), the GCM simulations sampled a range of values for these parameters. Two separate emulators were used, which were each calibrated on different GCM simulations; one suitable for glacial conditions and one for interglacial conditions. For timesteps that had a GSL value of equal to or higher than 0 m (equivalent to present-day interglacial conditions), the interglacial emulator was used, whilst timesteps with a GSL value of lower than 0 m used the glacial emulator. This approach was taken to ensure that there was no blending of state-specific climate variations across different climate states. For example, under glacial conditions development of the Laurentide ice sheet is accompanied by strong cooling over northern North America. However, this does not mean that during interglacial conditions there should be a strong warming in the same region, since the data are presented as an anomaly from interglacial present-day conditions (where no ice sheet is present). The use of separate emulators therefore ensures that the different glacial states are characterized separately and correctly. No negative effects of using two separate emulators were experienced, and checks were carried out to ensure that there were no discontinuities between the climate projections from the different emulators.

The emulator for interglacial conditions was calibrated on the *modice* and *lowice* GCM simulations described in Lord et al. (2017). These are two ensembles of simulations, each made up of 60 experiments with varying atmospheric CO_2 and orbital parameter values. Atmospheric CO_2 concentration ranges from 250 ppmv up to 1901 ppmv. A set of 20 additional simulations, with CO_2 concentrations higher than 2000 ppmv (Lord 2017), were excluded for the reasons discussed by Lord et al. (2017). The *modice* ensemble has fixed modern-day ice sheet extents, whilst the *lowice* ensemble has fixed reduced GrIS and WAIS extents, based on the PRISM4 Pliocene reconstructions (Dowsett et al. 2016). Global temperatures during the Pliocene were higher than they are at present, meaning that in the ice sheet reconstruction the GrIS is limited to high elevations in the Eastern Greenland Mountains, and no ice is present over Western Antarctica. Large regions of the EAIS show minimal changes or slightly increased surface elevation, although there is substantial loss of ice in the Wilkes and Aurora subglacial basins (Haywood et al. 2016). Similar patterns of ice retreat have been simulated in response to future warming scenarios for the GrIS (Greve 2000, Huybrechts and de Wolde 1999, Ridley et al. 2005, Stone et al. 2010) and WAIS (Huybrechts and de Wolde 1999, Winkelmann et al. 2015). These two ice sheet configurations therefore represent climate states ranging from interglacial conditions to relatively severe global warming conditions accompanied by significant ice sheet retreat.

The emulator for glacial conditions is also calibrated on the 60-member *modice* ensemble of GCM simulations from Lord et al. (2017). An additional suite of simulations is also included as calibration data which were produced by Singarayer and Valdes (2010) (denoted "*LGC*" ensemble), and also run using HadCM3. These are a series of snapshot simulations covering the last glacial cycle (LGC; 120 kyr BP to present day), forced by changes in orbit, atmospheric CO_2 concentration, and ice sheet evolution. The reconstructed ice sheet extents are based on the ICE-5G model of Peltier (2004). Combined, the *modice* and *LGC* ensembles capture changes in climate and ice sheet extent ranging from interglacial states to full glacial conditions.

A principal component analysis (PCA) was carried out on the GCM data before it was used to calibrate the emulator. This analysis is fully detailed in Lord et al. (2017), and involved combining the spatial information contained in the GCM data and the input data (climate forcings) into a number of maps (dimension reduction) and producing associated weightings for each experiment and principal component (PC). In order to reproduce the original GCM output for a specific experiment with a specific set of climate forcing conditions (i.e. CO_2 concentration, etc.), or to estimate the climate resulting from a new set of climate forcing conditions, the PCs were weighted depending on the input conditions for the experiment and then combined to give the emulated climate projection resulting from the input forcing conditions.

3.2.2 Optimisation and evaluation of the emulator

The GCM data used to calibrate the two emulators were selected based on which climate variable was being emulated. For example, when future SAT was being projected, the SAT data produced by the GCM was used for calibration. Before being used, each emulator configuration was optimised via the method described in Lord et al. (2017). This optimisation process selected the optimal number of PCs to be retained (the majority of the PCs were discarded as they only account for a very small amount of total variation in the GCM data), and the values for a number of hyperparameters used in the emulator. These include a correlation length hyperparameter for each input dimension (δ), which describes the smoothness of the climate response in the GCM data to the input conditions, and a nugget parameter (v), which has a number of functions including accounting for any non-linearity in the output response and representing the effects of the discarded PCs. However, it was demonstrated in Lord (2017) that the optimisation can be carried out on SAT, and then the optimized configuration applied to other climate variables with no significant loss of performance. Hence, this approach was adopted here.

In order to optimize the two emulators, each was calibrated on the GCM SAT data from its respective ensemble(s) of simulations. The input factors ($\ln(CO_2)$, ε, $e\sin\varpi$, $e\cos\varpi$, and GSL) were standardised prior to the calibration being performed; each was centred in relation to its column mean, and then scaled based on the standard deviation (SD) of the column. Different emulator configurations were tested by varying the number of PCs retained, ranging from 5 to 20, and for each emulator configuration, the correlation length scales δ and nugget v were optimized by maximisation of the penalised likelihood (see Lord et al. 2017 for explanation). This optimisation was carried out in log space, ensuring that the optimized hyperparameters would be positive.

The performance of each emulator was assessed using a leave-one-out cross-validation approach, in which a series of emulators is constructed and used to predict one left-out experiment each time. For example, for the interglacial emulator (120 experiments), 120 separate emulators were calibrated with one experiment left out of each. This left-out experiment was then reproduced using the corresponding emulator and the results were compared with the actual experiment results. The number of grid boxes for each experiment calculated to lie within different SD bands, and the RMSE averaged across all the 120 emulators were used as performance indicators to compare the different selected values for retained PCs and hyperparameters. Following the leave-one-out validation, the two emulator configurations that performed best were selected as the final two optimized emulators. It was found that the optimized interglacial emulator retained 15 PCs (accounting for 90% of total variance), and had length scales δ of 2.792 (ε), 1.310 ($e\sin\varpi$), 1.664 ($e\cos\varpi$), 0.523 (CO_2), and 10.000 (GSL), and a nugget of 0.000. The optimized glacial emulator retained 15 PCs (accounting for 81% of total variance), and had length scales δ of 6.908 (ε), 7.499 ($e\sin\varpi$), 5.460 ($e\cos\varpi$), 1.003 (CO_2), and 0.290 (GSL), and a nugget of 0.050.

The results of the evaluation of the emulators are shown in Figure 10. The results suggest that the emulators perform relatively well. Figures 10a and 10c show the percentage of grid boxes for each left-out experiment estimated by the corresponding emulator within different standard deviation bands, along with the RMSE. A few of the experiments performed considerably worse than others, exhibiting below the expected number of grid boxes with errors within 1 SD, and/or higher than the expected number of grid boxes with errors of greater than 2 SD, which is generally accompanied by a higher RMSE. However, the input conditions for these experiments are not particularly similar or unique.

Figures 10b and 10d compare the mean annual "SAT index" for each left-out experiment calculated by the GCM and the corresponding emulator (note: this is the mean value for the GCM output data grid assuming all grid boxes are of equal size, hence not taking into account grid box area). There are no obvious outliers, and the emulated means are relatively close to their modelled equivalents. There also does not appear to be any significant loss of performance at very low or very high temperature, and therefore at very low or very high CO_2.
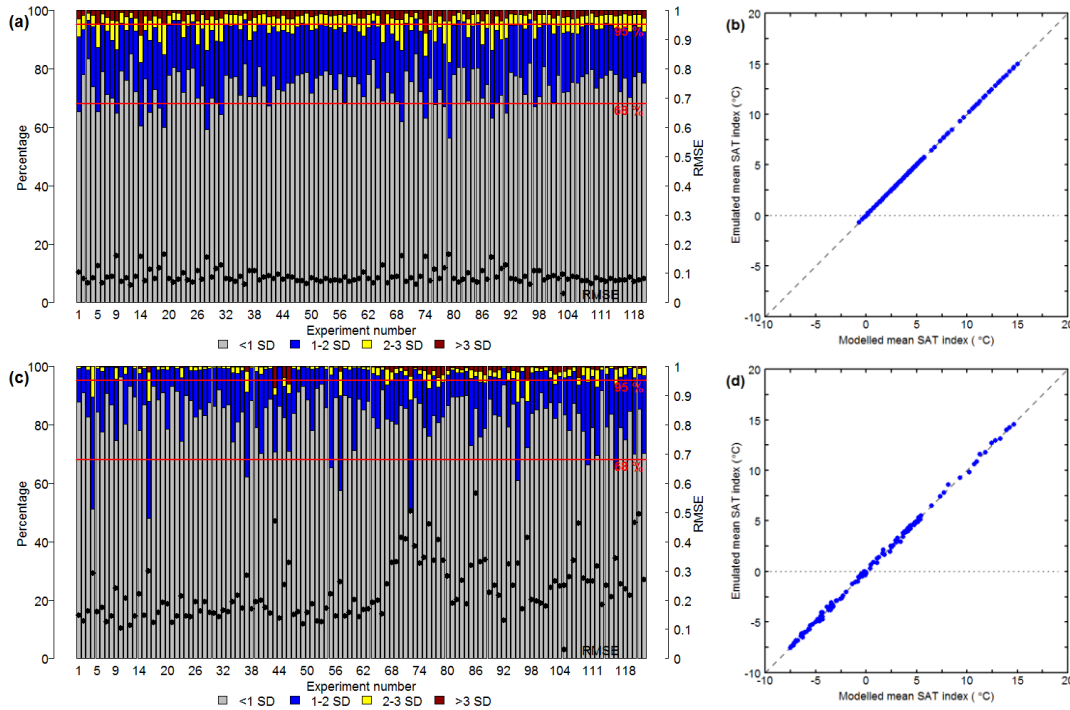
Figure 10. *Evaluation of emulator performance for the interglacial emulator (top panel) and glacial emulator (bottom panel), both calibrated on SAT data. (a) + (c) Bars give the percentage of grid boxes for which the emulator predicts the SAT of the left-out experiment to within 1, 2, 3 and more than 3 SD. Also shown is the RMSE for the experiments (black circles). Red lines indicate 68 and 95 %. (b) + (d) Mean annual SAT index (°C) calculated by the emulator and the GCM. The 1 : 1 line (dashed) is included for reference. Note: this is the mean value for the GCM output data grid assuming all grid boxes are of equal size, hence not taking into account variations in grid box area. SAT is shown as an anomaly compared with the pre-industrial control simulation.*

In summary, the calibration and evaluation shows that the emulators are able to reproduce the left-out ensemble simulations reasonably well, with no obvious systematic errors in their predictions. These emulator configurations were optimized on SAT data, and these same configurations (i.e. same number of retained PCs and hyperparameter values) were then also applied to emulate the other variables. This approach ensures that the results for the variables are consistent with each other.

3.2.3 Palaeo-validation of the emulator

In order to further evaluate the performance of the emulator in simulating long-term changes in climate, and thus to be able to assess its likely performance in simulating future climate, it was used to model temperature and precipitation over the last 800 kyr (middle to late Pleistocene). This time period was selected because a range of high-resolution palaeo records exist, of multiple variables and in multiple locations, providing both forcing data for the emulator and proxy climate reconstructions which can be compared to the emulator results. The climate variables were emulated at 1 kyr intervals over the time period and forced with the records illustrated in Figure 11. Orbital data (Figure 11a) was calculated using the method of Laskar et al. (2004). A composite record of observed atmospheric CO_2 was also used (Figure 11b), which was measured from the Dome C ice cores from Antarctica (Bereiter et al. 2015). Finally, the sea level stack reconstructed from $\delta^{18}O$ data from ocean sediment cores produced by Spratt and Lisiecki (2016) was used (Figure 11c), in order to provide the GSL index used as the fifth forcing parameter to the emulator.

A number of different reconstructions of palaeoclimate taken from several locations, shown in Figure 12, were used for comparison to the emulator results, selected due to their high temporal resolution and coverage of the last 800 kyr. These records consist of:

- Reconstructed Antarctic temperature, derived from Deuterium data from the Dome C ice core (Jouzel et al. 2007).
- Reconstructed sea surface temperature (SST) data for the South China Sea and North Atlantic, based on $\delta^{18}O$ data from ocean sediment cores collected from the Ocean Drilling Program (ODP) site 1143 (Li et al. 2011) and site 982 (Lawrence et al. 2009).
- $\delta^{18}O$ data measured from cave speleothems, which is thought to be a proxy for variations in the strength of East Asian monsoon rainfall. Records from two caves were used to provide full coverage of the last 224 kyr; the Sanbao Cave in central China (Wang et al. 2001) and the Hulu Cave in eastern China (Wang et al. 2008).
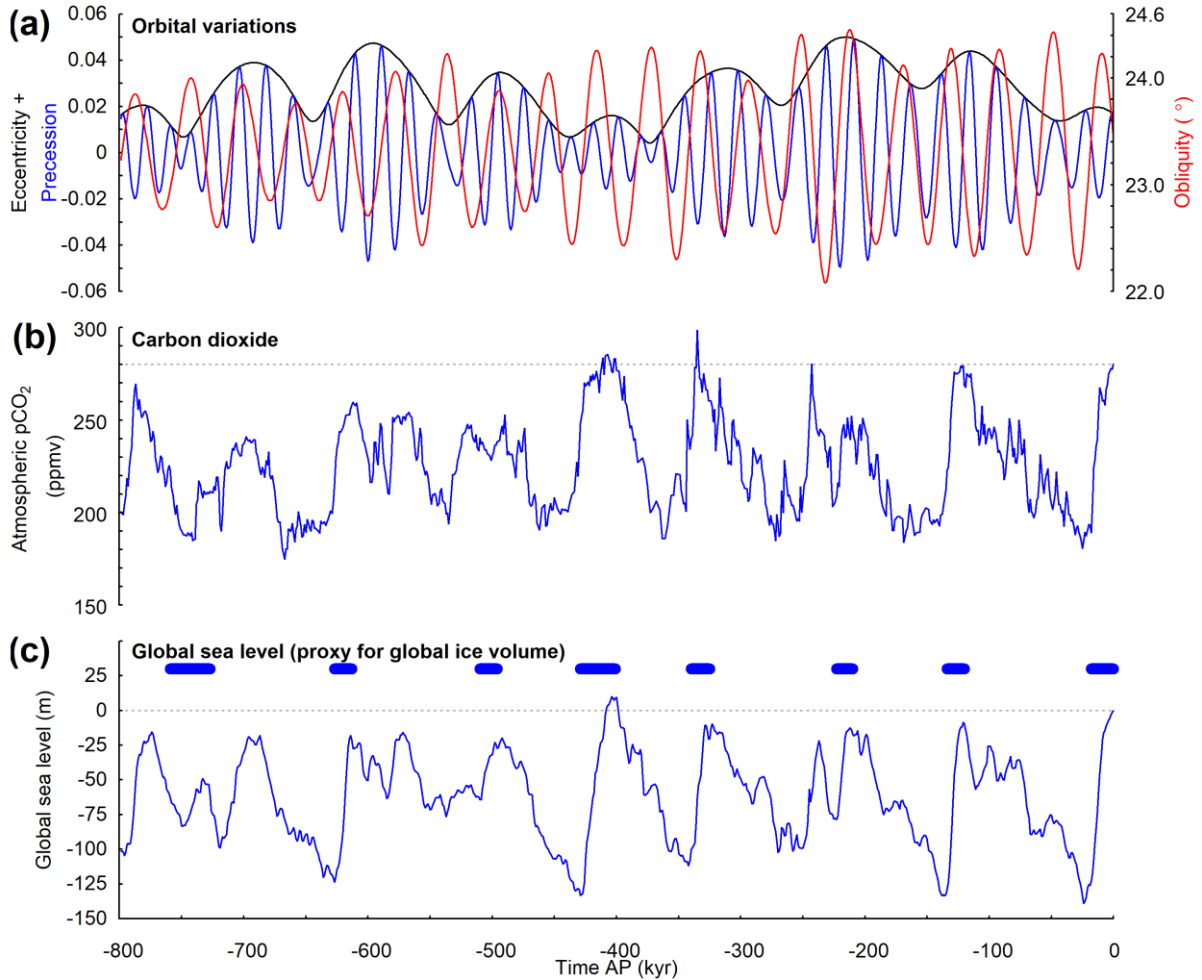
Figure 11. *Climate forcing data used as input to the emulator for the last 800 kyr. (a) Time series of orbital variations (Laskar et al. 2004), showing eccentricity (black) and precession (blue) on the left axis, and obliquity (degrees; red) on the right axis. (b) Time series of observed atmospheric CO_2 concentration (ppmv) constructed from composite records from Antarctic ice cores (Bereiter et al. 2015). The pre-industrial CO_2 concentration is also shown (grey dotted line). (c) Time series of reconstructed global sea level (m) derived from ocean sediment core $\delta^{18}O$ data (Spratt and Lisiecki 2016), shown as an anomaly compared with pre-industrial. Periods of interglacial conditions are indicated by thick horizontal bands.*

Palaeo SST data is used for comparison with emulated SAT because multiple records exist from varying global locations, which cover hundreds of thousands of years at a sufficient resolution to capture orbital cycles. Each proxy data set was compared to emulated mean annual SAT or precipitation for the appropriate grid box for each site (Figure 12). Temperature and precipitation data are generally shown as anomalies compared to pre-industrial conditions at the different locations, taken from each proxy data set in the case of SST, and the pre-industrial control simulation in the case of SAT and precipitation.
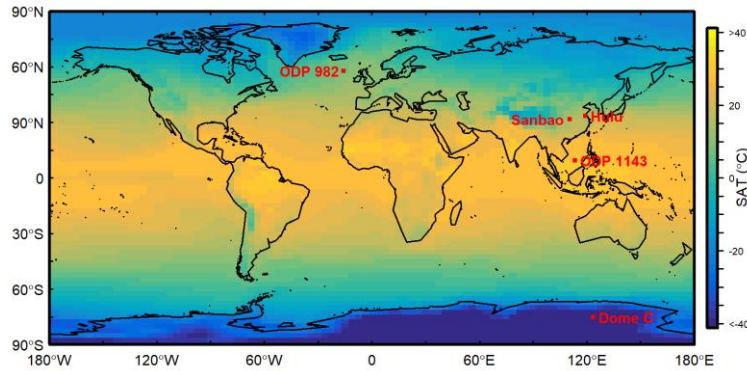
Figure 12. Map highlighting the source locations of the proxy data records. Temperature records are from Antarctica (Dome C), the South China Sea (ODP 1143), and the North Atlantic (ODP 982). East Asian Monsoon records are from central (Sanbao Cave) and eastern China (Hulu Cave). Background shading illustrates pre-industrial SAT (°C) taken from a HadCM3 control simulation.

Figure 13 compares the proxy and emulated temperature data for the Antarctic, South China Sea and North Atlantic sites. It can be seen that the emulator does a reasonably good job of reproducing SAT variations over the last 800 kyr at these sites. In particular, the timing and duration of many of the interglacials and glacial maxima are similar in the model and observations, and the agreement between the magnitude of variations is generally fairly good. However, there are some instances when the relative maxima and minima are not well reproduced by the emulator, such as the interglacials at approximately -330 kyr, -240 kyr and -125 kyr AP in the Dome C data (Figure 13a), or the interglacials at around -700 kyr and -620 kyr AP, and the LGM in the data for ODP site 1143 (Figure 13b), which are underestimated by the emulator relative to the proxy data. For site 982 (Figure 13c), the SAT anomaly compared to present day is underestimated compared to the ocean core SST anomaly data at the interglacial periods occurring at approximately -700 kyr, -620 kyr and -130 kyr AP, whist the emulator demonstrates stronger glacial cooling than the proxy data from approximately -760 to -620 kyr AP, -200 and -150 kyr BP, and during the LGM (-18–-21 kyr AP).

The relatively large uncertainty in the emulator at approximately -400 kyr AP at Dome C (Figure 13a) is possibly due to the fact that, contrary to the transition from interglacial to glacial conditions for which changes in the ice sheets are well sampled, there are only two different Antarctic ice sheet configurations for interglacial conditions – modern-day ice (*modice*) and reduced ice (*lowice*). Therefore, the emulator uncertainty in regions where the ice sheets change significantly whilst in an interglacial state is relatively high, because the emulator effectively only has two ice sheet configurations to interpolate between. This uncertainty could be reduced by carrying out a number of additional GCM simulations with ice sheet configurations that vary within the limits set by the *modice* and *lowice* configurations. However, this is beyond the scope of this study, and is not expected to have a significant impact on the results for the two repository sites since they are located relatively far from the GrIS and AIS.
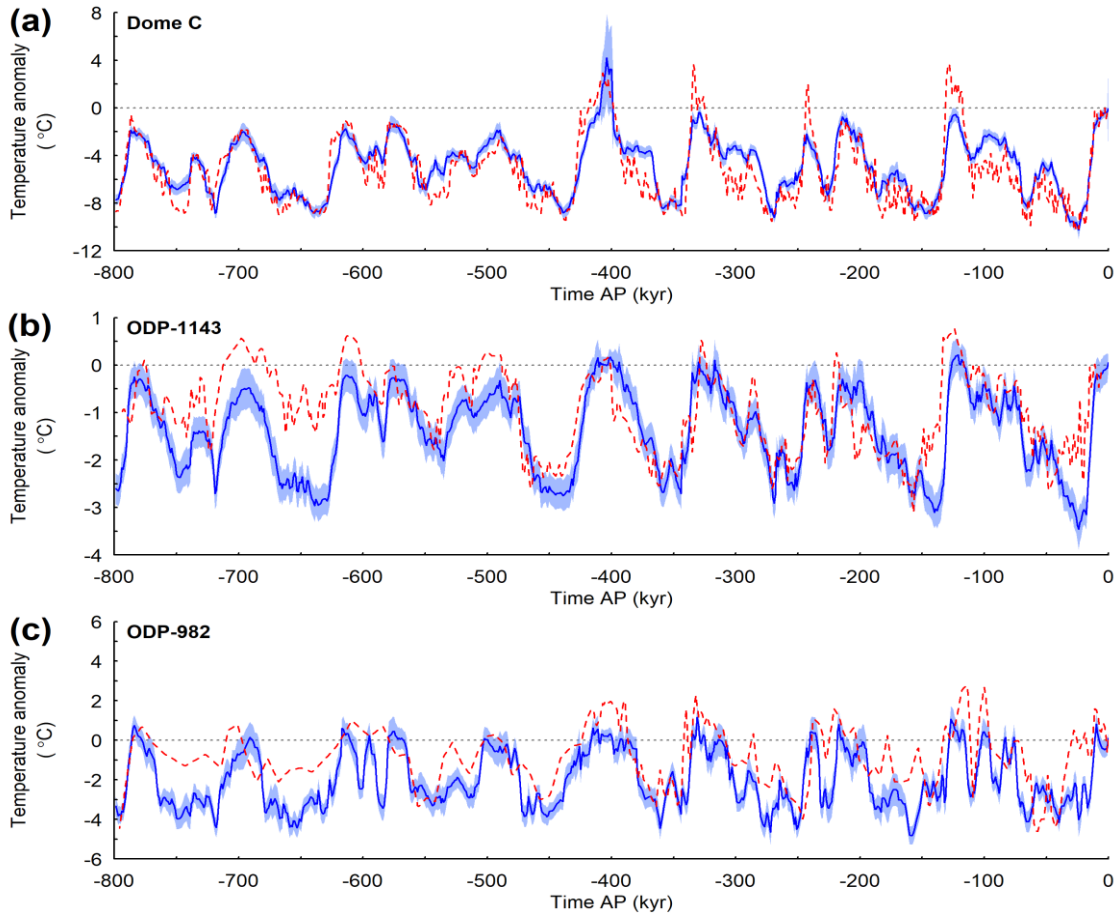
Figure 13. *Time series of temperature anomaly (°C) for the last 800 kyr reconstructed from proxy data (red dashed lines) and modelled using the emulator (blue solid lines) at three locations. (a) Dome C, Antarctica. Temperature reconstructed from a Deuterium record from the Dome C ice core (red dashed line; Jouzel et al. 2007). Temperature is shown as an anomaly relative to the mean temperature of the last millennium. Emulated mean annual SAT anomaly compared to a pre-industrial control simulation (blue solid line), modelled every 1 kyr. (b) ODP 1143, South China Sea. SST reconstructed from a $\delta^{18}O$ record from ocean sediment cores (red dashed line; Li et al. 2011). SST is shown as an anomaly compared to the pre-industrial SST from the data set. Emulated mean annual SAT anomaly compared to a pre-industrial control simulation (blue solid line), modelled every 1 kyr. (c) ODP 982, North Atlantic. SST reconstructed from a $\delta^{18}O$ record from ocean sediment cores (red dashed line; Lawrence et al. 2009). SST is shown as an anomaly compared to the pre-industrial SST from the data set. Emulated mean annual SAT anomaly compared to a pre-industrial control simulation (blue solid line), modelled every 1 kyr. Blue error bands represent the emulated grid box posterior variance (1 SD).*

The δ^{18}O data records from China (used as a proxy for precipitation) are compared with emulated precipitation in Figure 14. As with SAT, the emulator appears to be able to reproduce the major variations evident in the δ^{18}O record reasonably well, particularly with regards to the precession-driven timing of maxima and minima in precipitation. However, there are some differences between the relative intensities of some of these extremes; for instance, the two maxima in δ^{18}O at around -160 to -180 kyr AP are relatively weak in the emulator simulation, and the precipitation minimum at approximately -210 kyr AP is more intense in the δ^{18}O data. However, direct quantitative comparison between these records is challenging without including an explicit representation of oxygen isotopes in the underlying GCM simulations.
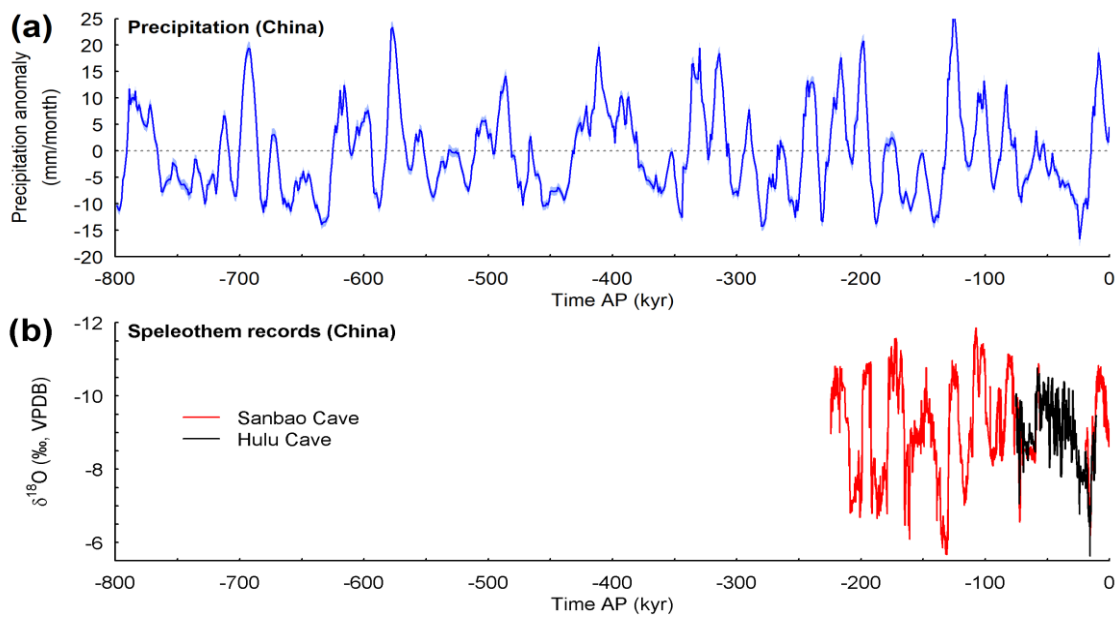
Figure 14. Time series of precipitation for the last 800 kyr for China. (a) Emulated mean annual precipitation anomaly compared to a pre-industrial control simulation (mm/month). Precipitation is modelled every 1 kyr. Error bands represent the emulated grid box posterior variance (1 SD). (b) δ^{18}O records (‰, VPDB) from the Sanbao (Wang et al. 2001) and Hulu (Wang et al. 2008) caves in China covering the last 224 kyr. Cave speleothem δ^{18}O data is taken to be a proxy for variations in the strength of the East Asian monsoon. For comparison, the Hulu record is plotted 1.6‰ more negative to account for the higher Hulu values (Wang et al. 2001).

All in all, comparison of emulated SAT and precipitation to a number of proxy climate reconstructions from various sources suggests that the emulator performs reasonably well when modelling climate changes over long timescales. Discrepancies between the emulator and proxy data could occur due to a number of reasons, including errors in the emulator, where the response of a climate variable to a forcing has not been full captured, or errors in the underlying GCM. Errors may also be related to missing forcings/processes in the model, such as freshwater fluxes, non-CO_2 greenhouse gases, or aerosols such as dust. They could also be associated with errors in the proxy data, such as uncertainties in the calibration of the underlying proxy data. It may also be that the proxies used are influenced by local conditions other than the variable being reconstructed; speleothem $\delta^{18}O$ data for example may be affected by temperature or local conditions in the cave, in addition to monsoon intensity. It is likely that in reality the differences are due to a combination of several of these reasons.

The SAT anomaly (compared to pre-industrial) at the LGM was also reproduced using the emulator, illustrated in Figure 15a, and compared to the SAT anomaly reconstruction of Annan and Hargreaves (2013), shown in Figure 15b. This reconstruction was produced by combining a range of proxy records of climate from different parts of the globe with an ensemble of simulations performed with various climate models as part of the PMIP2 project (Braconnot et al. 2007). It can be seen that the large-scale features of SAT are similar between the two reconstructions, with the most significant regions of cooling located over the Laurentide ice sheet in North America, and to a lesser extent the Fennoscandian ice sheet. There are some discrepancies, including the extent of cooling over the Laurentide and Fennoscandian ice sheets being too large in the emulated reconstruction, and high latitudes (Arctic and Antarctic regions) also being slightly too cold in this simulation compared to that of Annan and Hargreaves (2013). This enhanced cooling in the emulator at this time is highlighted by a global mean cooling value of 5.1 °C, slightly more than the value estimated by Annan and Hargreaves (2013) of 4.0 °C. At the Olkiluoto and Forsmark sites, the SATs projected by the emulator are approximately 1 °C and 3 °C cooler than the same locations in the model-proxy reconstruction, respectively. However, the temperatures over ice sheets in the reconstruction are very uncertain, and based on model results rather than direct proxies. As identified in Section 1.1, one of the key questions for high latitude repository sites relates to the timing and severity of future glaciations. The SAT projections during glacial conditions could therefore be considered as worst-case – if the reconstruction is correct then the cooling and associated impacts (e.g. permafrost) may not be quite as severe as projected in this report.

Overall, the generally good agreement between the proxy and emulator data for the last 800 kyr, particularly when considering the orbital-scale variations in climate, along with the evaluation of LGM climate, and the leave-one-out evaluation reported in the previous section, gives confidence that the emulator can realistically simulate changes in climate across a wide range of different forcing conditions.
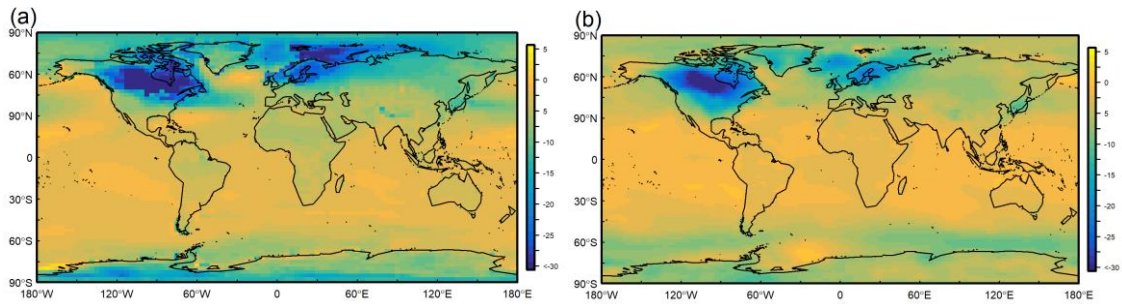
Figure 15. Maps of SAT anomaly (compared to pre-industrial; °C) at the Last Glacial Maximum (-21 kyr AP) as projected by: (a) the emulator, and (b) Annan and Hargreaves (2013), using a combination of proxy climate data and multi-model regression.

3.2.4 Forcing data

In order to simulate the possible evolution of climate over the next 1 Myr, the emulator was forced with the input data that was produced using the methods described in Section 3.1. This data consists of atmospheric CO_2 concentration, projected using the CO_2 impulse response function (Section 3.1.1), the three orbital parameters (Section 3.1.2), and GSL, estimated using the CGSLM (Section 3.1.3). These five variables are illustrated in Figure 16 and described in Section 4.1. The resulting scenarios are based on the assumption that beyond the end of the "fossil fuel era" (~2500 AD), humans will make no other significant changes to the natural carbon or glacial cycles, through emissions of CO_2 or other greenhouse gases. The evolution of summer insolation (averaged between June 21 and July 20) at 65°N over the next million years is shown in Figure 17, which illustrates the combined impacts of the three orbital parameters presented in Figure 16 on incoming solar radiation. As discussed previously, the insolation received in the Northern Hemisphere during the summer is thought to be critical in determining transitions between interglacial and glacial conditions. As in Lord et al. (2017), the climate was modelled at 1 kyr intervals, producing a continuous projection for the next 1 Myr. The locations of the two sites on the HadCM3 grid are illustrated in Figure 18. Olkiluoto has a latitude of 61.2° N and a longitude of 21.5° E, whereas Forsmark has a latitude of 60.4° N and a longitude of 18.2° E.
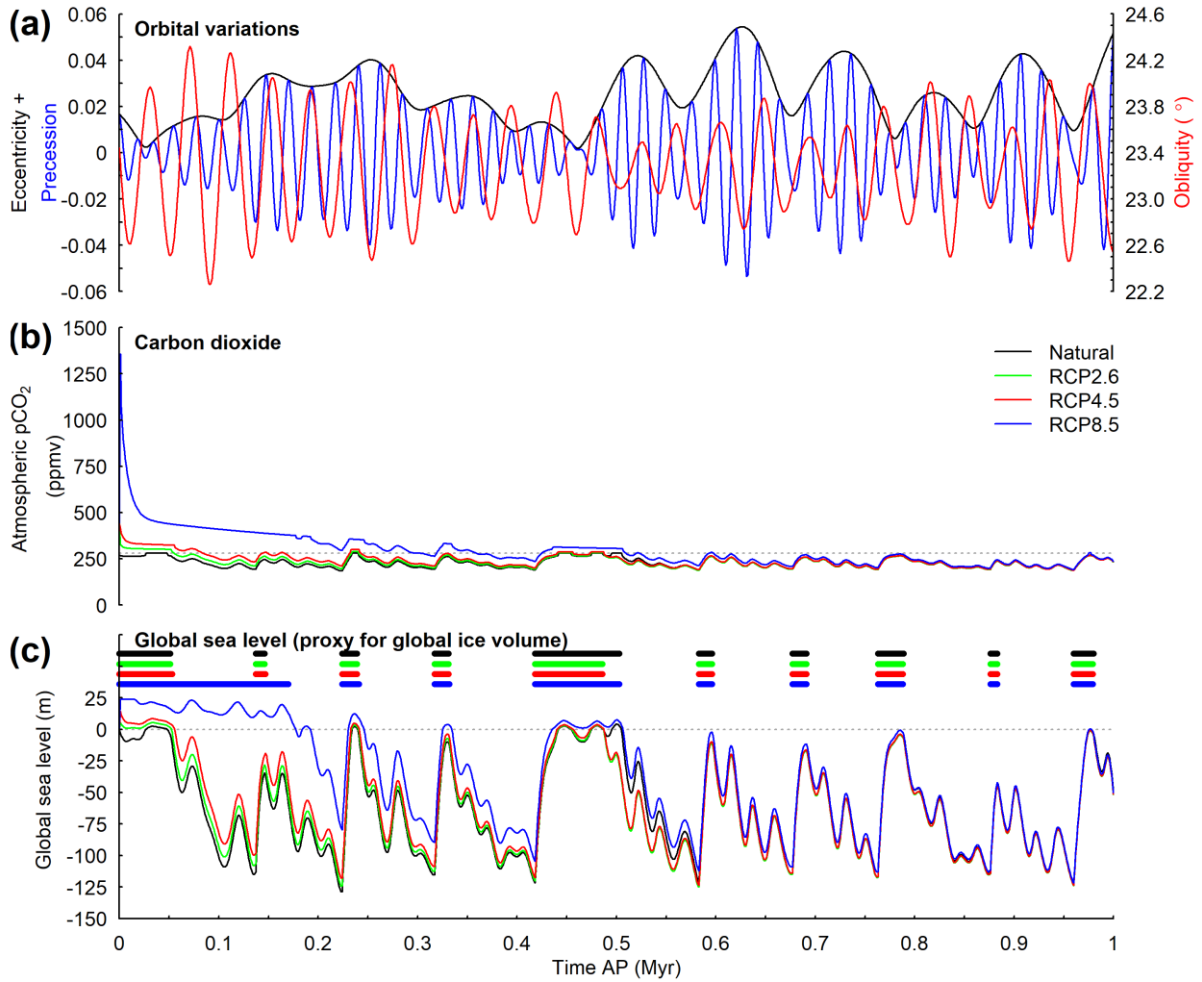
Figure 16. *Climate forcing data used as input to the emulator for the next million years. (a) Time series of orbital variations (Laskar et al. 2004), showing eccentricity (black) and precession (blue) on the left axis, and obliquity (degrees; red) on the right axis. (b) Time series of atmospheric CO_2 concentration (ppmv) for the natural (black line), RCP2.6 (green line), RCP4.5 (red line), and RCP8.5 (blue line) emissions scenarios, predicted using the carbon cycle impulse response function of Lord et al. (2016), and updated to include the impact of global temperature/CO_2 feedbacks (see Figure 4a for comparison). The pre-industrial CO_2 concentration is also shown (grey dotted line). (c) Time series of global sea level (m) for the four emissions scenarios, shown as an anomaly compared with pre-industrial. Periods of interglacial conditions for each emissions scenario are indicated by thick horizontal bands.*
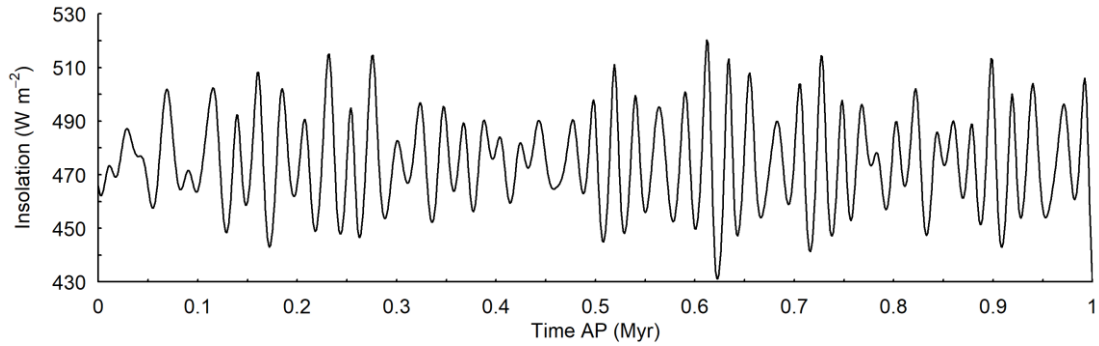
Figure 17. Evolution of summer insolation (W m⁻²) at 65°N for the next million years, calculated using the method of Laskar et al. (2004).

The climate variables modelled are SAT and precipitation. For each variable in turn, the two emulators (glacial and interglacial versions) were calibrated on the relevant HadCM3 data, and then forced with the future climate forcing data (Figure 16). The data for the two emulators were then combined: for each time-slice (every 1 kyr), if the GSL was above 0 m (pre-industrial), the respective emulated climate from the interglacial emulator was retained, whilst if GSL was below 0 m, the respective emulated climate from the glacial emulator was retained. The retained data was then combined to provide a projection of the evolution of the variable over the next 1 Myr, with the glacial-interglacial cycles being accounted for in the results.
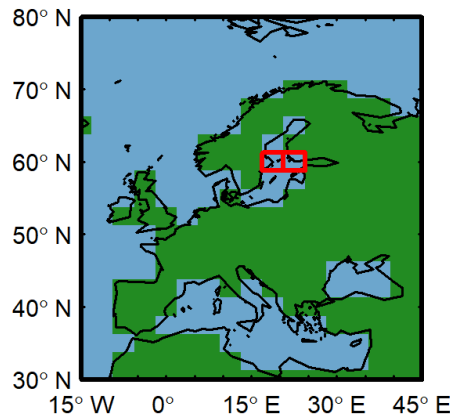
Figure 18. Map of Europe highlighting the grid boxes that represent the Forsmark (left red grid box) and Olkiluoto (right red grid box) case study sites.

3.3 Downscaling of future climate

The future climate data produced by the emulator has the same spatial resolution as the underlying GCM, HadCM3, of 3.75° of longitude by 2.5° of latitude. This equates to a surface resolution of about 417 km x 278 km at the Equator, reducing to 295 km x 278 km at 45° N or S. However, it may be that this resolution is too low for certain applications, which may require a more detailed characterisation of changes in climate at the local scale of the site. For instance, in order to run a site-specific landscape development model, climate data of a higher spatial resolution may be required in order to account for the impacts of local conditions on climate, such as sub-grid box scale changes in orography. Where this is the case, climate data can be downscaled to a higher spatial resolution. In this report, downscaling to a ~50 km scale will be considered, as this is the scale of the multivariate global gridded observational climate dataset which has been used to allow downscaling to be carried out.

There are a number of different approaches that can be used to downscale climate data. The four main approaches are bias-correction (e.g. Brandefelt et al. 2013), dynamical downscaling (e.g. BIOCLIM 2003a, Kjellström et al. 2009), rule- based downscaling (e.g. BIOCLIM 2003c), and physical-statistical downscaling (e.g. Vrac et al. 2007). A detailed discussion of the different methodologies, along with some of their advantages and disadvantages, and a worked example of downscaling GCM climate data for application to potential sites for a geological disposal facility in Britain is provided by Thorne et al. (2016).

In the present study, two different techniques are applied to increase the spatial resolution of the future climate data for the region of Fennoscandia, which each have different strengths and weaknesses. The first one is a statistical bias-correction technique, which involves calculating the bias in the underlying GCM compared to observed climate data and applying this bias to the future projections to "correct" the projections. The second method is physical-statistical downscaling. Details of both techniques are included in this section, and the downscaled climate results are presented and discussed in Chapters 4 and 5.

3.3.1 Bias-correction downscaling

As mentioned above, the bias-correction technique involves calculating the bias in the GCM compared to observations under known climate conditions, and then applying this bias to the future projections of climate. In this case, the bias is calculated by comparing climate data for a pre-industrial simulation produced using the GCM to observational data for the sites. For this, the high-resolution CRU observed gridded climatology (v1) for the period 1961–1990 (New et al. 1999) was used, which provided SAT and precipitation observations for the region of Fennoscandia (52° N to 72° N, and 3° E to 31° E) , illustrated in Figures 19a and 19c. This 0.5° resolution data set equates to ~50 km resolution at this latitude. For the comparison, the pre-industrial SAT and precipitation data produced by the GCM (Figures 19d and 19e) was bilinearly interpolated to the same resolution as the CRU data. The bias of the GCM (T_{Bias}, P_{Bias}) for each grid box j was calculated as below:

$$T_{Bias_j} = T_{GCM_j}^{PI} - T_{CRU_j} \qquad\qquad \text{Equation 1}$$

$$P_{Bias_j} = P_{GCM_j}^{PI} / P_{CRU_j} \qquad\qquad \text{Equation 2}$$

where T (P) denotes SAT (precipitation), T_{GCM}^{PI} refers to the interpolated pre-industrial climate data from the GCM, and T_{CRU} refers to the observational data. Precipitation was bias-corrected by calculated the relative difference (rather than absolute difference) between the GCM and observations in order to avoid negative precipitation rates.

Following calculation of the bias, the SAT and precipitation data produced by the emulator at each timestep for the region of Fennoscandia was bilinearly interpolated to 0.5° resolution. To account for the bias in these projections, the bias at each grid box (j) was subtracted from the interpolated emulator value (T_{Em}) at that grid box for each time step (k), for SAT and precipitation separately:

$$T_{DSBias_j}^k = T_{Em_j}^k - T_{Bias_j} \qquad\qquad \text{Equation 3}$$

The climate data downscaled using this methodology is denoted T_{DSBias}.

In this downscaling technique, the observational data provides information about regional variations in SAT and precipitation, including for example the impacts of orography, at a higher resolution than that of the emulator. It also aims to correct some of the bias that results from the emulator, as well as the GCM itself, for example due to the parameterisations used or missing processes or feedbacks.

A limitation of this approach is that the bias is calculated based on modern-day interglacial climate conditions, and this bias is then applied to the emulated future projections which include different climate states (e.g. glacial) for which the bias may not be the same, particularly when an ice sheet is present. However, high-resolution observational data is only available for the last few decades or centuries, meaning that equivalent observational data for different climate states does not exist. Therefore, the assumption is made that the bias is applicable for the full million years, across all climate states. A similar downscaling approach was also adopted by Brandefelt et al. (2013).

Bearing in mind this limitation, an alternative set of downscaled future climate projections are presented in Chapter 5, which use the same bias-correction technique described above. However, when the Fennoscandian ice sheet is projected to be covering the Olkiluoto and Forsmark sites (i.e. GSL <-53 m), the bias correction is not applied, and the interpolated emulator result for each grid box is used instead. This approach was taken as there may be greater uncertainty associated with the bias-corrected climate during ice-covered periods, and it therefore illustrates the sensitivity of the climate data to different assumptions being made.

3.3.2 Physical-statistical downscaling

Additionally, a physical-statistical downscaling technique has been adopted in order to produce high-resolution projections of future climate for the whole region of Scandinavia. For this, a set of predictors are selected based on physical considerations, which are expected to have an impact on local climate, such as orography or distance from the coast. Then, a regression analysis is performed to derive the statistical relationships between the predictor variables, which may initially be at low resolution (i.e. from a global climate model), and the observed high-resolution variables (predictands), such as observational data of temperature. Various studies have applied this or similar methods of downscaling to European regions for application to radioactive waste disposal (e.g. BIOCLIM 2003d, Pimenoff et al. 2011, Thorne et al. 2016).

The regression model used in the downscaling was calibrated using high-resolution observational data for the present day and HadCM3 data for the pre-industrial/modern day (control simulation). The high-resolution CRU observed gridded climatology (v1) for the period 1961–1990 (New et al. 1999) was used to provide information about small scale changes in observed climate in response to local conditions over Scandinavia (Figures 19a and 19c). Following calibration, the model was applied to the results of the emulator to produce downscaled regional projections. All temperature and precipitation data used is mean annual data.

The relevant datasets, including the climate output and orography from the emulator, were bilinearly interpolated to the same resolution as the CRU data. Whilst the statistical model was fitted to global data to ensure that the climatic impacts of high elevations are captured, data from the region of Scandinavia (52°N to 72°N, and 3°E to 31°E) is illustrated in Figure 19.

For each climatic variable, a linear, multi-variate regression was fitted in R (statistical computing software), with the optimal parameter values being estimated using a least-squares approach. For a climate variable, V, the observed value V_{Obs} was compared to a calculated value, V_{Calc}, estimated by the regression model:

$$V_{Calc} = A_0 + A_1 * x + A_2 * y + A_3 * z \ldots + A_n * m \qquad \textit{Equation 4}$$
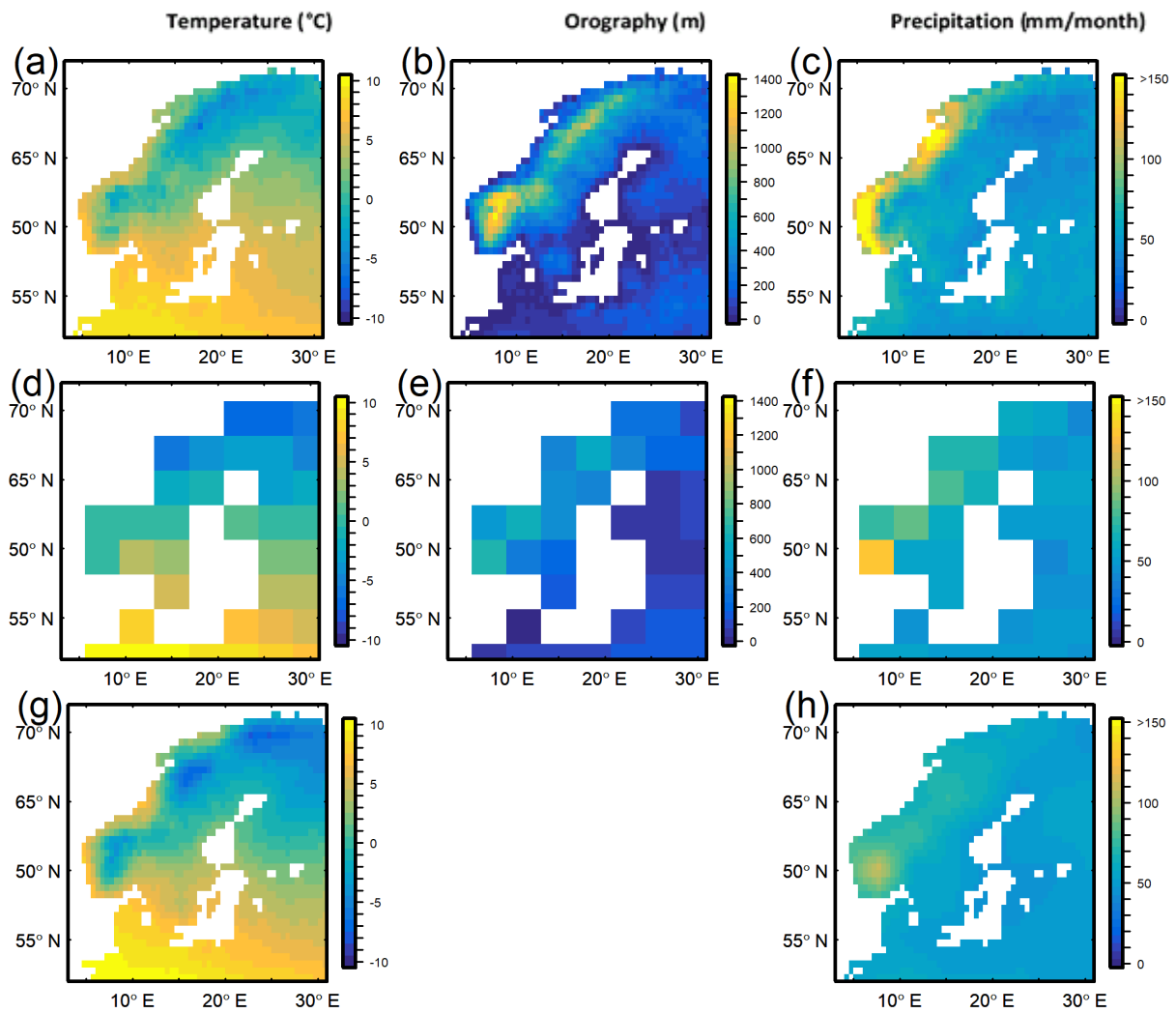
Figure 19. *Evaluation of physical-statistical downscaling technique over Fennoscandia. Top panel: CRU 0.5° gridded observational data (1961–1990 AD), showing (a) mean annual SAT (°C), (b) orography (m), and (c) mean annual precipitation (mm/month). Middle panel: Raw (non-interpolated) HadCM3 data for the pre-industrial control simulation, showing (d) mean annual SAT, (e) modern-day (modice) orography (m), and (f) mean annual precipitation (mm/month). Bottom panel: Predicted climate variables produced using the downscaling model, showing (g) mean annual SAT (°C), and (h) mean annual precipitation (mm/month).*

Various combinations of different variables were tested as predictors ($x,y,z,...m$), following the methods of Thorne et al. (2016) and previous climate research carried out for the oil and gas industry, including high-resolution orography data (Figure 19b; New et al. 1999) which was expected to account for a significant amount of variation. For SAT, the impact of orography is mainly related to the lapse rate, which is the rate at which air temperature decreases with elevation, resulting in generally lower temperatures in mountainous regions. For precipitation, orographic rainfall is expected to be relevant, whereby areas of increased elevation such as mountains force incoming air to rise and cool, leading to condensation. The different regression models were evaluated by comparing the root mean squared error (RMSE) of V_{Calc}, the correlation coefficient for V_{Calc} versus V_{Obs}, and the Bayesian information criterion (BIC) value, which was ultimately used to select the optimal model. BIC measures the relative quality of the fit while favouring models with fewer parameters so as to avoid over-fitting (the lowest score represents the best fit).

For the underlying regression model trained on modern-day conditions, the optimal set of predictors was HadCM3 SAT (Figure 19d), HadCM3 orography (Figure 19e), and CRU orography (Figure 19b). The optimal regression model for precipitation included HadCM3 precipitation (Figure 19f), HadCM3 orography (Figure 19e), CRU orography (Figure 19b), a measure of distance from the coast, and the orographic gradient. When applying the regression models to future climate, the climate data for the relevant timestep was used. For both temperature and precipitation, the high-resolution orography data of Peltier (2004) was used in place of the CRU orography data, to provide orographic data that accounts for changes in the global ice sheets.

For SAT, the optimal model (i.e. that with the lowest BIC) was found to perform well, as can be seen when Figures 19a (T_{Obs}) and Figure 19g (T_{Calc}) are compared, particularly when the relative simplicity of the raw HadCM3 SAT data used in the downscaling is taken into account (Figure 19d). The optimal regression model for precipitation performed less well, as demonstrated when Figures 19c and 19h are compared. While this model is able to reproduce some of the higher orographic precipitation in western Norway, it is not to the same magnitude as seen in the observations. It also appears that the regression model is not able to account fully for rain-shadow and other orographic effects, because relatively high precipitation extends too far eastwards and northwards from the west and south coasts of Norway, whereas observations show a marked decrease in precipitation directly above and to the east of the Norwegian mountain ranges. An improvement in the results for modern-day conditions may be achieved by applying the regression model only over the region of Fennoscandia, but at the expense of results during glacial periods, when the model has difficulty modelling precipitation over the Fennoscandian ice sheet due to the relatively high orographies that are not found during the modern-day period used during optimisation. Thorne et al. (2016) encountered similar issues when downscaling precipitation over Britain, as did Pimenoff et al. (2011) for the region of Europe. It may also be that some of the discrepancy is due to errors in the observational data, particularly over mountainous regions, and also in the underlying GCM simulations. To account for this error, the downscaled results are bias-corrected based on the anomaly between the pre-industrial climate results predicting using the physical-statistical model and the CRU climate data, and the same anomaly is applied for all climate states in the future.

The bias-corrected results (T_{DSBIAS}) are presented as the primary downscaled climate data in Chapter 4. The other downscaling methods, including the bias-correction technique only applied when the ice sheet is not covering the sites and the physical-statistical downscaling, are presented as alternative methodologies and are described in Chapter 5. The strengths and weaknesses of each technique are discussed in detail in Section 5.3.

4 RESULTS

In this chapter, we first discuss the results of the impulse response function and CGSLM (Section 4.1) that give the forcings for the emulator, and then discuss the results of the emulator in Section 4.2, followed by the results downscaled using the bias-correction technique in Section 4.3.

4.1 Forcing data (output from IRF[1] and CGSLM[2])

Atmospheric CO_2 concentration for the RCP scenarios demonstrates an initial increase immediately following the emission period, with RCP2.6 reaching a maximum value of ~440 ppmv at present day and RCP8.5 reaching a maximum of ~1350 ppmv at 1 kyr AP, after which atmospheric CO_2 rapidly declined over approximately the first 50 kyr (Figure 16b). These peak values are taken from the atmospheric CO_2 concentration data used to force the emulator, which has a resolution of 1 kyr. For comparison, Meinshausen et al. (2011) projected peak CO_2 concentrations for the same RCP scenarios of 440 ppmv occurring in year 2052, and 1960 ppmv in year 2250. If the raw output from the IRF is considered, which has an annual resolution for the first ~1 kyr, relatively similar results are found, with CO_2 concentration peaking at 470 ppmv in year 2040 for RCP2.6, and 1970 ppmv in year 2234 for RCP8.5. As stated previously, the 1 kyr temporal resolution of the emulator means that this maximum is not captured. However, it would only be this high for a relatively short period of time (hundreds of years) compared to the timescales being considered here, before CO_2 concentration began to decrease following the end of the emissions period.

Following the early rapid decay of the CO_2 perturbation, atmospheric CO_2 decreases back towards pre-industrial much more slowly. The time at which glacial conditions are first projected to influence CO_2 depends on the total emissions released to the atmosphere. In the natural scenario, which assumes no anthropogenic emissions, GSL falls below pre-industrial immediately after present day (indicating an increase in global ice volume; Figure 16c), accompanied by a reduction in CO_2 concentration. However, this almost immediate projected increase in global ice volume is relatively small, and the current interglacial lasts until approximately 50 kyr AP, with full glacial conditions (<-100 m GSL) not projected to occur until approximately 140 kyr AP. GSL for both the RCP2.6 and RCP4.5 scenarios follows a similar trend to the natural scenario with the current interglacial projected to end in ~50-60 kyr AP. However, the higher atmospheric CO_2 concentrations for these RCP emissions scenarios mean that GSL is also higher than that for the natural scenario, resulting in the next glacial episode being less severe. The anthropogenic CO_2 emissions in RCP8.5 are projected to delay the onset of the next glaciation for nearly 170 kyr into the future, with the first significant drop in GSL and hence CO_2 concentration observed around this time.

---

[1] Section 3.1.1
[2] Section 3.1.3

In all the emissions scenarios, atmospheric CO_2 then fluctuates in synchrony with GSL, with the higher emissions scenarios (particularly RCP8.5) occasionally flattening out due to the occurrence of interglacial conditions and thus the lack of a glacial feedback on CO_2. The CGSLM projects an approximate 100 kyr cyclicity in full glacial conditions following the early period of anthropogenically increased atmospheric CO_2 concentration, although an extended interglacial between approximately 420 and 500 kyr is projected in all scenarios (Figure 16c). Full glacial conditions are accompanied by a decrease in GSL of up to ~130 m, whilst interglacials generally have GSL close to or slightly higher than present-day values. The glacial-interglacial cycles for the natural, low (RCP2.6), and medium (RCP4.5) emissions scenarios are essentially identical in terms of timing from approximately 50 kyr onwards, although with an offset in GSL for several hundreds of thousands of years. RCP8.5 is projected to skip the next glacial cycle, with interglacial conditions maintained for longer than 150 kyr, and demonstrates a smaller decrease in GSL during the next few GSL minima due to the influence of elevated atmospheric CO_2 concentrations. Interestingly, at ~500 kyr AP the GSL of the natural scenario diverges slightly from those of the RCP2.6 and RCP4.5 scenarios, remaining in interglacial conditions slightly longer than the other scenarios and merging with the RCP8.5 scenario. The projections of atmospheric CO_2 concentration and GSL for all four scenarios converge from approximately 600 kyr AP onwards.

4.2 Future climate

4.2.1 Modelled anomalies

The emulators were combined to produce time series data representing the continuous evolution of various climatic variables for the next 1 Myr, based on the orbital, CO_2 and GSL forcings previously described. Figure 20 shows the projected evolution of global mean annual temperature over the next 1 Myr. This is compared to Figure 5a (Section 3.1.3), in order to check that the results of the emulator and the CGSLM are consistent. It can be seen that the temperature projections are generally similar in form, although some minor variations are evident towards the beginning of the simulations when CO_2 emissions are elevated above pre-industrial values. These discrepancies are likely linked to the different ways in which the two models calculate temperature. For the CGSLM, it is calculated as a simple global index scaled from an index of global ice. The emulator, however, simulates the global temperature field, incorporating spatial variations in temperature which can influence the global average. The similar forms of the projections, however, suggest that the two models are relatively consistent.

Figures 21 and 22 illustrate the future evolution of SAT and precipitation at the grid boxes representing the Olkiluoto and Forsmark sites, respectively. The estimated uncertainty in the emulated projections is also shown, defined as 1 SD of the emulated grid box posterior variance. This represents the uncertainty associated with using the emulator to project climate. It therefore does not account for the full uncertainty in the projection, including for example uncertainties in the representation of the ice sheets which may vary between different reconstructions and different models. In this section, all climate variables are presented as an anomaly compared with pre-industrial.
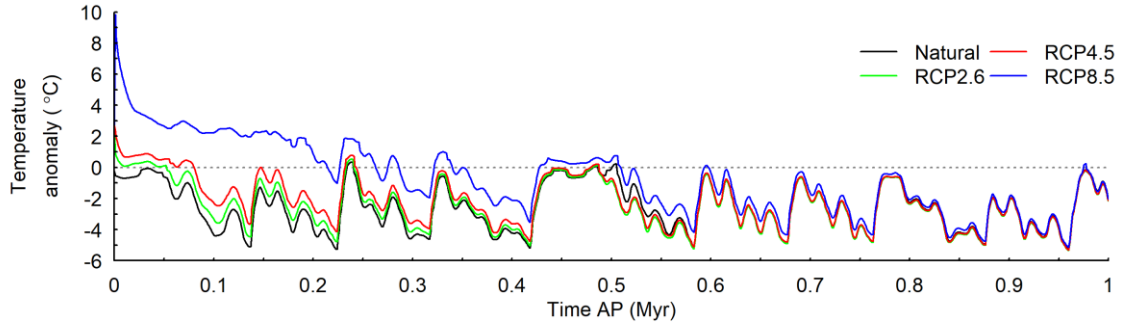
Figure 20. *Time series of emulated mean annual global SAT anomaly (°C) for the next 1 Myr, for the natural (black line), RCP2.6 (green line), RCP4.5 (red line), and RCP8.5 (blue line) emissions scenarios. SAT is modelled every 1 kyr.*
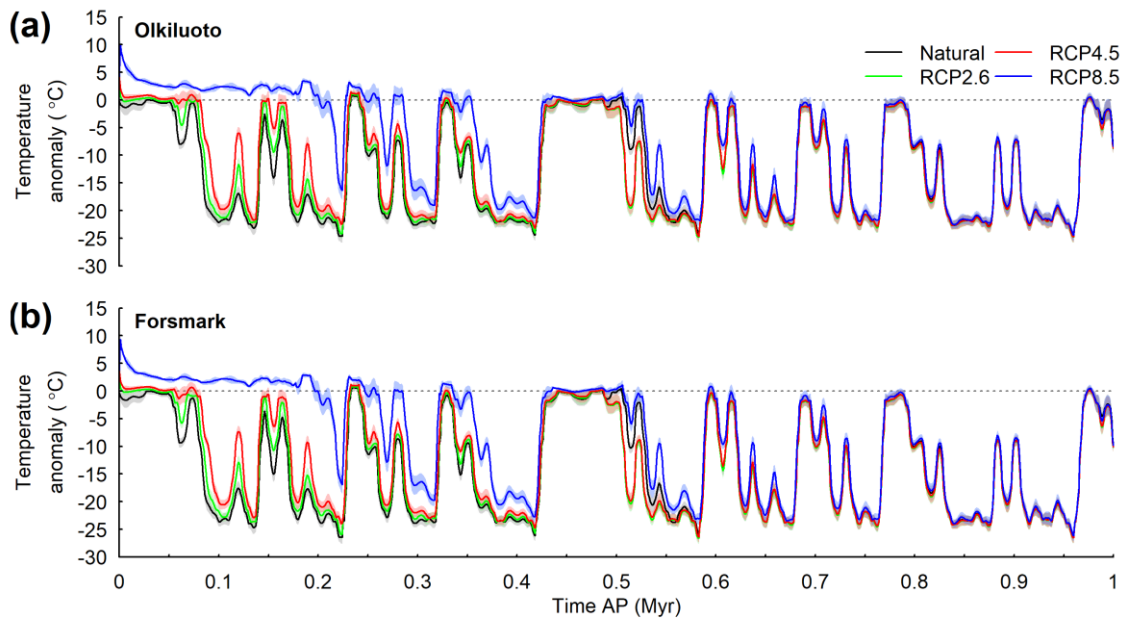
Figure 21. *Time series of emulated mean annual SAT anomaly (°C) for the next 1 Myr at the Olkiluoto ((a)) and Forsmark ((b)) grid boxes, for the natural (black line), RCP2.6 (green line), RCP4.5 (red line), and RCP8.5 (blue line) emissions scenarios. SAT is modelled every 1 kyr. Error bands represent the emulated grid box posterior variance (1 SD). It should be noted that the error bands represent the uncertainty associated with the emulator only, not the overall uncertainty associated with the projections.*

For the early part of the simulation, all the variables for the RCP scenarios exhibit trends similar to that shown by the atmospheric CO_2 concentration (Figure 16b), with a considerable increase over the first few thousand years immediately following emissions. This trend is the result of the increased greenhouse effect caused by the increased atmospheric concentration of CO_2. Mean annual SAT anomaly for the Olkiluoto grid box peaks at 10.0 ± 0.6 °C (above pre-industrial) for RCP8.5 and 4.2 ± 0.2 °C for RCP2.6 (Figure 21a), whilst for the Forsmark grid box SAT peaks at 9.3 ± 0.6 °C and 3.7 ± 0.2 °C, respectively (Figure 21b). The maximum precipitation anomaly during the early part of the simulation for Olkiluoto is 20.0 ± 0.5 mm/month (above pre-industrial) for RCP8.5

and 4.6 ± 0.5 mm/month for RCP2.6, and for Forsmark is 19.8 ± 0.5 mm/month and 5.1 ± 0.5 mm/month (Figure 22).

A relatively rapid decline then occurs in the RCP scenarios for up to ~50 kyr AP, which is the result of a large proportion of the atmospheric CO_2 perturbation being taken up from the atmosphere by carbon cycle processes, described in detail in Lord et al. (2016). Following this, the variables generally gradually decrease back towards pre-industrial values, with oscillations resulting from variations in the orbital parameters and the glacial-interglacial cycles becoming increasingly dominant as the simulation progresses and the anthropogenic CO_2 perturbation declines. In contrast, the natural scenario responds to orbital and glacial forcing immediately after 0 kyr AP, demonstrating cooler than present-day conditions resulting from the decreased CO_2 and GSL associated with the relatively low insolation forcing.
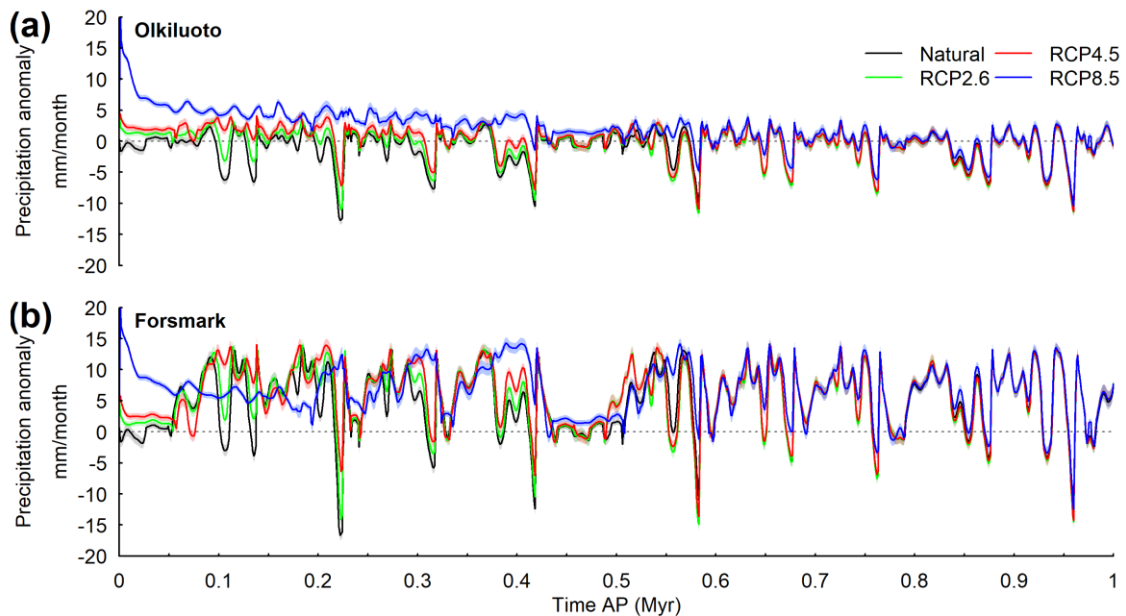
Figure 22. *Time series of emulated mean annual precipitation anomaly (mm/month) for the next 1 Myr at the Olkiluoto ((a)) and Forsmark ((b)) grid boxes, for the natural (black line), RCP2.6 (green line), RCP4.5 (red line), and RCP8.5 (blue line) emissions scenarios. Precipitation is modelled every 1 kyr. Error bands represent the emulated grid box posterior variance (1 SD). It should be noted that the error bands represent the uncertainty associated with the emulator only, not the overall uncertainty associated with the projections.*

Following the early period of the simulations when anthropogenic CO_2 has a large impact on climate, variations in SAT at the two sites for all scenarios demonstrate a similar pacing to fluctuations in GSL and CO_2, with minima in SAT occurring approximately every 100 kyr (in the absence of anthropogenic CO_2 forcing) in synchrony with full glacial conditions. SAT anomalies of approximately -24 to -27 °C (1 SD = ~1 °C) are projected to occur during glacial periods as a result of the growth of the Fennoscandian ice sheet over the region. The ice sheet reduces the albedo of the land surface resulting in increased reflection of solar radiation, and increases the altitude of the modelled land surface due to the buildup of thick ice, both resulting in cooling. The natural decrease in CO_2 concentration during glaciations also plays a role.

A decrease in precipitation of up to -16.50 ± 0.8 mm/month is also projected. This may be caused by cooler global temperatures resulting in reduced evaporation of sea water and thus lower atmospheric water vapour in the region. Other regional processes also play a role, such as the increased altitude of the ice sheet resulting in increased rainfall on the south-west boundary of the ice sheet (direction of prevailing wind), leading to lower air moisture and therefore precipitation over the ice sheet (rain shadow effect). This process can be clearly seen on Figures 24b, 24c, 25b and 25c, which illustrate SAT and precipitation anomalies over Europe associated with a decrease in GSL of ~46 m and ~122 m (Figures 23b and 23c), respectively. A slight increase in precipitation can be observed in Figure 25b over parts of southern Norway and Sweden and the North Sea, along the south-eastern boundary of the ice sheet in Figure 23b. This region of increased rainfall has then increased in intensity slightly further south in Figure 25c, accompanied by an extension of the strongly cooled area southwards (Figure 24c) as the ice sheet expands (Figure 23c). It appears that the Forsmark site is more strongly affected by the rain shadow effect, as during glacial conditions prior to full glacial conditions the precipitation anomaly in Figure 22b is significantly higher than the pre-industrial baseline (grey dotted line), whilst during interglacial conditions it is approximately in line with the pre-industrial baseline. However, such a significant increase in precipitation is not evident at the Olkiluoto site (Figure 25a). This is further supported by Figure 25b, which shows the positive precipitation anomaly over the Forsmark grid box but not the Olkiluoto grid box.
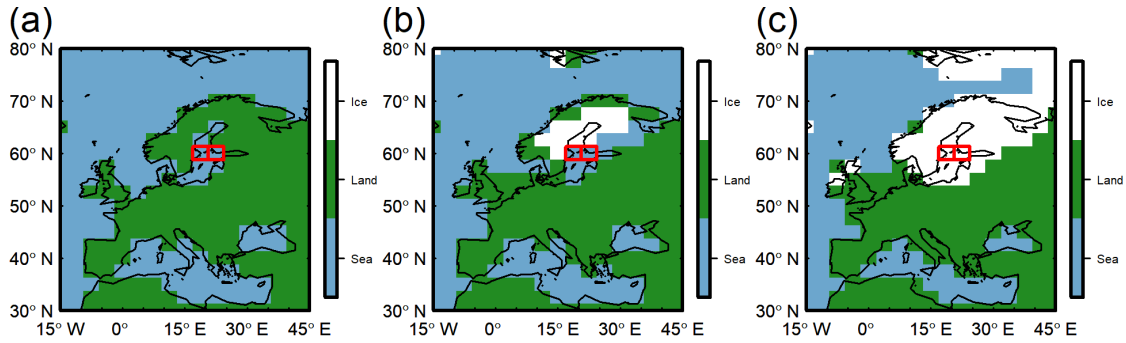
Figure 23. *Surface types for the region of Europe showing land/sea boundaries and ice sheet extent. The two site grid boxes are also shown in red. Snapshots have GSL values of: (a) +24 m (e.g. 5 kyr AP), (b) -46 m (e.g. 215 kyr AP), and (c) -122 m (e.g. 960 kyr AP).*
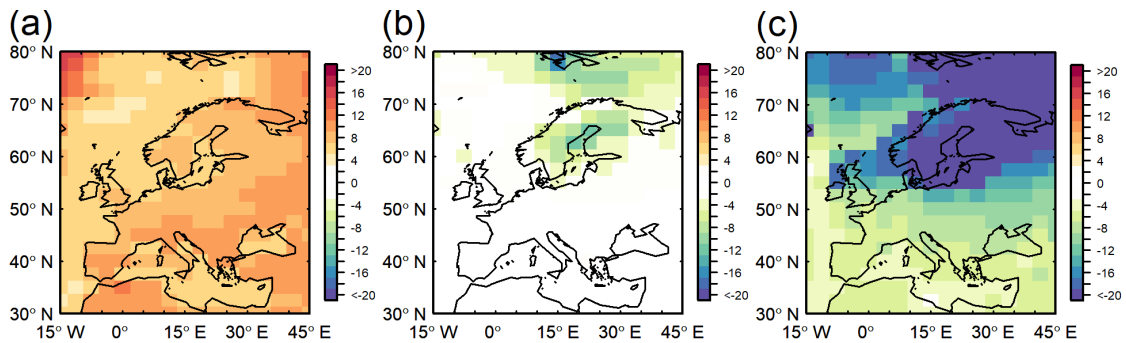
Figure 24. *Emulated mean annual SAT anomaly (°C) for the region of Europe for the RCP8.5 emissions scenario. Snapshots have GSL values of: (a) +24 m (5 kyr AP), (b) -46 m (215 kyr AP), and (c) -122 m (960 kyr AP).*
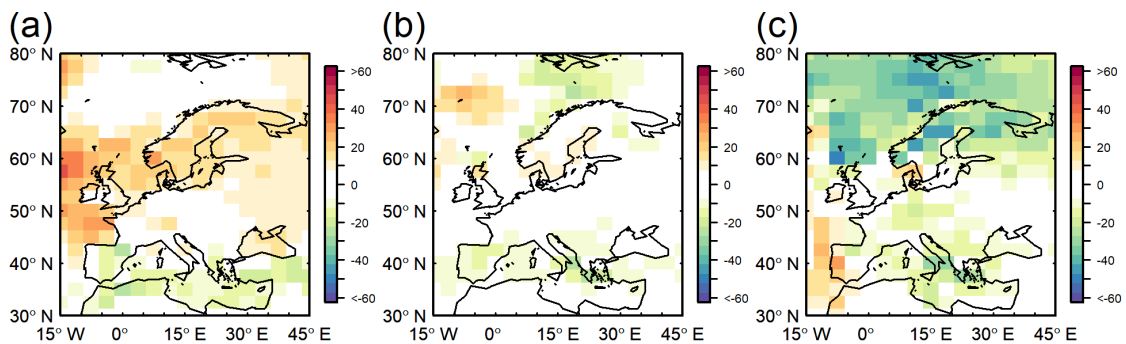
Figure 25. *Emulated mean annual precipitation anomaly (mm/month) for the region of Europe for the RCP8.5 emissions scenario. Snapshots have GSL values of: (a) +24 m (5 kyr AP), (b) -46 m (215 kyr AP), and (c) -122 m (960 kyr AP).*

Figures 26 and 27 show the wavelet power spectra for the SAT anomaly data shown in Figure 21 and the precipitation anomaly data shown in Figure 22 for the two sites. The standard MATLAB wavelet software of Torrence and Compo (1998) (available online at http://atoc.colorado.edu/research/wavelets) was used. This type of analysis allows the dominant orbital frequencies influencing climate to be identified. From Figure 21, it can be seen that the change in SAT for approximately the first 100 kyr is driven largely by the increased atmospheric CO_2 concentration. From approximately 100 kyr onwards, precession has an increased impact on the pacing of SAT fluctuations (periodicity of ~20 kyr; Figure 26), particularly during the periods when eccentricity is relatively high. During these periods, eccentricity also has an increased influence (periodicity of ~100 kyr), demonstrated by the generally larger amplitudes of the temperature fluctuations (Figure 21). There is evidence of obliquity forcing (periodicity of ~40 kyr) at times when obliquity is relatively high, such as between ~200 and 300 kyr AP. The oscillations in precipitation over the next 1 Myr appear to show stronger precessional forcing compared to SAT (Figures 22 and 27), which is at its strongest when eccentricity is high (Figure 16a). As with SAT, there is also evidence of eccentricity forcing (Figure 27). The emulator uncertainty associated with SAT shown in Figure 21 and precipitation in Figure 22 is relatively low when compared with the magnitude of the variations caused by anthropogenic warming and glacial-interglacial fluctuations.

Figures 24 and 25 show snapshots of climate over Europe for the RCP8.5 scenario at three future times (5, 215 and 960 kyr AP), selected because they illustrate the full range of projected GSL values. The ice sheet extents for the selected GSLs are illustrated in Figure 23. Figures 24a and 25a are associated with the maximum increase in GSL of 24 m (Figure 23a), which occurs shortly after the emissions period when atmospheric CO_2 concentration is significantly higher than pre-industrial. This results in partial melting of the GrIS, the warming signature for which can just be seen in the north-west corner of Figure 24a. Increased warming over land areas occurs, along with increased precipitation in some regions including the North Atlantic and Fennoscandia.
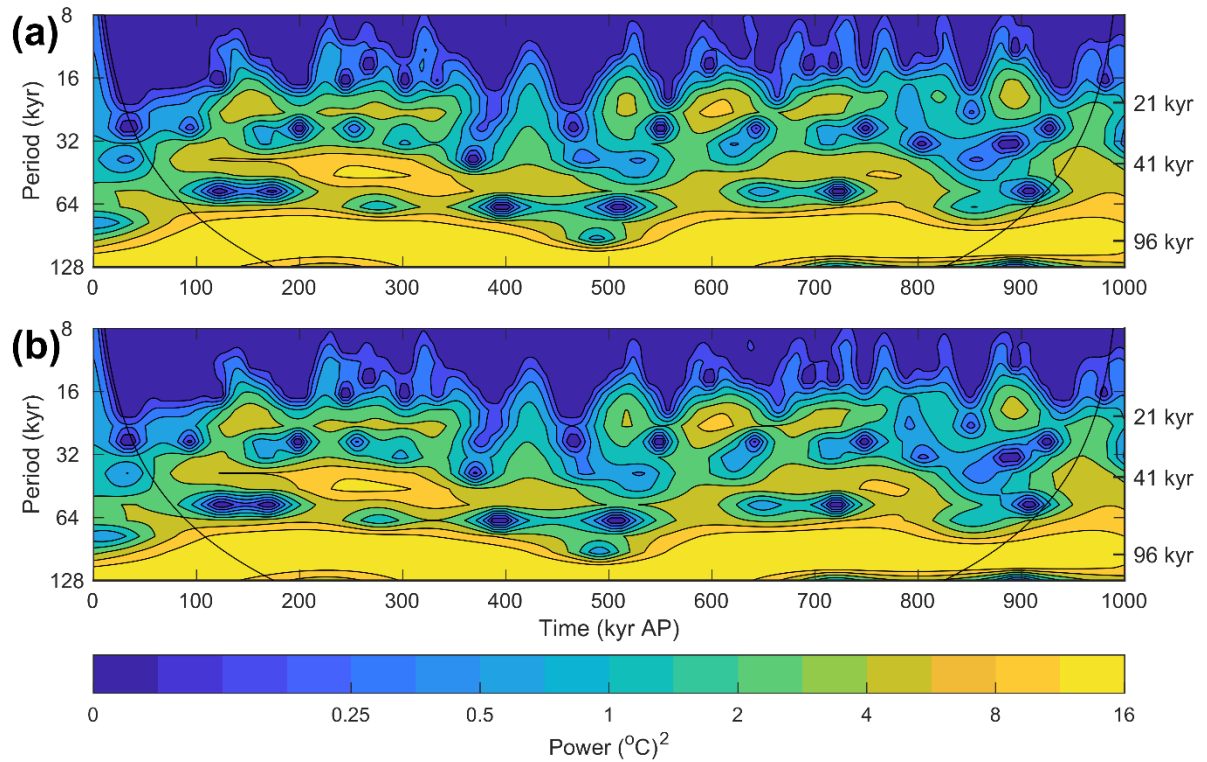
Figure 26. The wavelet power spectrum for emulated mean annual SAT anomaly (°C) the next 1 Myr for the Olkiluoto ((a)) and Forsmark ((b)) grid boxes, for the RCP2.6 emissions scenario (green line in Figure 21). SAT is normalised separately for each site by the standard deviation of the analysed SAT data ((a) = 8.8 °C; (b) = 9.1 °C).
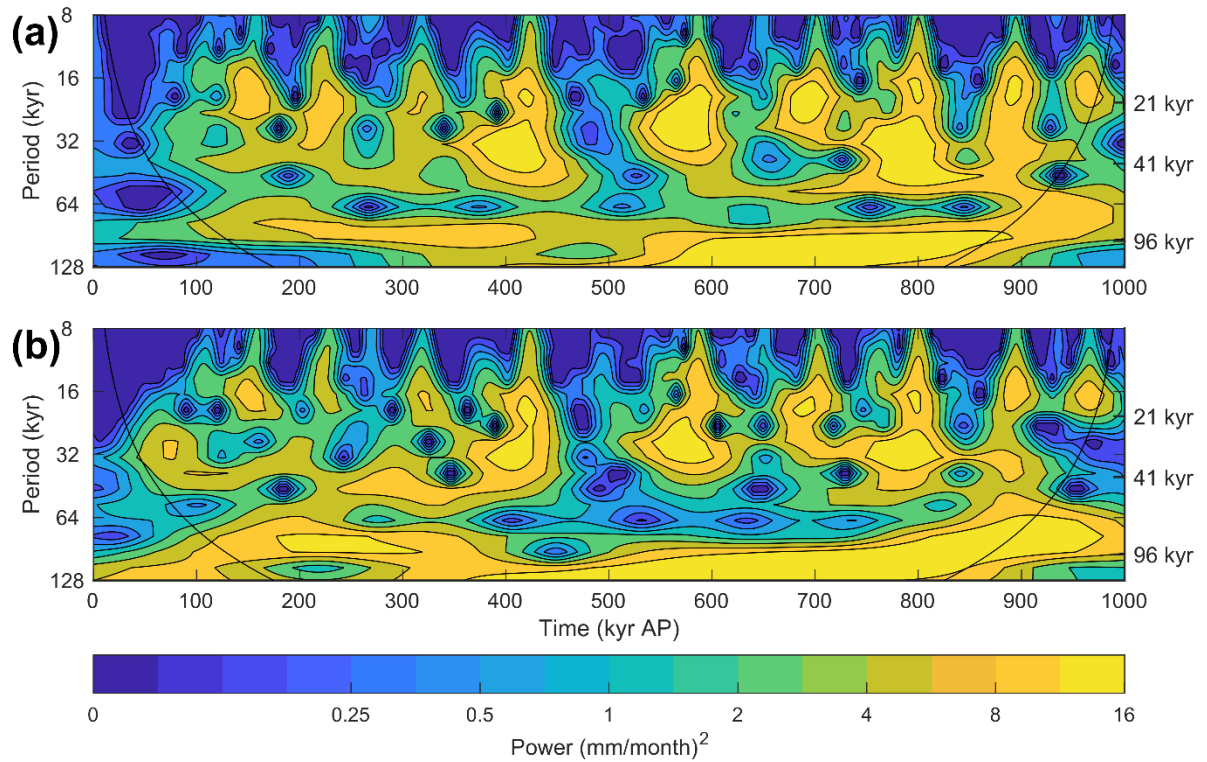
Figure 27. *The wavelet power spectrum for emulated mean precipitation anomaly (mm/month) the next 1 Myr for the Olkiluoto ((a)) and Forsmark ((b)) grid boxes, for the RCP2.6 emissions scenario (green line in Figure 22). Precipitation is normalised separately for each site by the standard deviation of the analysed precipitation data ((a) =2.5 mm/month; (b) = 5.1 mm/month).*

Figures 24b, 24c, 25b, and 25c show glacial conditions, with GSL of -46 m and -122 m (Figures 23b and 23c), respectively. Cooling can be seen over Fennoscandia and the Barents Sea (Figure 24b) as the Fennoscandian ice sheet starts to build up (Figure 23b), which then intensifies to >-20 °C and extends to cover much of the high northern latitudes (Figure 24c) as the ice sheet reaches full size (Figure 23c). As mentioned previously, a decrease in precipitation over much of the cooled area also occurs, along with a few regions of increased rainfall in the North Atlantic and to the south-east of the ice sheet (Figure 25c).

4.2.2 Downscaled climate

In order to produce high-resolution projections of future climate, the emulator results were downscaled using the bias-correction technique described in Section 3.3.1, which downscales data to regional scale, from which site scale data can be extracted. The results of a number of alternative downscaling techniques, including physical-statistical downscaling (Section 3.3.2), are presented in Section 5.3 along with a discussion of the uncertainty in the projections.

Figures 28 to 35 illustrate the downscaled climate data, using the CRU 0.5° gridded climatology for 1961–1990 (New et al. 1999). Figures 28 to 31 show the downscaled climate in response to the forcings illustrated in Figure 16, whilst Figures 32 to 35 show the downscaled climate but assuming that there is no ice coverage at the sites. For this "no-ice" data, the emulator was forced with the same forcings as presented in Figure 16, except when GSL fell below -46 m (i.e. the lowest GSL at which ice coverage does not occur at the sites in the Singarayer and Valdes (2010) simulations, shown in Figure 9a) it was set to -46 m to prevent the simulation of ice sheet coverage at the sites (thus the minimum GSL was -46 m). These "no-ice" results were included to provide information about what the air temperature at the land surface may be if the ice sheet did not quite extend to the sites of interest during glaciations.

In Figures 28 to 35, periods when the ice sheet is projected to be overlying the sites are highlighted by the vertical shaded bands, calculated by applying the relatively simple threshold approach to GSL (Figure 16c) that was described and validated in Section 3.1.3. The vertical bands are the same for the ice-covered and non-ice-covered versions of the SAT and precipitation results, since they are based on GSL, and thus highlight when the differences between these results occur. Periods of higher confidence ice coverage (GSL < -93 m) are illustrated by purple bands, whilst periods of lower confidence ice coverage (-93 m < GSL < -53 m) are represented by cyan bands. The projected timings of these periods of glacial conditions at the sites are detailed in Table 2, including the duration. During ice-covered conditions the climate results are associated with higher uncertainty, since the downscaling bias correction is calibrated on modern-day climate. Downscaled climate for the region of Fennoscandia is shown in Figure 36 (SAT) and Figure 37 (precipitation) for different climate states, including warm interglacial (top panel) and glacial (bottom panel).
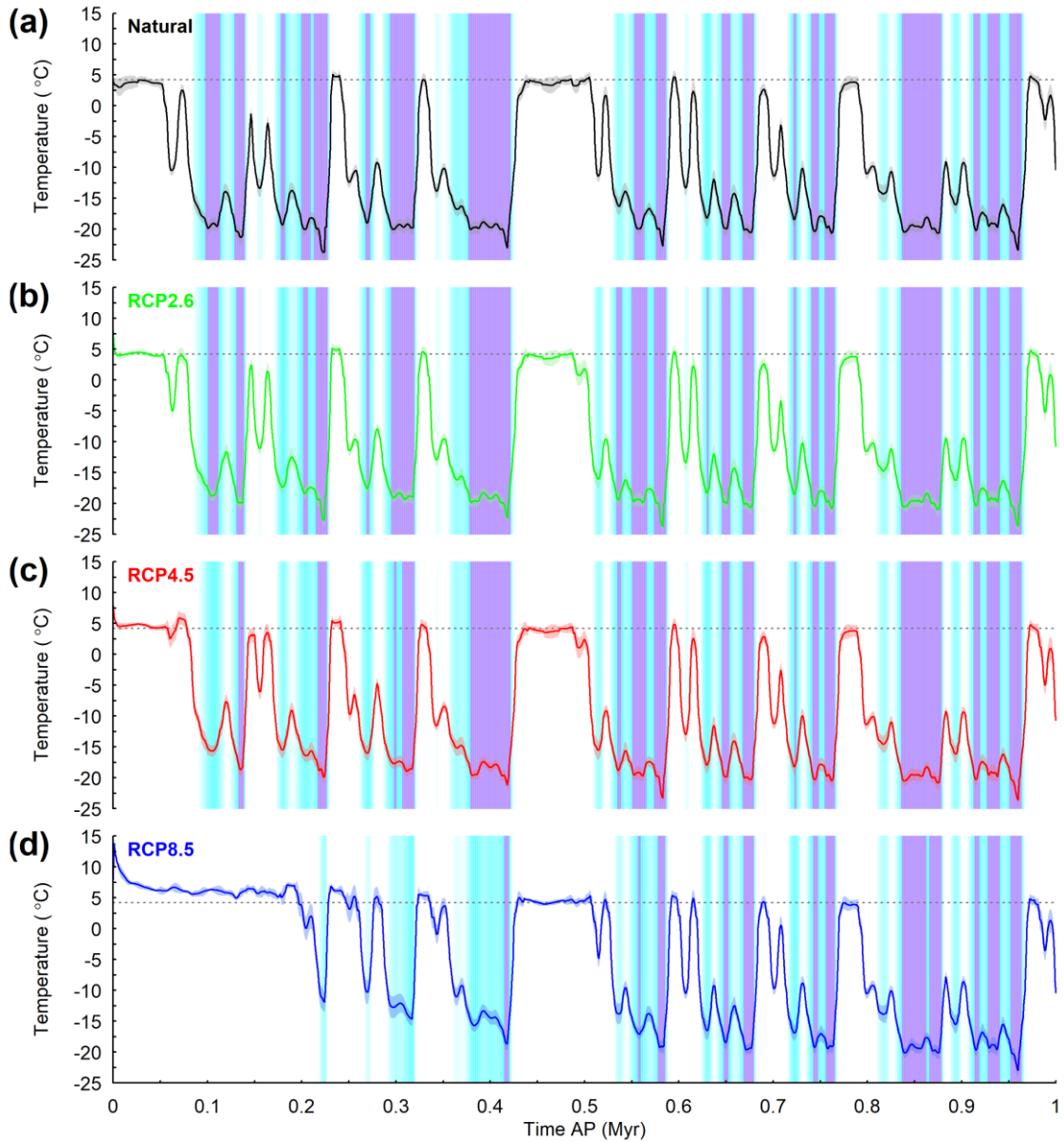
Figure 28. *Time series of emulated downscaled mean annual SAT (°C) for the next 1 Myr at the Olkiluoto site, for the natural ((a)), RCP2.6 ((b)), RCP4.5 ((c)), and RCP8.5 ((d)) emissions scenarios, downscaled using the bias-correction technique. SAT is modelled every 1 kyr. Error bands represent the emulated grid box posterior variance (1 SD). Vertical bands represent periods when the Fennoscandian ice sheet is covering the site, with purple shading indicating higher confidence (GSL < -93 m) and cyan shading indicating lower confidence (-93 m < GSL < -53 m) ice coverage. A higher degree of cyan shading indicates lower uncertainty. The grey dotted line represents present-day mean annual SAT at the site (4.2 °C) taken from the CRU 0.5° gridded climatology for the period 1961–1990 (New et al. 1999).*

The temperature and precipitation projections are very similar in form to the anomalies exhibited in the previous section. The warmest conditions are experienced at the very start of the time period, either at present day for RCP2.6 and RCP4.5, or 1 kyr AP for RCP8.5 (Figures 28 and 29). At Olkiluoto, maximum absolute temperatures at these times are 7.9 °C and 13.8 °C for RCP2.6 and RCP8.5, whilst the temperature at Forsmark is 9.5 °C and 16.0 °C. The warmest timestep for RCP2.6 and RCP4.5 (at 0 kyr AP) are the same since they both have the same modern-day forcing conditions, although after this time the climates diverge. This can clearly be seen in Figures 36a and 36b, and Figures 37a and 37b. When considering SAT, cooler temperatures over the Norwegian mountain ranges can be seen relative to the lower elevation (Figures 36a to 36c).
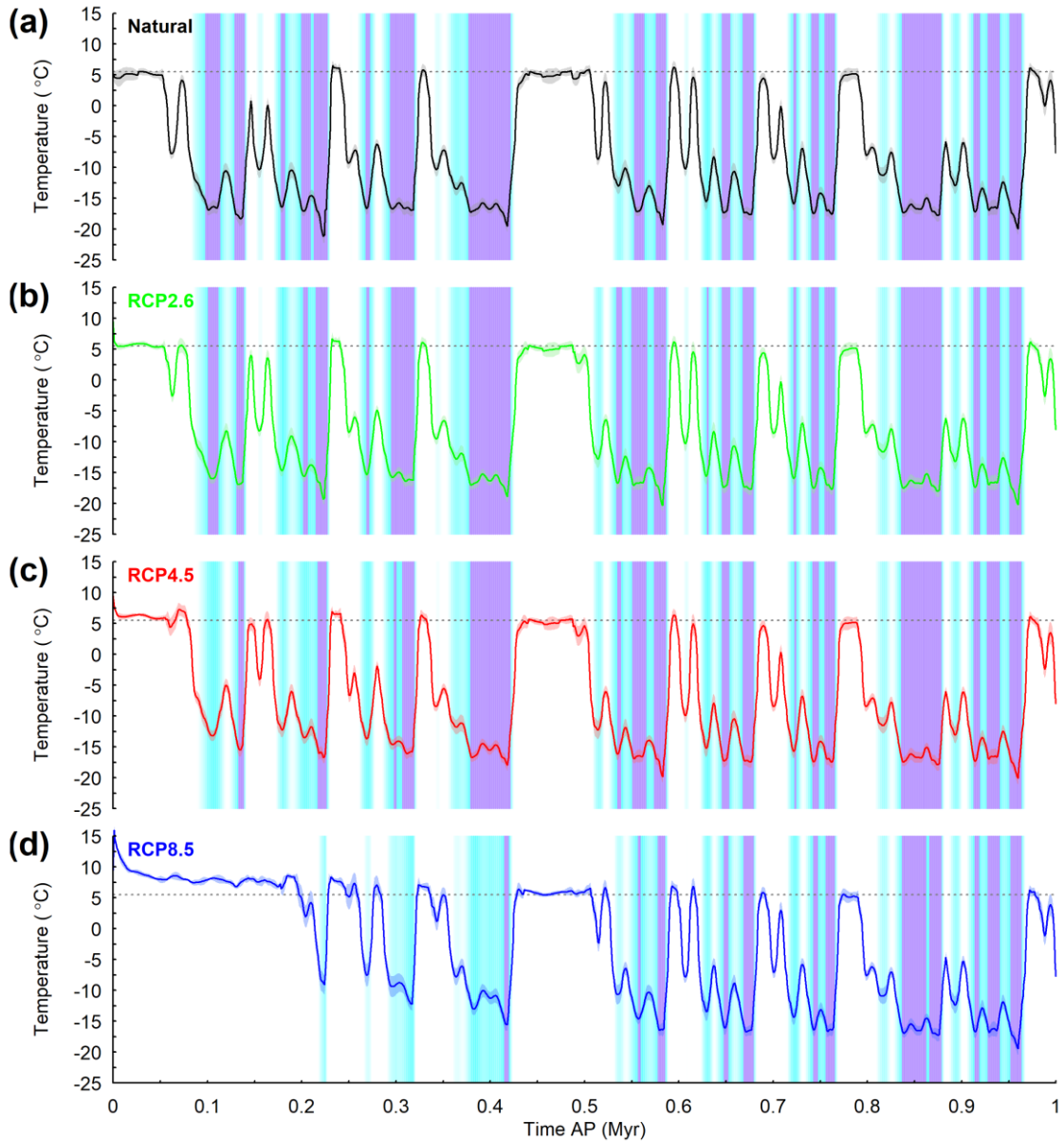
Figure 29. *Time series of emulated downscaled mean annual SAT (°C) for the next 1 Myr at the Forsmark site, for the natural ((a)), RCP2.6 ((b)), RCP4.5 ((c)), and RCP8.5 ((d)) emissions scenarios, downscaled using the bias-correction technique. SAT is modelled every 1 kyr. Error bands represent the emulated grid box posterior variance (1 SD). Vertical bands represent periods when the Fennoscandian ice sheet is covering the site, with purple shading indicating higher confidence (GSL < -93 m) and cyan shading indicating lower confidence (-93 m < GSL < -53 m) ice coverage. A higher degree of cyan shading indicates lower uncertainty. The grey dotted line represents present-day mean annual SAT at the site (5.5 °C) taken from the CRU 0.5° gridded climatology for the period 1961–1990 (New et al. 1999).*

Figure 30. *Time series of emulated downscaled mean annual precipitation (mm/month) for the next 1 Myr at the Olkiluoto, for the natural ((a)), RCP2.6 ((b)), RCP4.5 ((c)), and RCP8.5 ((d)) emissions scenario, downscaled using the bias-correction technique. SAT is modelled every 1 kyr. Error bands represent the emulated grid box posterior variance (1 SD). Vertical bands represent periods when the Fennoscandian ice sheet is covering the site, with purple shading indicating higher confidence (GSL < -93 m) and cyan shading indicating lower confidence (-93 m < GSL < -53 m) ice coverage. A higher degree of cyan shading indicates lower uncertainty. The grey dotted line represents present-day mean annual precipitation at the site (45 mm/month) taken from the CRU 0.5° gridded climatology for the period 1961–1990 (New et al. 1999).*

In Section 4.1, the CGSLM estimated that the next glacial inception may occur at ~50 kyr AP for RCP2.6, ~60 kyr AP for RCP4.5, and ~170 kyr AP for RCP8.5. However, based on the GSL threshold analysis, and only taking into account periods of higher confidence ice coverage, the ice sheet is not projected to expand as far as the Olkiluoto and Forsmark sites until ~100 kyr AP for RCP2.6, ~130 kyr AP for RCP4.5, and ~410 kyr AP for RCP8.5 (Figures 28-35, Table 2). The SATs over Fennoscandia for these times are illustrated in Figure 36 (bottom panel), where the relatively low temperatures over the extensive Fennoscandian ice sheet can be clearly seen. Temperature minima at Olkiluoto projected to occur just prior to this ice sheet coverage range from -16.2 °C for RCP8.5 to -16.5 °C for RCP2.6, and at Forsmark from -15.6 °C for RCP8.5 to -16.0 °C for RCP2.6, although the timing of these minima varies between the scenarios.
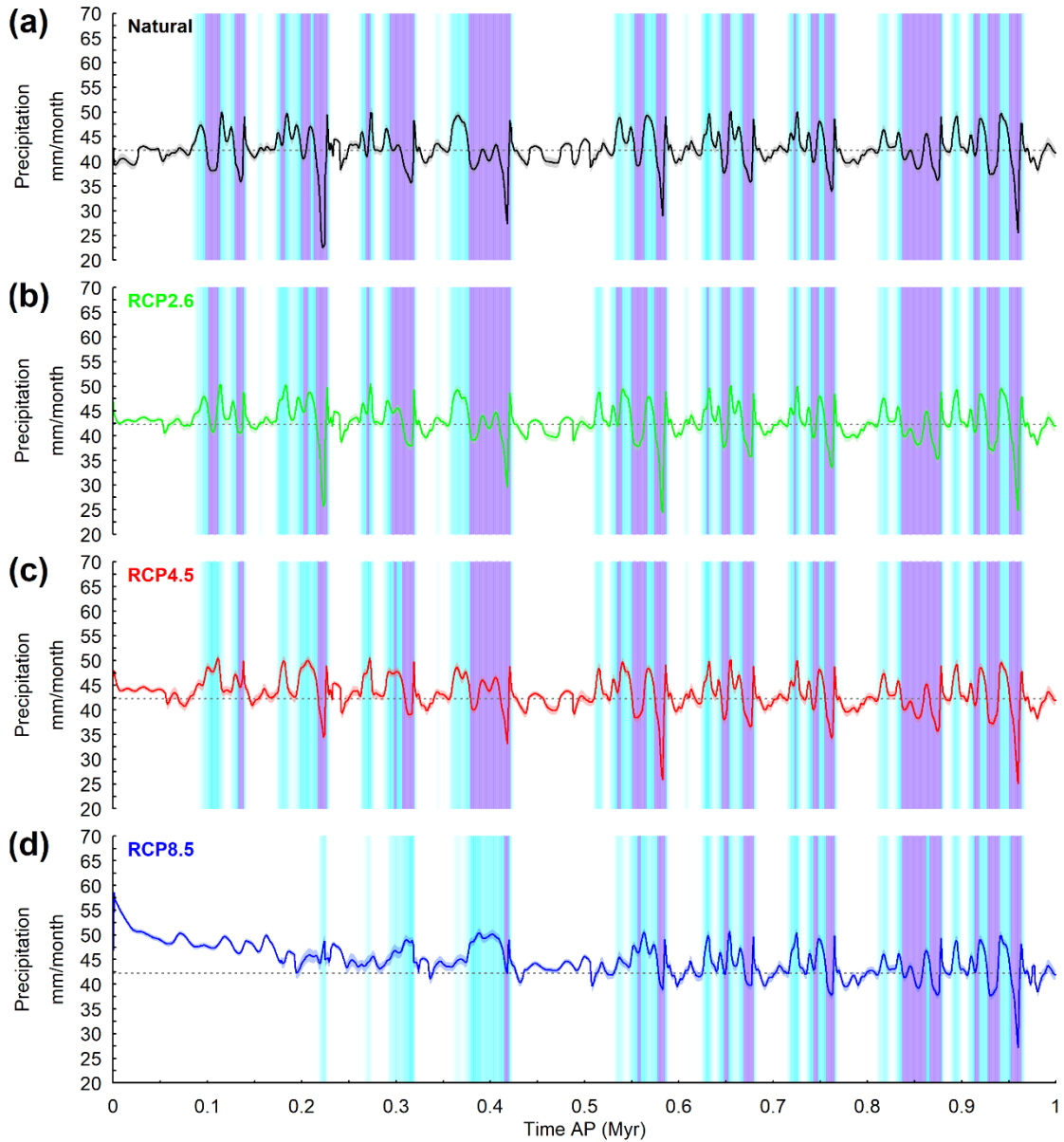
Figure 31. *Time series of emulated downscaled mean annual precipitation (mm/month) for the next 1 Myr at the Forsmark site, for the natural ((a)), RCP2.6 ((b)), RCP4.5 ((c)), and RCP8.5 ((d)) emissions scenarios, downscaled using the bias-correction technique. SAT is modelled every 1 kyr. Error bands represent the emulated grid box posterior variance (1 SD). Vertical bands represent periods when the Fennoscandian ice sheet is covering the site, with purple shading indicating higher confidence (GSL < -93 m) and cyan shading indicating lower confidence (-93 m < GSL < -53 m) ice coverage. A higher degree of cyan shading indicates lower uncertainty. The grey dotted line represents present-day mean annual precipitation at the site (42 mm/month) taken from the CRU 0.5° gridded climatology for the period 1961–1990 (New et al. 1999).*

For RCP2.6 and RCP4.5, there is also an earlier period of cooler-than-modern temperatures at both sites, occurring approximately 60 kyr AP, several tens of thousands of years before ice coverage is first recorded at the sites in the two scenarios. The Fennoscandian ice sheet has partially developed at this time, but has either not yet expanded as far as the two sites, or else the confidence that ice coverage occurs is very low. Following glaciation, interglacial conditions are experienced as SAT increases back towards modern-day values for a time, after which cooling occurs once more. In terms of the timing of glacial conditions at the sites, ice sheet coverage is fairly variable, ranging from a few thousand years up to 60 kyr or longer (Table 2), based on the GSL threshold method.
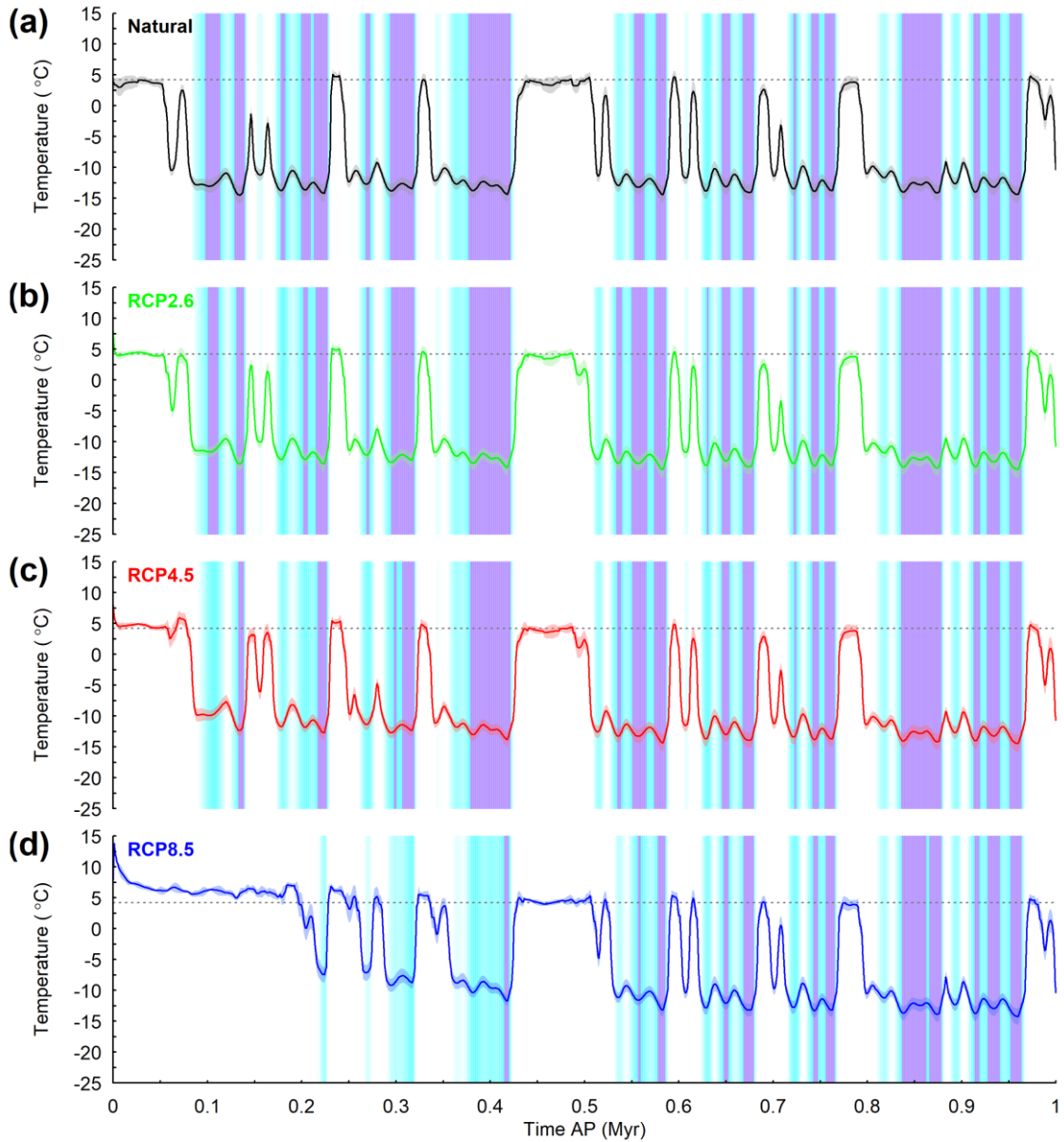
Figure 32. *Time series of emulated downscaled mean annual SAT (°C) for the next 1 Myr assuming no ice cover during glacial conditions at the Olkiluoto site, for the natural ((a)), RCP2.6 ((b)), RCP4.5 ((c)), and RCP8.5 ((d)) emissions scenarios, downscaled using the bias-correction technique. During glacial periods, GSL is allowing to reach a minimum of -46 m and is then held constant until it increases towards interglacial conditions. SAT is modelled every 1 kyr. Error bands represent the emulated grid box posterior variance (1 SD). Vertical bands represent periods when the Fennoscandian ice sheet is covering the site, with purple shading indicating higher confidence (GSL < -93 m) and cyan shading indicating lower confidence (-93 m < GSL < -53 m) ice coverage. A higher degree of cyan shading indicates lower uncertainty. The grey dotted line represents present-day mean annual SAT at the site (4.2 °C) taken from the CRU 0.5° gridded climatology for the period 1961–1990 (New et al. 1999).*

Figure 33. *Time series of emulated downscaled mean annual SAT (°C) for the next 1 Myr assuming no ice cover during glacial conditions at the Forsmark site, for the natural ((a)), RCP2.6 ((b)), RCP4.5 ((c)), and RCP8.5 ((d)) emissions scenarios, downscaled using the bias-correction technique. During glacial periods, GSL is allowing to reach a minimum of -46 m and is then held constant until it increases towards interglacial conditions. SAT is modelled every 1 kyr. Error bands represent the emulated grid box posterior variance (1 SD). Vertical bands represent periods when the Fennoscandian ice sheet is covering the site, with purple shading indicating higher confidence (GSL < -93 m) and cyan shading indicating lower confidence (-93 m < GSL < -53 m) ice coverage. A higher degree of cyan shading indicates lower uncertainty. The grey dotted line represents present-day mean annual SAT at the site (5.5 °C) taken from the CRU 0.5° gridded climatology for the period 1961–1990 (New et al. 1999).*

Figures 30 and 31 illustrate projected precipitation at the two sites over the next 1 Myr, whereas Figure 37 illustrates precipitation for the whole of Fennoscandia. The warmest period for each scenario is also associated with relatively high precipitation, ranging from 50 mm/month to 67 mm/month at Olkiluoto, and 47 mm/month to 59 mm/month at Forsmark (Figures 29 and 31). In Figure 37 (top panel), it can be seen that the highest precipitation occurs in the south of Norway and to the west of the Norwegian mountains, with more modest increases in Sweden and Finland when RCP2.6 is compared to RCP8.5.
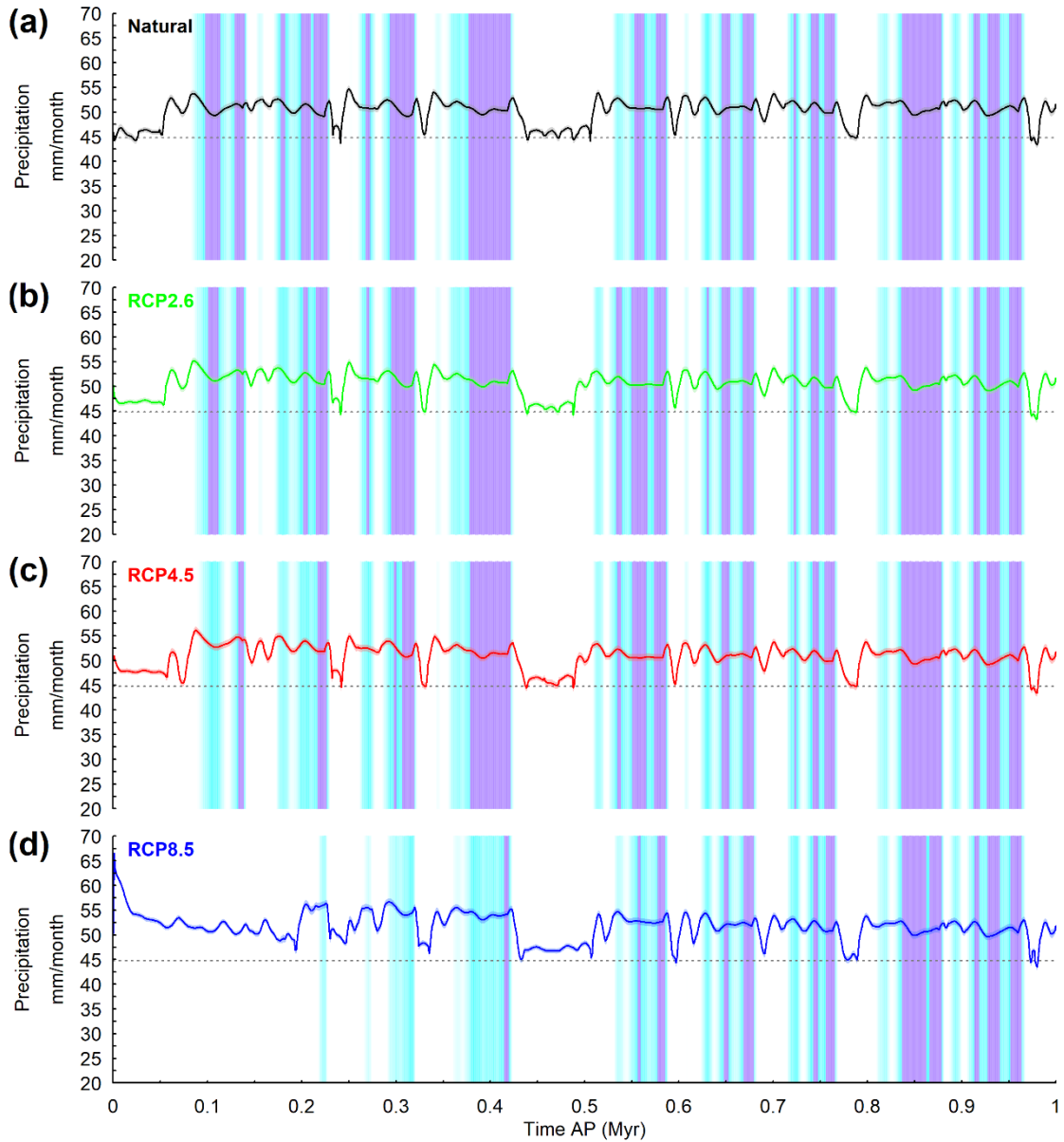
Figure 34. *Time series of emulated downscaled mean annual precipitation (mm/month) for the next 1 Myr assuming no ice cover during glacial conditions at the Olkiluoto site, for the natural ((a)), RCP2.6 ((b)), RCP4.5 ((c)), and RCP8.5 ((d)) emissions scenarios, downscaled using the bias-correction technique. During glacial periods, GSL is allowing to reach a minimum of -46 m and is then held constant until it increases towards interglacial conditions. SAT is modelled every 1 kyr. Error bands represent the emulated grid box posterior variance (1 SD). Vertical bands represent periods when the Fennoscandian ice sheet is covering the site, with purple shading indicating higher confidence (GSL < -93 m) and cyan shading indicating lower confidence (-93 m < GSL < -53 m) ice coverage. A higher degree of cyan shading indicates lower uncertainty. The grey dotted line represents present-day mean annual precipitation at the site (45 mm/month) taken from the CRU 0.5° gridded climatology for the period 1961–1990 (New et al. 1999).*

During glacial conditions when prolonged (higher confidence) ice is present at the sites, a decrease in precipitation compared to interglacial conditions is seen (Figures 30 and 31), since the presence of the ice sheet increases the orography in the region, resulting in increased orographic rainfall in ice-free areas and at the ice sheet margin and reduced precipitation in high altitude areas (Figure 37; bottom panel). Prior to this decrease, an increase in precipitation is observed as the ice sheet margin approaches the sites, as discussed in the previous section. Precipitation at Olkiluoto is estimated to be ~46 – 47 mm/month immediately prior to the first timestep with ice sheet coverage for all emissions scenarios (see earlier in the section for timings of first glaciations), and ~53 mm/month at Forsmark. Following this period of ice coverage at the sites, precipitation generally increases back towards approximately modern-day values at Forsmark as the climate system moves into an interglacial state before it begins the transition back towards glacial conditions. Compared to the Forsmark site, the increase in precipitation above pre-industrial values at Olkiluoto occurs earlier in the glacial cycle, during peri-glacial conditions (i.e. within the white bands).
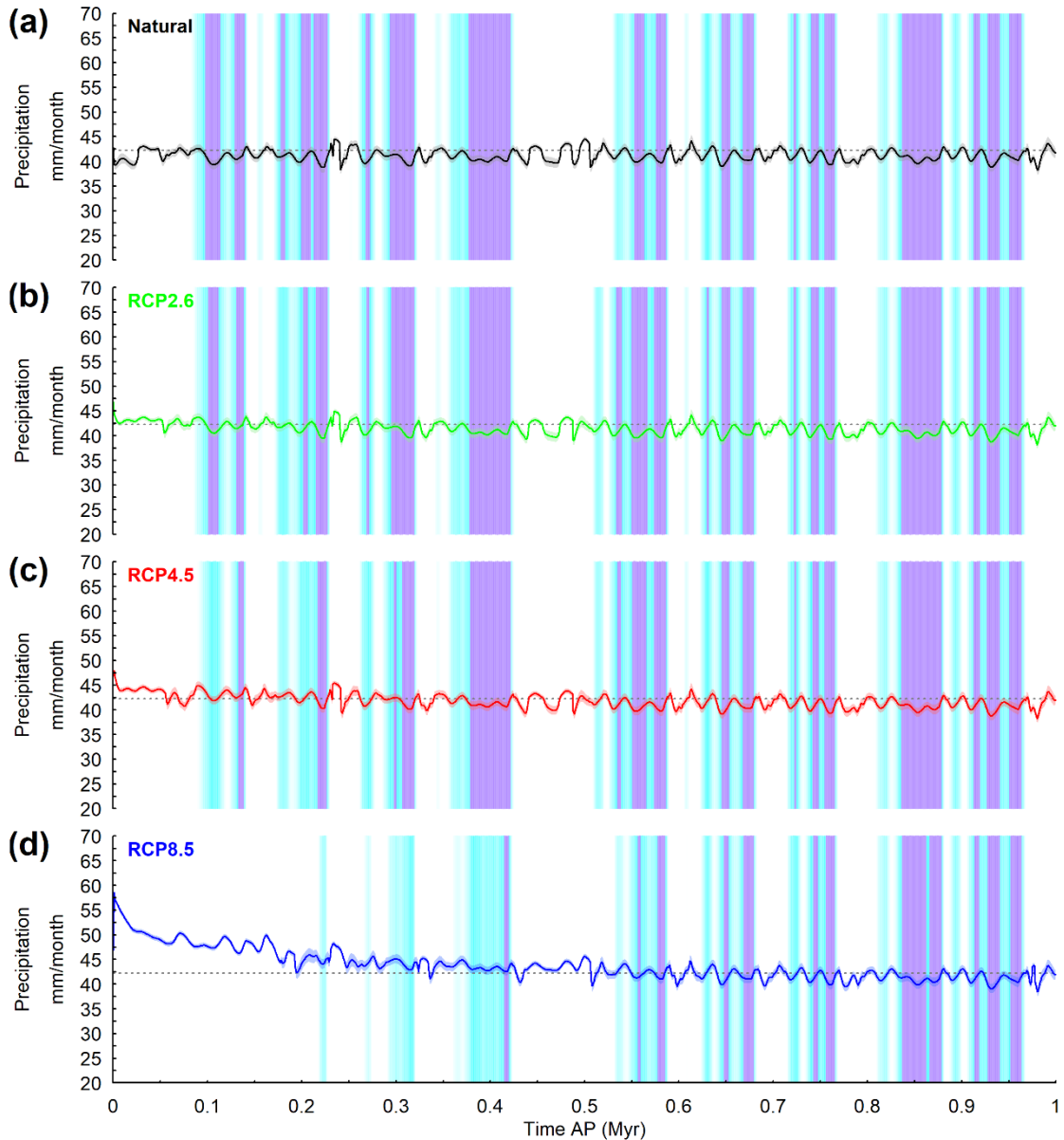
Figure 35. *Time series of emulated downscaled mean annual precipitation (mm/month) for the next 1 Myr assuming no ice cover during glacial conditions at the Forsmark site, for the natural ((a)), RCP2.6 ((b)), RCP4.5 ((c)), and RCP8.5 ((d)) emissions scenarios, downscaled using the bias-correction technique. During glacial periods, GSL is allowing to reach a minimum of -46 m and is then held constant until it increases towards interglacial conditions. SAT is modelled every 1 kyr. Error bands represent the emulated grid box posterior variance (1 SD). Vertical bands represent periods when the Fennoscandian ice sheet is covering the site, with purple shading indicating higher confidence (GSL < -93 m) and cyan shading indicating lower confidence (-93 m < GSL < -53 m) ice coverage. A higher degree of cyan shading indicates lower uncertainty. The grey dotted line represents present-day mean annual precipitation at the site (42 mm/month) taken from the CRU 0.5° gridded climatology for the period 1961–1990 (New et al. 1999).*

Table 2. Timings and durations of the projected periods of ice coverage at the Olkiluoto and Forsmark sites for the last glacial cycle (including modelling results of SKB (2010), and GSL reconstructed using the CGSLM and $\delta^{18}O$ data (Spratt and Lisiecki 2016)) and the natural, RCP2.6, RCP4.5, and RCP8.5 emissions scenarios. Lower confidence ice coverage corresponds to the cyan shaded bands on Figures 28 to 35, whilst higher confidence coverage corresponds to the purple shaded bands. For a single ice coverage event with consecutive periods of lower and higher confidence coverage, the timings and duration for the lower confidence coverage encompass the full event, with the period(s) of higher confidence coverage making up a part of this. For example, the first occurrence of ice coverage in the natural scenario (Figures 28a-35a) demonstrates lower confidence coverage starting at 82 kyr AP, followed by two periods of higher confidence coverage at 97–112 and 128–138 kyr AP with lower confidence ice coverage in between, followed by a period of lower confidence coverage from 139 until 141 kyr AP. However, this is reported as lower confidence coverage from 82 to 141 kyr AP (59 kyr), with a total of 25 years (15 + 10 kyr) projected to be higher confidence ice coverage. Grey shading indicates the occurrence of lower confidence ice coverage without progression to higher confidence coverage.

Scenario		Projected ice coverage at sites							
		Lower confidence				Higher confidence			
		From (kyr AP)	To (kyr AP)	Duration (kyr)	Total time (kyr)	From (kyr AP)	To (kyr AP)	Duration (kyr)	Total time (kyr)
LGC	SKB (2010)					-64	-55	9	
						-30	-11	19	
	CGSLM	-110	-104	6					
		-94	-13	81		-69	-55	14	
						-35	-16	19	
	$\delta^{18}O$	-112	-109	3					
		-71	-12	59		-39	-15	24	
Natural		82	141	59	59	97	112	15	15
						128	138	10	25
		151	158	7	66				
		169	229	60	126	177	181	4	29
						199	208	9	38
						212	226	14	52
		258	277	19	145	267	271	4	56
		283	321	38	183	293	318	25	81
		340	349	9	192				
		352	424	72	264	376	420	44	125
		529	588	59	323	552	562	10	135
						575	585	10	145
		604	609	5	328				
		622	682	60	388	645	653	8	153
						667	678	11	164
		713	767	54	442	721	723	2	166
						740	747	7	173
						754	764	10	183
		808	881	73	515	836	877	41	224
		886	899	12	528				
		904	966	62	590	912	918	6	230
						927	939	12	242
						950	962	12	254
RCP2.6		85	141	56	56	100	110	10	10

					130	137	7	17
	170	228	58	114	201	205	4	21
					214	226	12	33
	259	277	18	132	268	270	2	35
	284	321	37	169	294	318	24	59
	340	347	7	176				
	353	424	71	247	377	420	43	102
	508	520	12	259				
	524	588	64	323	533	538	5	107
					549	565	16	123
					573	585	12	135
	604	609	5	328				
	622	682	60	388	629	630	1	136
					645	653	8	144
					667	678	11	155
	713	767	54	442	721	723	2	157
					740	747	7	164
					754	764	10	174
	807	881	74	516	835	877	42	216
	886	899	13	529				
	904	966	62	591	912	918	6	222
					926	939	13	235
					950	962	12	247
RCP4.5	89	118	29	29				
	122	140	18	47	132	137	5	5
	172	228	56	103	216	225	9	14
	260	276	16	119				
	285	321	36	155	297	299	2	16
					306	318	12	28
	354	424	70	225	378	420	42	70
	508	520	12	237				
	525	588	63	300	534	537	3	73
					550	564	14	87
					573	585	12	99
	622	682	60	360	645	652	7	106
					667	678	11	117
	714	767	53	413	722	723	1	118
					741	747	6	124
					754	764	10	134
	807	881	74	487	835	877	42	176
	886	899	13	500				
	904	966	62	562	912	918	6	182
					926	939	13	195
					950	962	12	207
RCP8.5	217	226	9	9				
	265	273	8	17				
	290	319	29	46				
	360	422	62	108	414	418	4	4
	531	587	56	164	556	558	2	6
					577	584	7	13
	623	681	58	222	647	651	4	17
					668	678	10	27
	714	729	15	237				
	733	767	34	271	742	746	4	31
					755	764	9	40

809	824	15	286				
826	880	54	340	836	861	25	65
				865	877	12	77
886	899	13	353				
905	966	61	414	913	917	4	81
				927	939	12	93
				951	962	11	104
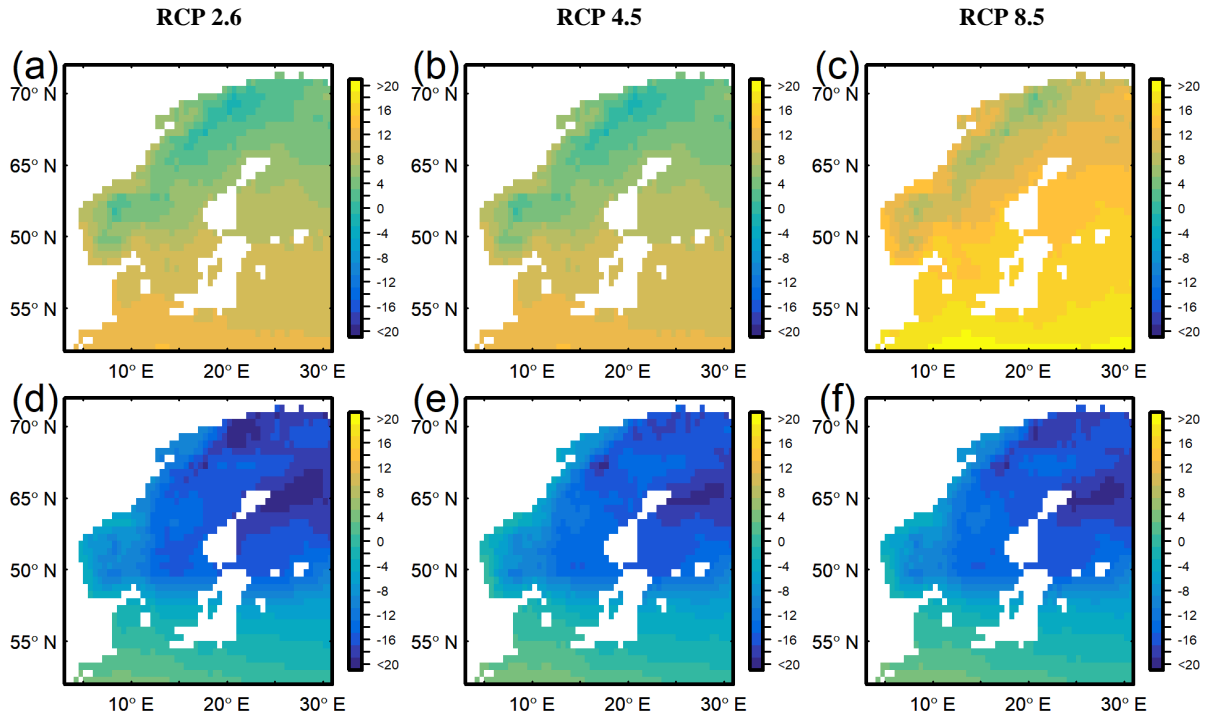
Figure 36. *Emulated mean annual SAT (°C) snapshots, downscaled using the bias-correction technique for the region of Scandinavia, for the RCP2.6, RCP4.5 and RCP8.5 emissions scenarios. Top panel: Warmest conditions (at: (a) 1 kyr AP, (b) 1 kyr AP, and (c) 2 kyr AP). Bottom panel: Coldest conditions immediately prior to development of the ice sheet at the sites during the next glaciation (at: (d) 99 kyr AP, (e) 131 kyr AP, and (f) 413 kyr AP).*
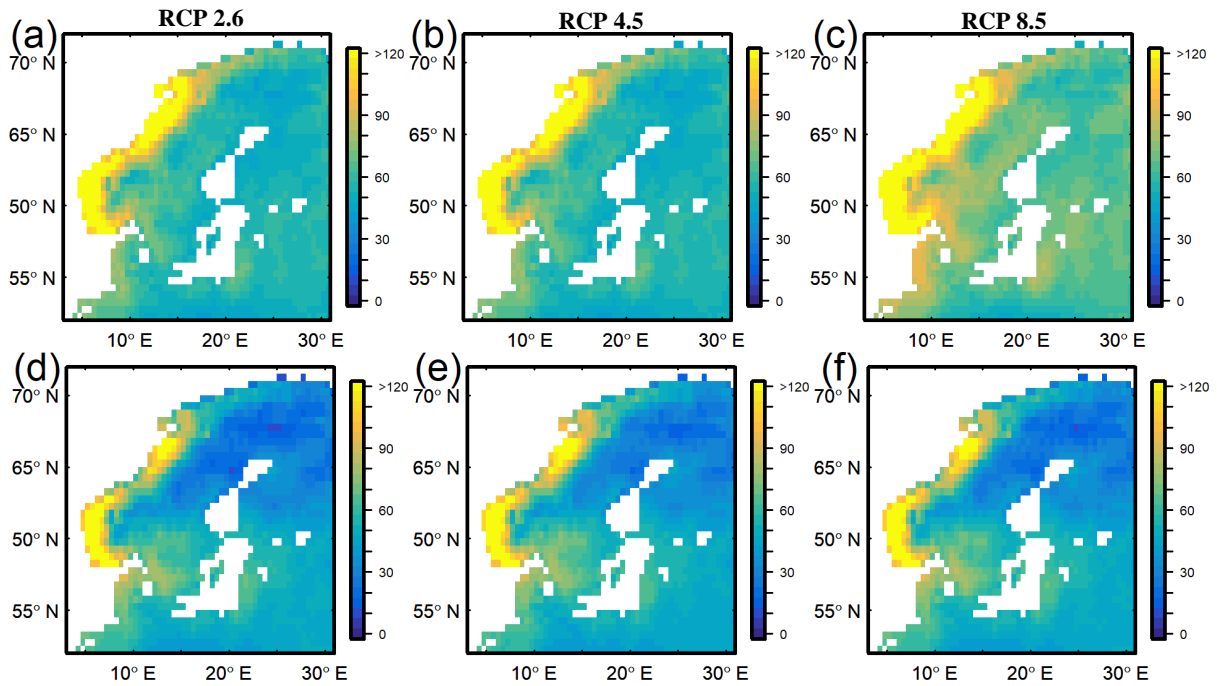
Figure 37. *Emulated mean annual precipitation (mm/month) snapshots, downscaled using the bias-correction technique for the region of Scandinavia, for the RCP2.6, RCP4.5 and RCP8.5 emissions scenarios. Top panel: Warmest conditions (at: (a) 1 kyr AP, (b) 1 kyr AP, and (c) 2 kyr AP). Bottom panel: Coldest conditions immediately prior to development of the ice sheet at the sites during the next glaciation (at: (d) 99 kyr AP, (e) 131 kyr AP, and (f) 413 kyr AP)*

If ice coverage is assumed not to occur at the sites (Figures 32 to 35), the SAT and precipitation curves follow the same trajectory as in Figures 28 to 31 during interglacial and mild glacial conditions. However, during full glacial conditions, the SAT results demonstrate less cooling due to the absence of ice at the grid boxes, and smaller extremes in precipitation. This is because the ice sheet margin no longer passes over the site, thus reducing the rain-shadow driven maxima, and increasing the minima that occur during periods of ice coverage at the site during full glacial conditions in Figures 30 and 31.

5 DISCUSSION AND UNCERTAINTIES

5.1 Future climate

The CGSLM applied here suggests that the next glacial inception following low to medium anthropogenic emissions (natural scenario, RCP2.6 or RCP4.5) may occur approximately 50 kyr in to the future. If high anthropogenic CO_2 emissions (RCP8.5) are assumed, the current interglacial may last until ~170 kyr AP. These timings are in good agreement with a number of previous studies that modelled the possible timing of the next glacial inception, many of which are summarised in the review by Brandefelt and Näslund (2014). For example, several studies have suggested that under pre-industrial atmospheric CO_2 concentrations, the next glacial inception may occur either imminently (Pimenoff et al. 2011) or in ~50 kyr (e.g. Berger and Loutre 2002, Berger et al. 2003, Cochelin et al. 2006, Ganopolski et al. 2016). For CO_2 scenarios with medium emissions, studies have suggested the end to the current interglacial period occurring in approximately 50 kyr (Berger et al. 2003), 130 kyr (Archer and Ganopolski 2005, Lord et al. 2015, Ganopolski et al. 2016), or 167 kyr AP (Texier et al. 2003). For high emissions of 5000 Pg C, Archer and Ganopolski (2005) concluded that the next glacial inception may be delayed for more than 500 kyr, in agreement with Lord et al. (2015), but in contrast to Texier et al. (2003), who estimated that the current interglacial would end in ~167 kyr under the same emissions forcing. The relatively large range in estimates for the onset of the next glaciation, even for similar emissions scenarios, is a result of different models and modelling techniques being used. Most of the studies used EMICs, which can be run over the multi-millennial timescales required to address this question. However, some the models may cover different regions (e.g. Northern Hemisphere only), may be forced with constant or varying atmospheric CO_2 concentrations or with anthropogenic CO_2 emissions, may or may not include different features, processes and feedbacks of the climate and Earth system (e.g. vegetation, carbon cycle), and may have different representations of different components of the Earth system (e.g. ocean, atmosphere). These differences mean that the models may respond slightly differently to insolation and CO_2 forcings, which can result in differences in their projections of future climate. The modelling approach applied in this report to project the glacial cycles (the CGSLM) was relatively simplistic compared to some of the studies discussed above. However, the modelling of long-term future global climate presented here was performed using an emulator calibrated on the results of a GCM, which is more complex than an EMIC in terms of the underlying physics and the features and processes of the Earth system that are represented.

A study by Brandefelt et al. (2013) estimated that for permafrost development to occur at Forsmark during the insolation minima at 17 and 54 kyr AP, atmospheric CO_2 concentrations of ~210 ppmv or less and ~250 ppmv or less would be required, respectively. In light of the long atmospheric lifetime of CO_2 emissions that has been discussed, low concentrations such as these are unlikely in the next few tens of thousands of years; however, they cannot be entirely excluded over this time period. It should be noted, however, that the initiation of the next glaciation does not mean that ice coverage at the sites in question is imminent. In fact, based on the GSL threshold method applied here and only taking into account periods of higher confidence ice coverage, the results suggest that the Fennoscandian ice sheet will not extend as far as the Forsmark and

Olkiluoto sites until ~100 kyr AP for RCP2.6, ~130 kyr AP for RCP4.5, and ~410 kyr AP for RCP8.5.

The results of the emulator suggest that future climate at the Olkiluoto and Forsmark sites will change in response to both orbital and anthropogenic CO_2 forcing, and the glacial-interglacial cycles. Under the emissions scenarios explored here, the most extreme changes in the climate variables considered generally occur within the first 50 kyr AP, immediately following the emissions period when atmospheric CO_2 concentrations are relatively high. Following this, climate conditions tend to gradually return back towards pre-industrial conditions, with orbitally-forced fluctuations and variations in global ice volume becoming more dominant. For the emissions scenarios considered here, mean annual SAT is projected to increase by a maximum of 10.0 ± 0.6 °C at the Olkiluoto site and 9.3 ± 0.6 °C at the Forsmark site, whilst precipitation at the sites increases by up to 20.0 ± 0.5 mm/month in response to radiative forcing from anthropogenic emissions.

A previous study by Kjellström et al. (2009) used the Rossby Centre regional climate model, RCA3, to simulate climate over the Fennoscandian region for a number of different climate states. One of these was a warm climate state, representing the climate several thousand years into the future when greenhouse gas concentrations are still above pre-industrial values at 750 ppmv. This simulation was compared to a simulation of the recent past (roughly representing the time period 1961–2000) and suggested a warming of 4.0 °C at Olkiluoto and 3.6 °C at Forsmark, accompanied by increases in mean annual precipitation of 16.0 and 11.5 mm/month, respectively. For reference, the recent past simulation was also performed using the Community Climate System Model version 3 (CCSM3) GCM, along with a pre-industrial simulation, and resulted in an annual global mean temperature that was 1.3 °C warmer than the pre-industrial simulation.

Other modelling has suggested a warming of ~7 − 11 °C averaged over the period 2181–2200 AD for central northern Europe under RCP8.5 (Collins et al. 2013), largely in line with the results presented here. Winkelmann et al. (2015) projected a maximum warming of around 8 °C for a 5,000 Pg C emissions scenario, although this was for global mean temperature rather than a single grid box temperature, and was modelled using the EMIC *c*GENIE. In reality, the degree of human-induced climate change will be dependent on the total emissions that are released to the atmosphere, with lower emissions expected to result in lower levels of warming, as illustrated in Figure 21. However, the amount of CO_2 that will be emitted in the future is not known; thus, a relatively high emissions scenario was selected to represent a bounding scenario. Even relatively modest estimates of total emissions have been found to result in relatively large changes in climate compared with those driven by orbital changes during unperturbed interglacial periods.

In the results presented here, SAT at the LGM (18-21 kyr BP) at Olkiluoto is projected to decrease by up to 24.1 ± 0.6 °C compared to the pre-industrial simulation, whilst Forsmark is projected to cool by up to 25.9 ± 0.5 °C. A large proportion of this cooling occurs as a result of the significantly increased altitude of the modelled land surface due to the presence of the ice sheet (temperatures are colder at higher altitudes). In addition, precipitation decreases by up to 12.3 ± 0.5 mm/month at Olkiluoto, and up to 16.6 ± 0.6 mm/month at Forsmark. This can be compared to Kjellström et al. (2009), who included a glacial climate state in their modelling of Fennoscandian climate using RCA3, which

represented a period during the LGM (21 kyr BP). The model projected a cooling of 20.8 °C at the Olkiluoto site and 25.5 °C at the Forsmark site when compared with the recent past simulation (described earlier in this section). Mean annual precipitation at Olkiluoto was estimated to decrease by 8.2 mm/month (compared with the recent past) at Forsmark, but no significant change was projected at the Olkiluoto site. A similar magnitude of cooling was simulated over Fennoscandia by the CLIMBER-2-SICOPOLIS model for a simulation of the last glacial cycle (Pimenoff et al. 2011). A number of other studies have estimated cooling in mean annual temperature over northern Europe of ~10 – 32 °C during the LGM (e.g. Otto-Bliesner et al. 2006, Braconnot et al. 2007, Singarayer and Valdes 2010). There are a number of causes of differences in the predictions of climate conditions at the LGM, including different models and methods of reconstruction (e.g. GCMs, EMICs, proxy data) being used, different climate forcing records (e.g. GSL and CO_2 reconstructed using models or palaeo proxy data), and different model boundary conditions (e.g. orography). Issues such as these are the motivation for many large intermodel comparison projects, such as the Coupled Model Intercomparison Project (CMIP, www.wcrp-climate.org/wgcm-cmip/wgcm-cmip6) and the Paleoclimate Model Intercomparison Project (PMIP, https://pmip4.lsce.ipsl.fr). These projects use a range of GCMs to run sets of simulations with the same forcing and boundary conditions, with the aims of assessing the impact of model structural differences on climate projections and producing multi-model mean results, which are often taken to be the "best estimate" climate projections.

5.2 Implications of climate changes

Whether as a result of orbital or CO_2 forcing, fluctuations in climate could have implications for the safety assessments of the geological repositories that have been proposed to be sited at Olkiluoto and Forsmark. One key issue for both sites relates to the timing of the next glacial inception (see e.g. SKB 2010). During glacial episodes, the advance and retreat of ice sheets can lead to changes on groundwater flow and chemistry, changes in stresses in the Earth's crust, surface erosion (Clayton 1994, SKB 2010), and isostatic effects (SKB 2010, Whitehouse 2009). Permafrost may develop during periglacial conditions, reaching depths of tens or hundreds of metres (French 2007, Hartikainen et al. 2010). Hence, a significantly extended interglacial or a delayed glaciation with an extended prior period of periglacial conditions can have important implications which may be either detrimental or advantageous to safety, for the long-term performance of repositories located in previously glaciated regions (see e.g. SKB 2011).

Changes in GSL, particularly increasing GSL associated with anthropogenic warming and continental ice sheet retreat, may also have implications for these sites given their coastal locations, although ongoing glacial isostatic adjustment would act to mitigate the impacts of some of this sea level rise (e.g. SKB 2010).

5.3 Alternative downscaling methods

The results in Section 4.2.2 were produced using bias-correction downscaling, as described in Section 3.3.1. Here, we instead present results from an alternative method – physical-statistical downscaling (described in Section 3.3.2). Physical-statistical downscaling works by identifying statistical relationships between high-resolution data describing physical characteristics of the region (e.g. orography), high-resolution observed climate data (e.g. SAT) and low resolution climate model data (e.g. SAT, orography). The statistical model is then applied to the emulated projections of future climate, allowing the climatic impacts of physical conditions at a finer scale than the GCM resolution to be represented in the projected data. To account for the model error, the downscaled results are bias-corrected based on the anomaly between the pre-industrial climate results predicting using the physical-statistical model and the CRU climate data. The climate projections for the sites downscaled using this method are illustrated in Figures 38-41 (dashed lines), along with the results downscaled using bias-correction (bold solid lines) which were also presented in Figures 28-31.

Two other downscaling techniques were also considered, which aim to address the increased uncertainty in the bias-correction and physical-statistical techniques during periods when ice is present at the sites. For these results, the bias-correction and physical-statistical downscaling techniques were applied when the sites were ice-free (i.e. interglacial and early glacial conditions). However, during conditions of ice coverage at the sites (i.e. full glacial) the raw emulator climate output (interpolated to 0.5° resolution of the CRU dataset) was used, rather than a downscaled version. Only the results of the bias-correction downscaling applied only when there is no ice at the sites, assigned the suffix 'no ice' (dotted lines), are presented in Figures 38-41 because the results of the 'no ice' physical-statistical downscaling were essentially indistinguishable from the other curves.

Of particular interest in Figures 38-41 is the comparison of the bias-correction and physical statistical downscaling techniques, which each have different strengths and weaknesses that are discussed below. For SAT, the projections at the two sites downscaled using these two techniques are very similar and only differ occasionally, particularly during mild glacial conditions (Figures 38 and 39). At these times, the SATs following physical-statistical downscaling are slightly warmer (by up to ~1 °C) due to differences between the low-resolution GCM orography and the high-resolution orography.

The difference between the two downscaling techniques is a little more variable for precipitation. At both sites (Figures 40 and 41), precipitation is fairly similar across the two techniques during interglacial conditions, such as between ~430 and 530 kyr AP. However, at Olkiluoto just before or after the approach or coverage of the ice sheet at the site (cyan and purple bands), the bias-corrected data shows higher precipitation values than the physical-statistical data. The higher values at these times originate in the emulated precipitation data, and are amplified by the bias correction downscaling but not by the physical-statistical downscaling. This trend is also evident at the Forsmark site, although to a lesser degree. During full glacial conditions, the physical-statistical downscaling results in significantly lower precipitation rates at both sites, by up to ~12–

15 mm/month at Olkiluoto and ~5–6 mm/month at Forsmark. This may be related to the high-resolution orography data of Peltier (2004) used in the statistical model exhibiting higher orography for the ice sheet in this region than the HadCM3 orography used in the emulator.
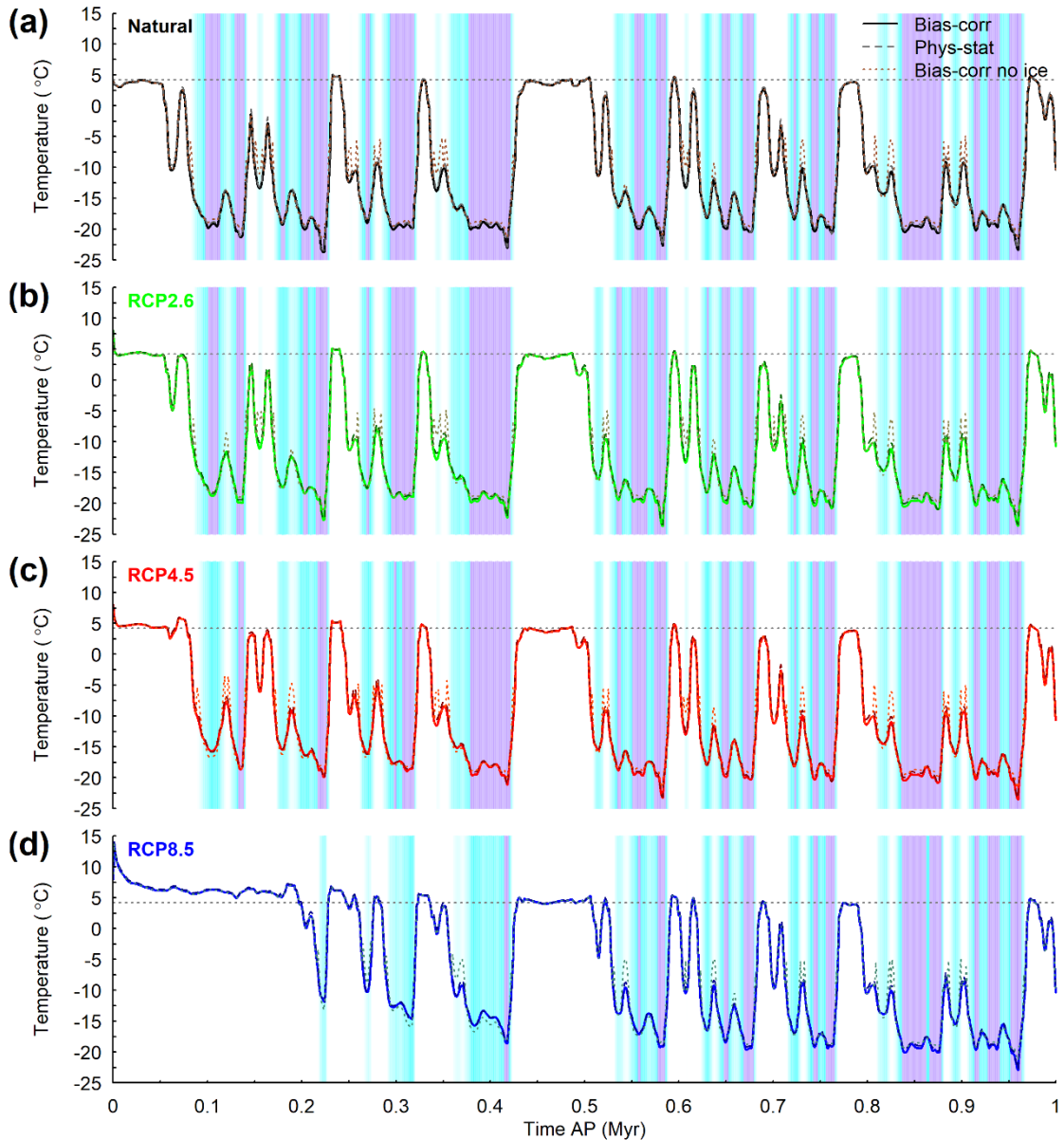
Figure 38. *Time series of emulated downscaled mean annual SAT (°C) for the next 1 Myr at the Olkiluoto site, for the natural ((a)), RCP2.6 ((b)), RCP4.5 ((c)), and RCP8.5 ((d)) emissions scenarios, downscaled using a number of alternative techniques. These include the bias-correction downscaling presented in Figure 28 (solid lines; 'Bias-corr'), physical-statistical downscaling (dashed lines; 'Phys-stat'), and the bias-correction technique applied only when ice is not covering the sites (dotted lines; 'Bias-corr no ice'). SAT is modelled every 1 kyr. Vertical bands represent periods when the Fennoscandian ice sheet is covering the site, with purple shading indicating higher confidence (GSL < -93 m) and cyan shading indicating lower confidence (-93 m < GSL < -53 m) ice coverage. A higher degree of cyan shading indicates lower uncertainty. The grey dotted line represents present-day mean annual SAT at the site (4.2 °C) taken from the CRU 0.5° gridded climatology for the period 1961–1990 (New et al. 1999).*

Figure 39. *Time series of emulated downscaled mean annual SAT (°C) for the next 1 Myr at the Forsmark site, for the natural ((a)), RCP2.6 ((b)), RCP4.5 ((c)), and RCP8.5 ((d)) emissions scenarios, downscaled using a number of alternative techniques. These include the bias-correction downscaling presented in Figure 29 (solid lines; 'Bias-corr'), physical-statistical downscaling (dashed lines; 'Phys-stat'), and the bias-correction technique applied only when ice is not covering the sites (dotted lines; 'Bias-corr no ice'). SAT is modelled every 1 kyr. Vertical bands represent periods when the Fennoscandian ice sheet is covering the site, with purple shading indicating higher confidence (GSL < -93 m) and cyan shading indicating lower confidence (-93 m < GSL < -53 m) ice coverage. A higher degree of cyan shading indicates lower uncertainty. The grey dotted line represents present-day mean annual SAT at the site (4.2 °C) taken from the CRU 0.5° gridded climatology for the period 1961–1990 (New et al. 1999).*

Downscaling the data only during ice-free conditions at the sites results in slightly higher SATs during mild glacial conditions at Olkiluoto (by up to 1 °C) and slightly lower SATs during full glacial conditions at Forsmark (by up to -3 °C). During glacial conditions, precipitation rates at Olkiluoto are generally intermediate between the bias-correction (higher precipitation) and physical-statistical downscaling results (lower precipitation). Conversely, at Forsmark during mild glacial conditions precipitation rates at Forsmark are higher than the standard bias-corrected results.
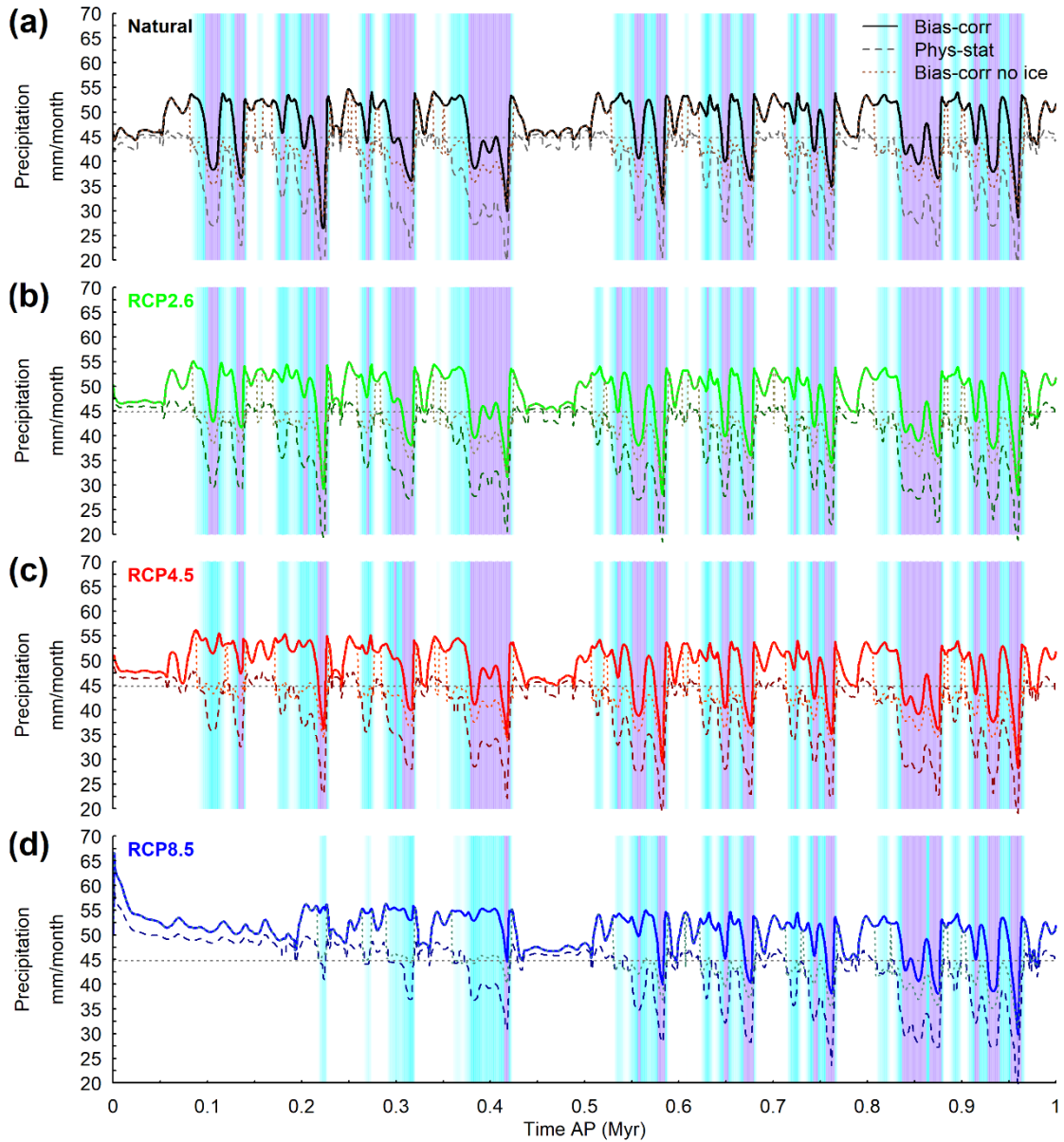
Figure 40. *Time series of emulated downscaled mean annual precipitation (mm/month) for the next 1 Myr at the Olkiluoto site, for the natural ((a)), RCP2.6 ((b)), RCP4.5 ((c)), and RCP8.5 ((d)) emissions scenarios, downscaled using a number of alternative techniques. These include the bias-correction downscaling presented in Figure 30 (solid lines; 'Bias-corr'), physical-statistical downscaling (dashed lines; 'Phys-stat'), and the bias-correction technique applied only when ice is not covering the sites (dotted lines; 'Bias-corr no ice'). SAT is modelled every 1 kyr. Error bands represent the emulated grid box posterior variance (1 SD). Vertical bands represent periods when the Fennoscandian ice sheet is covering the site, with purple shading indicating higher confidence (GSL < -93 m) and cyan shading indicating lower confidence (-93 m < GSL < -53 m) ice coverage. A higher degree of cyan shading indicates lower uncertainty. The grey dotted line represents present-day mean annual precipitation at the site (42 mm/month) taken from the CRU 0.5° gridded climatology for the period 1961–1990 (New et al. 1999).*

Figure 41. *Time series of emulated downscaled mean annual precipitation (mm/month) for the next 1 Myr at the Forsmark site, for the natural ((a)), RCP2.6 ((b)), RCP4.5 ((c)), and RCP8.5 ((d)) emissions scenarios, downscaled using a number of alternative techniques. These include the bias-correction downscaling presented in Figure 31 (solid lines; 'Bias-corr'), physical-statistical downscaling (dashed lines; 'Phys-stat'), and the bias-correction technique applied only when ice is not covering the sites (dotted lines; 'Bias-corr no ice'). SAT is modelled every 1 kyr. Error bands represent the emulated grid box posterior variance (1 SD). Vertical bands represent periods when the Fennoscandian ice sheet is covering the site, with purple shading indicating higher confidence (GSL < -93 m) and cyan shading indicating lower confidence (-93 m < GSL < -53 m) ice coverage. A higher degree of cyan shading indicates lower uncertainty. The grey dotted line represents present-day mean annual precipitation at the site (42 mm/month) taken from the CRU 0.5° gridded climatology for the period 1961–1990 (New et al. 1999).*

These downscaled results demonstrate the uncertainty in the emulated projections of future climate when they are downscaled to 0.5° resolution. Each of the techniques have strengths and weaknesses, which may vary between different climate variables and different climate states. For example, all techniques works well during interglacial conditions that are similar to present day, particularly in the case of SAT, since the model bias is calculated compared to observations of recent modern-day (CRU climatology data). This bias is assumed to be independent of climate state, meaning that the same bias is applied during both interglacial and glacial conditions. In reality this may not be the case, but with no high-resolution observations of a glacial climate this is very difficult to confirm.

The climate data downscaled using the physical-statistical technique, prior to the subsequent bias-correction, appears to be less similar to the CRU data site observations during interglacial conditions, in particular precipitation. This is because, as mentioned previously, physical-statistical downscaling generally works better for SAT than precipitation because the interaction of physical processes that impact precipitation are more complicated, making it harder for the statistical model to identify statistical relationships between the climate and physical data. Therefore, it may be that in some regions precipitation is over- or underestimated, such as over south west Norway where significantly higher precipitation is seen in the observational data than in the downscaled emulator results. The regression models also include a relatively small number of physical variables, whilst in reality temperature and precipitation are likely to be affected by a wider range of variables and conditions. Additionally, the physical-statistical model is limited by the underlying emulator results that are fed into it, which are themselves limited by the GCM, and GCMs generally exhibit less skill in reproducing precipitation than SAT. These errors are corrected for during the bias-correction stage. However, the physical-statistical downscaling technique is also limited during glacial conditions, as the statistical relationships identified under an interglacial climate, as well as the model bias, are assumed to remain unchanged.

These limitations during glacial climates were the drivers for the inclusion of climate projections downscaled only during ice-free conditions; in such situations the two downscaling methods have been shown to work relatively well, but during glacial conditions the uncertainty may be higher, so an argument can be made for using the raw emulator data during these periods, which is based on the underlying GCM. However, this may therefore mean that the climate data during these periods do not account for relatively fine spatial scale conditions in the region (e.g. orography).

A number of alternative downscaling techniques have been presented and compared to the downscaled climate projections described in Section 4.2.2. Although there are some variations between the projections, particularly precipitation, they show generally similar trends to each other, and each method of downscaling has different strengths and weaknesses which have been discussed.

5.4 Methodological uncertainties and limitations

There are a number of limitations associated with the methodology outlined above, particularly relating to the assumptions that it is based on and its application to different periods of time. These include:

- The carbon cycle response function is a relatively simple and global mean function linking weathering rates and climate. It does not account for potential additional long-term negative feedbacks and influences involving marine organic carbon burial, positive feedbacks associated with melting of permafrost and release of methane from methane clathrates, changes in volcanic outgassing, or shorter timescale interactions with the terrestrial biosphere. The impacts that changes in climate have on these processes and feedbacks are still not fully understood, and there is also significant uncertainty about changes in the relationship between CO_2, climate and global weathering (e.g. Munhoven 2002, Uchikawa and Zeebe 2008, Meissner et al. 2012). The response function also assumes that, in the absence of anthropogenic CO_2 emissions and orbital forcing (i.e. a "natural scenario"), atmospheric CO_2 will remain in constant.

- The relatively simple linear regression used to update atmospheric CO_2 concentration during glacial periods allows the impact of glacial conditions on atmospheric CO_2 to be represented, but does not account for any non-linearity in the response of CO_2. There is also some uncertainty associated with the relationship between glacial-interglacial cycles and CO_2 and the feedbacks that link them.

- The CGSLM that was used to calculate future GSL is relatively simplistic, requiring a relatively small number of forcings and tuneable parameters. However, similar models are commonly used in research due to the very long time scales involved when considering glacial-interglacial cycles (e.g. Archer and Ganopolski 2005, Paillard 1998, Ganopolski et al. 2016, Tzedakis et al. 2017), and the model has been shown to be able to reproduce reconstructed past global temperature anomalies and GSL data reasonably well (Figure 5). However, this method of validation assumes that the fundamental climate regime of the next 1 Myr will be the same as that of the last 1 Myr, with glacial conditions occurring approximately every 100 kyr. Prior to 1 Myr BP, however, glacials occurred approximately every 40 kyr, and because there is still some uncertainty associated with the drivers of this change in pacing, it cannot be ruled out that the glacial regime may change again in the future. Nevertheless, based on current understanding of the glacial cycles and palaeo-validation results, exploration of the sensitivity of the model to the values of the tuneable parameters has suggested that, when parameters are varied independently, the model is relatively robust, with a range of values for the parameters generally resulting in relatively small changes in the model results. A more thorough sensitivity analysis using LHC sampling (Section 3.1.3) found that, for model configurations that reproduced the palaeo temperature record well, several different temperature pathways for the future were projected, particularly during periods with relatively small variations

in insolation. This is partly a result of the relative simplicity of the conceptual model, which relies on insolation and time thresholds to control transitions between different climate states. Given that the future evolution of temperature is not known, the model was tuned to the palaeo data and model configuration that best reproduced the data was selected as the final model. It would also not be feasible to run such a long simulation using a GCM model containing a coupled ice sheet model due to the associated computational expense, although EMICs may be able to simulate long-term ice sheet evolution (e.g. Ganopolski and Brovkin 2017).

- The projections of future atmospheric CO_2 and GSL, and hence the climate projections, are based on the assumption that beyond approximately 2500 AD, humans will make no other significant changes to the climate. This may occur through emissions of CO_2 from the burning of fossil fuels or other processes such as land-use change, or through emissions of other gases that act as radiative forcing agents, such as methane or aerosols. The uncertainty associated with future human activities and the resulting impacts on radiative forcing is significant, thus a range of IPCC emissions scenarios have been included to account for the different possible pathways that society might take.

- The carbon cycle in the emulator is not coupled to the climate, since the atmospheric CO_2 concentration is prescribed. The methodology thus assumes that there will be no unexpected non-linearities in the carbon cycle, and that changes in climate that are different from those in *c*GENIE do not feed back to the carbon cycle. This may be of particular importance when simulating future climates, when the natural carbon cycle is expected to be significantly perturbed due to ongoing anthropogenic emissions of CO_2, in a way that may not be fully represented in *c*GENIE. There is also uncertainty surrounding the dynamics of the carbon cycle over long periods of time, such as the role of the silicate weathering mechanism, although the observation that different carbon cycle models generally produce fairly similar results increases our confidence (Archer et al. 2009).

- Whilst changes in the ice sheets in response to atmospheric CO_2 can be represented by the emulator, such as the likely future melting of the GrIS and WAIS in response to anthropogenic CO_2 emissions, the impact of these changes on the Earth and climate system cannot be captured. For example, various studies have modelled the response of the ice sheets to future climate warming, finding that the ice sheets may experience significantly increased melt. In fact, for scenarios with high CO_2 emissions (>~5000 Pg C), it has been suggested that the GrIS and AIS may be almost entirely melted within the next few thousand years (e.g. Huybrechts et al. 2011, Winkelmann et al. 2015, DeConto and Pollard 2016), which would cause significant changes in deep ocean circulation and ocean stratification (Golledge et al. 2019). These ocean changes cannot be captured by the current version of the methodology and, whilst their impacts on global and regional climate are uncertain, they are expected to be long-term. The melting of the ice sheets would also cause significant increases in global sea level, of approximately 70 m if both the GrIS and AIS melted (IPCC 2013) or up to ~50 m for partial melt of the EAIS (Clark et al. 2016), which would strongly affect the

global land-sea mask and regional climates, and which cannot be represented using the current methodology.

- At present the emulator assumes that future glaciations will follow the same trajectory of ice sheet expansion and retreat as was observed during the last stadial of the Weichselian, since the ensemble of GCM simulations that simulate glacial conditions are based on the last glacial cycle (Singarayer and Valdes 2010). However, it may be that future glaciations do not demonstrate the same spatial patterns of ice build-up and melt, perhaps due to differences in the orbital parameters or atmospheric CO_2. This may mean that for a certain GSL value, there may be multiple possible projections of Fennoscandian climate, resulting from changes in the ice sheet configuration over time, land surface albedo, and/or atmospheric circulation patterns. In fact, this is known to have occurred in the past – the distribution of land ice during the penultimate glacial maximum was different to that during the LGM, with geological evidence indicating a larger Fennoscandian ice sheet (Svendsen et al. 2004) and climate modelling suggesting a smaller Laurentide ice sheet (Colleoni et al. 2016). However, at present, there only exist robust observationally-constrained global ice sheet reconstructions for the last glacial cycle. As such, we believe that at this stage our methodology is appropriate. However, if ice sheet extent data for more than one glacial cycle were developed, and/or ice sheet modelling advanced to such a point that simulations alone could produce robust ice sheets configurations, then multiple versions of glacial cycles could be included, or else the continental ice sheets could be simulated separately. Alternatively, sensitivity studies could be carried out with an ice sheet model to try to investigate how the ice sheet extents varied during past glaciations. However, this approach would also involve inherent uncertainties, and is beyond the scope of the present study.

- Similarly, the Singarayer and Valdes (2010) climate simulations use the ICE-5G ice sheet reconstruction of Peltier (2004). These reconstructions were selected because they are based on palaeo data (global sea level and/or ice-sheet extent) and include the range of associated data that was required for this work. In addition, for glaciations prior to the last glacial cycle, there is very little or no palaeo data available that enables the 3-D reconstructions which are required here. However, a number of other reconstructions of the ice sheets also exist and demonstrate some differences to the ICE-5G reconstructions (see e.g. Schmidt et al. 2014), which could result in changes to the simulated climate. For example, some studies have suggested a lower maximum elevation for the Laurentide ice sheet during glacial conditions (e.g. Kleman et al. 2013, Abe-Ouchi et al. 2015). Modelling studies have suggested that the topography of the ice sheet can have a significant impact on mean sea level pressure, which affects the location of the wind-driven gyre circulation in the subpolar North Atlantic, and on the strength of the Atlantic Meridional Overturning Circulation, resulting in warming in the North Atlantic (Pausata et al. 2011, Colleoni et al. 2016). Storm tracks in the North Atlantic have also been shown to be affected, with associated impacts on precipitation and snowfall in northern Europe (e.g. Kageyama and Valdes 2000, Lofverstrom et al. 2014, Colleoni et al. 2016). As before, future work could investigate the sensitivity of future climate to the size and shape of the ice sheets

using ice sheet modelling, for example by incorporating additional GCM simulations with different ice sheet configurations into the emulator.

- Since the emulator simulates climate via a series of snapshots rather than a truly transient simulation, it is not able to capture deviations from a stationary response. As a consequence, the methodology becomes inappropriate if such transient changes in the deep ocean are found to be important for controlling surface climate evolution.

- The emulator is also limited by the limitations of the underlying GCM, and is only able to represent the processes and feedbacks included in it. Processes such as changes in atmospheric dust, for example, may have an impact on long-term climate but are associated with significant uncertainty and are not accounted for in the GCM. Vegetation in the underlying GCM simulations is able to change in response to changes in climate (including biophysical feedbacks but not biochemical feedbacks) but, as with CO_2, the nature of the emulator means that this is not coupled to climate, so any variations resulting from climate-CO_2 feedbacks are not represented.

- Two techniques for spatial downscaling, being bias-correction and physical-statistical downscaling, were presented and compared in Sections 4.2.2 and 5.3, along with a second variation of each method in which the downscaling was only carried out when an ice sheet was not present at the two sites. Each of the techniques has strengths and weaknesses, and makes a number of assumptions which could affect the downscaled results, and these are discussed in detail in Section 5.3. For example, it is assumed that the relationships identified by both techniques which are based on modern-day conditions will be the same in the future, for both global warming and cold glacial conditions, which may not necessarily be the case. The regression models for the physical-statistical downscaling also include a relatively small number of physical variables, whilst in reality temperature and precipitation are likely to be affected by a wider range of variables and conditions. Finally, both methods are limited by the underlying emulator results that are fed into them, which are themselves limited by the GCM.

- The emulator presented in this study is only suitable for modelling transient climate changes on timescales of several millennia or longer, as a number of shorter-term processes in the climate and carbon cycle are not represented. These include internal variability in the climate system, such as interannual variability, North Atlantic Oscillation (NAO), and El Niño – Southern Oscillation (ENSO), as well as radiative forcing occurring on shorter timescales (e.g. volcanic activity), and terrestrial carbon cycle processes. On these timescales, transient simulations run using complex models such as GCMs or EMICS are most appropriate.

- The modelling results presented consider changes in mean annual climate, and seasonal variations are not presented. Changes in seasonal climate may be of importance to processes such as permafrost development and interannual persistence of snow cover. Seasonality was beyond the scope of this study, but could be addressed in a subsequent study by running the emulator with seasonal GCM simulations.

- The carbon cycle response function, GSL projections, and climate emulator are all based on the results of single models (cGENIE, the CGSLM, and HadCM3, respectively). Other models may produce different results, due to variations in model structure and the parameterisations used. A discussion of how future projections of atmospheric CO_2 concentration following CO_2 emissions produced by cGENIE compare to similar results from other models is provided by Lord et al. (2016). Similarly, Lord et al. (2017) compare the results of a previous version of the emulator, particularly relating to the possible timing of the next glacial inception, to projections produced using other models. The comparison of our palaeoclimate results to palaeo proxy data in Section 3.2.3 suggests that the models used work fairly well during the time periods considered. However, further research could aim to compare the results presented here to projections produced based on other models.

In summary, the emulator is a useful tool for projecting changes in long-term climate, as long as the above assumptions and limitations are carefully considered to ensure that the methodology is being applied in the manner and under the conditions for which it was designed.

6 SUMMARY AND CONCLUSIONS

In this study, a combination of modelling techniques have been used to simulate the possible evolution of future climate over the next 1 Myr for a range of anthropogenic CO_2 emissions scenarios. These models include a carbon cycle impulse response function used to project atmospheric CO_2 concentration in response to anthropogenic CO_2 emissions, a CGSLM which estimated future changes in GSL forced by orbital and atmospheric CO_2 variations, and a statistical climate emulator used to project the future evolution of a number of climate variables forced by atmospheric CO_2 concentration, orbital variations and global ice sheet volume changes. The results of the emulator were then downscaled using bias-correction and a physical-statistical technique.

Future climate has been shown to vary in response to the CO_2 and orbital forcings and glacial-interglacial cycles, exhibiting a period of warming (accompanied by associated climate changes) for up to 50 kyr, due to elevated atmospheric CO_2 concentrations following emissions. This is followed by an increased dominance of orbital forcing on climate, and fluctuations between interglacial and glacial states. However, the results suggest that the timing of the next glacial inception, which is a key climate issue in safety assessments performed for the Olkiluoto and Forsmark sites, may be strongly affected by anthropogenic CO_2 emissions, with low to medium emissions resulting in the next glaciation occurring in ~50 kyr, and relatively high emissions extending the current interglacial for approximately 170 kyr. If the first occurrence of ice sheet coverage at the sites is considered, these timescales are even longer, being ~100-130 kyr AP and ~410 kyr AP, respectively.

Bearing in mind the limitations discussed in the previous section, the methodology described in this report is a useful and powerful tool for simulating long-term future climatic changes. The data presented here can be utilized in safety assessments for nuclear waste repositories. Depending on the application, the raw climate data produced by the emulator may not be sufficient, meaning that downscaling to regional or local scale may be required, and the temporal resolution of the data may need to be increased. A bias-correction downscaling technique has been applied here (and compared to a physical-statistical downscaling technique), increasing the spatial resolution of the climate data, but temporal downscaling is not addressed in this report. Suitably spatially and temporally downscaled data can be used to drive landscape-development or permafrost models which, due to the nature of the process of landscape development and the range of properties that affect it, need to be site-specific. Information about the future evolution of the site can then be used in assessments of long-term safety of the repository and help ensure that the level of exposure of humans and the environment to potential radioactive materials released from the repository are compliant with regulatory requirements.

Whilst future projections of SAT and precipitation have been presented in this report, a number of other climate variables have also been emulated to cover the next 1 Myr period, including soil temperature and moisture, snow depth, wind speed, and total leaf area index (as a proxy for vegetation). These data, as well as the SAT and precipitation data, have been provided separately. As previously stated, the SAT projections for glacial conditions that are presented in this report could be considered as worst-case, based on a comparison of the climate model and palaeo proxy climate data, i.e. if the palaeoclimate that was

reconstructed using proxy data is correct then the cooling and associated impacts (e.g. permafrost) may not be quite as severe as projected in this report.

REFERENCES

ABE-OUCHI, A., SAITO, F., KAGEYAMA, M., BRACONNOT, P., HARRISON, S. P., LAMBECK, K., OTTO-BLIESNER, B. L., PELTIER, W. R., TARASOV, L., PETERSCHMITT, J. Y. & TAKAHASHI, K. 2015. Ice-sheet configuration in the CMIP5/PMIP3 Last Glacial Maximum experiments. *Geoscientific Model Development,* 8**,** 3621-3637.

ABE-OUCHI, A., SAITO, F., KAWAMURA, K., RAYMO, M. E., OKUNO, J., TAKAHASHI, K. & BLATTER, H. 2013. Insolation-driven 100,000-year glacial cycles and hysteresis of ice-sheet volume. *Nature,* 500**,** 190-+.

ANNAN, J. D. & HARGREAVES, J. C. 2013. A new global reconstruction of temperature changes at the Last Glacial Maximum. *Climate of the Past,* 9**,** 367-376.
ARCHER, D. 2005. Fate of fossil fuel CO_2 in geologic time. *Journal of Geophysical Research-Oceans,* 110.

ARCHER, D., EBY, M., BROVKIN, V., RIDGWELL, A., CAO, L., MIKOLAJEWICZ, U., CALDEIRA, K., MATSUMOTO, K., MUNHOVEN, G., MONTENEGRO, A. & TOKOS, K. 2009. Atmospheric lifetime of fossil fuel carbon dioxide. *Annual Review of Earth and Planetary Sciences,* 37**,** 117-134.

ARCHER, D. & GANOPOLSKI, A. 2005. A movable trigger: Fossil fuel CO_2 and the onset of the next glaciation. *Geochemistry Geophysics Geosystems,* 6.

ARCHER, D., KHESHGI, H. & MAIER-REIMER, E. 1997. Multiple timescales for neutralization of fossil fuel CO_2. *Geophysical Research Letters,* 24**,** 405-408.

BEREITER, B., EGGLESTON, S., SCHMITT, J., NEHRBASS-AHLES, C., STOCKER, T. F., FISCHER, H., KIPFSTUHL, S. & CHAPPELLAZ, J. 2015. Revision of the EPICA Dome C CO_2 record from 800 to 600 kyr before present. *Geophysical Research Letters,* 42**,** 542-549.

BERGER, A. 1978. Long-term variations of daily insolation and Quaternary climatic changes. *Journal of the Atmospheric Sciences,* 35**,** 2362-2367.

BERGER, A. & LOUTRE, M. F. 1991. Insolation Values for the Climate of the Last 10000000 Years. *Quaternary Science Reviews,* 10**,** 297-317.

BERGER, A. & LOUTRE, M. F. 2002. An exceptionally long interglacial ahead? *Science,* 297**,** 1287-1288.

BERGER, A., LOUTRE, M. F. & CRUCIFIX, M. 2003. The Earth's climate in the next hundred thousand years (100 kyr). *Surveys in Geophysics,* 24**,** 117-138.

BGR 2012. Energy Study 2012. Reserves, Resources and Availability of Energy Resources. Federal Institute for Geosciences and Natural Resources (BGR).

BIOCLIM 2001. Deliverable D3: Global climatic features over the next million years and recommendation for specific situations to be considered. Agence Nationale pour la Gestion des Dechets Radioactifs (ANDRA).

BIOCLIM 2003a. Deliverable D6a: Regional climatic characteristics for the European sites at specific times: The dynamical downscaling. Agence Nationale pour la Gestion des Dechets Radioactifs (ANDRA).

BIOCLIM 2003b. Deliverable D4/5: Global climatic characteristics, including vegetation and seasonal cycles over Europe, for snapshots over the next 200,000 years. Agence Nationale pour la Gestion des Dechets Radioactifs (ANDRA).

BIOCLIM 2003c. Deliverable D8a: Development of the rule-based downscaling methodology for BIOCLIM Workpackage 3. Agence Nationale pour la Gestion des Dechets Radioactifs (ANDRA).

BIOCLIM 2003d. Deliverable D8b: Development of the physical/statistical downscaling methodology and application to climate model CLIMBER for BIOCLIM Workpackage 3. Agence Nationale pour la Gestion des Dechets Radioactifs (ANDRA).

BRACONNOT, P., OTTO-BLIESNER, B., HARRISON, S., JOUSSAUME, S., PETERCHMITT, J. Y., ABE-OUCHI, A., CRUCIFIX, M., DRIESSCHAERT, E., FICHEFET, T., HEWITT, C. D., KAGEYAMA, M., KITOH, A., LAINE, A., LOUTRE, M. F., MARTI, O., MERKEL, U., RAMSTEIN, G., VALDES, P., WEBER, S. L., YU, Y. & ZHAO, Y. 2007. Results of PMIP2 coupled simulations of the Mid-Holocene and Last Glacial Maximum - Part 1: experiments and large-scale features. *Climate of the Past,* 3**,** 261-277.

BRANDEFELT, J., NÄSLUND, J.-O., ZHANG, Q. & HARTIKAINEN, J. 2013. The potential for cold climate and permafrost in Forsmark in the next 60,000 years. TR-13-04*,* Svensk Kärnbränslehantering AB.

BRANDEFELT, J. & NÄSLUND, J. O. 2014. Timing of future glacial inception. *In:* HAEBERLI, W. & WHITEMAN, C. (eds.) *Snow and Ice-Related Hazards, Risks, and Disasters.* Oxford, UK: Elsevier.

BROECKER, W. S. 1998. Paleocean circulation during the last deglaciation: A bipolar seesaw? *Paleoceanography,* 13**,** 119-121.

BROECKER, W. S. 2006. Was the Younger Dryas triggered by a flood? *Science,* 312**,** 1146-1148.

CHARBIT, S., PAILLARD, D. & RAMSTEIN, G. 2008. Amount of CO_2 emissions irreversibly leading to the total melting of Greenland. *Geophysical Research Letters,* 35. CIAIS, P., SABINE, C., BALA, G., BOPP, L., BROVKIN, V., CANADELL, J., CHHABRAM, A., DEFRIES, R., GALLOWAY, J., HEIMANN, M., JONES, C., LE QUERE, C., MYNENI, R. B., PIAO, S. & THORNTON, P. 2013. Carbon and Other Biogeochemical Cycles. *In:* STOCKER, T. F., QIN, D., PLATTNER, G. K., TIGNOR,

M., ALLEN, S. K., BOSCHUNG, J., NAUELS, A., XIA, Y., BEX, V. & MIDGLEY, P. M. (eds.) *Climate Change 2013: The Physical Science Basis. Contribution of Working Group I to the Fifth Assessment Report of the Intergovernmental Panel on Climate Change.* Cambridge, UK and New York, USA: Cambridge University Press.

CLARK, P. U., SHAKUN, J. D., MARCOTT, S. A., MIX, A. C., EBY, M., KULP, S., LEVERMANN, A., MILNE, G. A., PFISTER, P. L., SANTER, B. D., SCHRAG, D. P., SOLOMON, S., STOCKER, T. F., STRAUSS, B. H., WEAVER, A. J., WINKELMANN, R., ARCHER, D., BARD, E., GOLDNER, A., LAMBECK, K., PIERREHUMBERT, R. T. & PLATTNER, G. K. 2016. Consequences of twenty-first-century policy for multi-millennial climate and sea-level change. *Nature Climate Change,* 6**,** 360-369.

CLAYTON, K. 1994. Glaciation of the British Isles: An Approach Seeking to Determine the Role of Glaciation in Landform Development over the Last Million Years. *Nirex Safety Studies Report NSS/R337***,** Available from Radioactive Waste Management Limited, UK.

COCHELIN, A. S. B., MYSAK, L. A. & WANG, Z. M. 2006. Simulation of long-term future climate changes with the green McGill paleoclimate model: The next glacial inception. *Climatic Change, 79***,** 381-401.

COLBOURN, G., RIDGWELL, A. & LENTON, T. 2015. The time scale of the silicate weathering negative feedback on atmospheric CO_2. *Global Biogeochemical Cycles, 29***,** 583-596.

COLLEONI, F., WEKERLE, C., NASLUND, J. O., BRANDEFELT, J. & MASINA, S. 2016. Constraint on the penultimate glacial maximum Northern Hemisphere ice topography (approximate to 140 kyrs BP). *Quaternary Science Reviews, 137***,** 97-112.

COLLINS, M., KNUTTI, R., ARBLASTER, J. M., DUFRESNE, J. L., FICHEFET, T., FRIEDLINGSTEIN, P., GAO, X., GUTOWSKI, W. J., JOHNS, T., KRINNER, G., SHONGWE, M., TEBALDI, C., WEAVER, A. & WEHNER, M. 2013. Long-term climate change: projections, commitments and irreversibility. *In:* STOCKER, T. F., QIN, D., PLATTNER, G. K., TIGNOR, M., ALLEN, S. K., BOSCHUNG, J., NAUELS, A., XIA, Y., BEX, V. & MIDGLEY, P. M. (eds.) *Climate Change 2013: The Physical Science Basis. Contribution of Working Group I to the Fifth Assessment Report of the Intergovernmental Panel on Climate Change.* Cambridge, UK and New York, NY, USA: Cambridge University Press.

COX, P. M., HUNTINGFORD, C. & WILLIAMSON, M. S. 2018. Emergent constraint on equilibrium climate sensitivity from global temperature variability. *Nature, 553***,** 319-+.

DANSGAARD, W., JOHNSEN, S. J., CLAUSEN, H. B., DAHLJENSEN, D., GUNDESTRUP, N. S., HAMMER, C. U., HVIDBERG, C. S., STEFFENSEN, J. P., SVEINBJORNSDOTTIR, A. E., JOUZEL, J. & BOND, G. 1993. Evidence for General Instability of Past Climate from a 250-Kyr Ice-Core Record. *Nature, 364***,** 218-220.

DECONTO, R. M. & POLLARD, D. 2016. Contribution of Antarctica to past and future sea-level rise. *Nature,* 531**,** 591-597.

DLUGOKENCKY, E. & TANS, P. 2018. *In:* NOAA/ESRL (ed.).

DOWSETT, H. J., DOLAN, A., ROWLEY, D., MOUCHA, R., FORTE, A. M., MITROVICA, J. X., POUND, M., SALZMANN, U., ROBINSON, M., CHANDLER, M., FOLEY, K. & HAYWOOD, A. 2016. The PRISM4 (mid-Piacenzian) paleoenvironmental reconstruction. *Climate of the Past,* 12**,** 1519-1538.

EBY, M., ZICKFELD, K., MONTENEGRO, A., ARCHER, D., MEISSNER, K. J. & WEAVER, A. J. 2009. Lifetime of anthropogenic climate change: millennial time scales of potential CO_2 and surface temperature perturbations. *Journal of Climate,* 22**,** 2501-2511.

FRENCH, H. M. 2007. *The Periglacial Environment,* Chichester, UK, John Wiley & Sons.

FRIEDLINGSTEIN, P., COX, P., BETTS, R., BOPP, L., VON BLOH, W., BROVKIN, V., CADULE, P., DONEY, S., EBY, M., FUNG, I., BALA, G., JOHN, J., JONES, C., JOOS, F., KATO, T., KAWAMIYA, M., KNORR, W., LINDSAY, K., MATTHEWS, H. D., RADDATZ, T., RAYNER, P., REICK, C., ROECKNER, E., SCHNITZLER, K. G., SCHNUR, R., STRASSMANN, K., WEAVER, A. J., YOSHIKAWA, C. & ZENG, N. 2006. Climate-carbon cycle feedback analysis: Results from the C^4MIP model intercomparison. *Journal of Climate,* 19**,** 3337-3353.

GANOPOLSKI, A. & BROVKIN, V. 2017. Simulation of climate, ice sheets and CO_2 evolution during the last four glacial cycles with an Earth system model of intermediate complexity. *Climate of the Past,* 13**,** 1695-1716.

GANOPOLSKI, A. & CALOV, R. 2011. The role of orbital forcing, carbon dioxide and regolith in 100 kyr glacial cycles. *Climate of the Past,* 7**,** 1415-1425.

GANOPOLSKI, A., WINKELMANN, R. & SCHELLNHUBER, H. J. 2016. Critical insolation-CO_2 relation for diagnosing past and future glacial inception. *Nature,* 529**,** 200-203.

GOLLEDGE, N. R., KELLER, E. D., GOMEZ, N., NAUGHTEN, K. A., BERNALES, J., TRUSEL, L. D. & EDWARDS, T. L. 2019. Global environmental consequences of twenty-first-century ice-sheet melt. *Nature,* 566**,** 65-+.

GREVE, R. 2000. On the response of the Greenland ice sheet to greenhouse climate change. *Climatic Change,* 46**,** 289-303.

HARTIKAINEN, J., KOUHIA, R. & WALLROTH, T. 2010. Permafrost simulations at Forsmark using a numerical 2D thermo-hydro-chemical model. SKB report TR-09-17*,* Svensk Kärnbränslehantering AB.

HAYWOOD, A. M., DOWSETT, H. J., DOLAN, A. M., ROWLEY, D., ABE-OUCHI, A., OTTO-BLIESNER, B., CHANDLER, M. A., HUNTER, S. J., LUNT, D. J., POUND, M. & SALZMANN, U. 2016. The Pliocene Model Intercomparison Project (PlioMIP) Phase 2: scientific objectives and experimental design. *Climate of the Past,* 12**,** 663-675.

HUYBRECHTS, P. 2010. Vulnerability of an underground radioactive waste repository in northern Belgium to glaciotectonic and glaciofluvial activity during the next 1 million years. Report 10/01*,* Departement Geografie VUB.

HUYBRECHTS, P. & DE WOLDE, J. 1999. The dynamic response of the Greenland and Antarctic ice sheets to multiple-century climatic warming. *Journal of Climate,* 12**,** 2169-2188.

HUYBRECHTS, P., GOELZER, H., JANSSENS, I., DRIESSCHAERT, E., FICHEFET, T., GOOSSE, H. & LOUTRE, M. F. 2011. Response of the Greenland and Antarctic Ice Sheets to Multi-Millennial Greenhouse Warming in the Earth System Model of Intermediate Complexity LOVECLIM. *Surveys in Geophysics,* 32**,** 397-416.

IEA 2011. World Energy Outlook. International Energy Agency (IEA).

IEA 2013. World Energy Outlook. International Energy Agency (IEA).

IMBRIE, J. & IMBRIE, J. Z. 1980. Modeling the Climatic Response to Orbital Variations. *Science,* 207**,** 943-953.

IPCC 2013. Climate Change 2013: The Physical Science Basis. Contribution of Working Group I to the Fifth Assessment Report of the Intergovernmental Panel on Climate Change. *In:* STOCKER, T. F., QIN, D., PLATTNER, G. K., TIGNOR, M., ALLEN, S. K., BOSCHUNG, J., NAUELS, A., XIA, Y., BEX, V. & MIDGLEY, P. M. (eds.). Cambridge, UK and New York, USA: Cambridge University Press.

JICKELLS, T. D., AN, Z. S., ANDERSEN, K. K., BAKER, A. R., BERGAMETTI, G., BROOKS, N., CAO, J. J., BOYD, P. W., DUCE, R. A., HUNTER, K. A., KAWAHATA, H., KUBILAY, N., LAROCHE, J., LISS, P. S., MAHOWALD, N., PROSPERO, J. M., RIDGWELL, A. J., TEGEN, I. & TORRES, R. 2005. Global iron connections between desert dust, ocean biogeochemistry, and climate. *Science,* 308**,** 67-71.

JOUZEL, J., BARKOV, N. I., BARNOLA, J. M., BENDER, M., CHAPPELLAZ, J., GENTHON, C., KOTLYAKOV, V. M., LIPENKOV, V., LORIUS, C., PETIT, J. R., RAYNAUD, D., RAISBECK, G., RITZ, C., SOWERS, T., STIEVENARD, M., YIOU, F. & YIOU, P. 1993. Extending the Vostok ice-core record of paleoclimate to the penultimate glacial period. *Nature,* 364**,** 407-412.

JOUZEL, J., MASSON-DELMOTTE, V., CATTANI, O., DREYFUS, G., FALOURD, S., HOFFMANN, G., MINSTER, B., NOUET, J., BARNOLA, J. M., CHAPPELLAZ, J., FISCHER, H., GALLET, J. C., JOHNSEN, S., LEUENBERGER, M., LOULERGUE, L., LUETHI, D., OERTER, H., PARRENIN, F., RAISBECK, G., RAYNAUD, D., SCHILT, A., SCHWANDER, J., SELMO, E., SOUCHEZ, R., SPAHNI, R., STAUFFER,

B., STEFFENSEN, J. P., STENNI, B., STOCKER, T. F., TISON, J. L., WERNER, M. & WOLFF, E. W. 2007. Orbital and millennial Antarctic climate variability over the past 800,000 years. *Science,* 317**,** 793-796.

KAGEYAMA, M. & VALDES, P. J. 2000. Impact of the North American ice-sheet orography on the Last Glacial Maximum eddies and snowfall. *Geophysical Research Letters,* 27**,** 1515-1518.

KJELLSTRÖM, E., STRANDBERG, G., BRANDEFELT, J., NÄSLUND, J.-O., SMITH, B. & WOHLFARTH, B. 2009. Climate conditions in Sweden in a 100,000-year time perspective. TR-09-04*,* Svensk Kärnbränslehantering AB.

KLEMAN, J., FASTOOK, J., EBERT, K., NILSSON, J. & CABALLERO, R. 2013. Pre-LGM Northern Hemisphere ice sheet topography. *Climate of the Past,* 9**,** 2365-2378.

LAMBERT, F., DELMONTE, B., PETIT, J. R., BIGLER, M., KAUFMANN, P. R., HUTTERLI, M. A., STOCKER, T. F., RUTH, U., STEFFENSEN, J. P. & MAGGI, V. 2008. Dust-climate couplings over the past 800,000 years from the EPICA Dome C ice core. *Nature,* 452**,** 616-619.

LASKAR, J., ROBUTEL, P., JOUTEL, F., GASTINEAU, M., CORREIA, A. C. M. & LEVRARD, B. 2004. A long-term numerical solution for the insolation quantities of the Earth. *Astronomy & Astrophysics,* 428**,** 261-285.

LAWRENCE, K. T., HERBERT, T. D., BROWN, C. M., RAYMO, M. E. & HAYWOOD, A. M. 2009. High-amplitude variations in North Atlantic sea surface temperature during the early Pliocene warm period. *Paleoceanography,* 24.

LENTON, T. M. & BRITTON, C. 2006. Enhanced carbonate and silicate weathering accelerates recovery from fossil fuel CO_2 perturbations. *Global Biogeochemical Cycles,* 20.

LI, L., LI, Q. Y., TIAN, J., WANG, P. X., WANG, H. & LIU, Z. H. 2011. A 4-Ma record of thermal evolution in the tropical western Pacific and its implications on climate change. *Earth and Planetary Science Letters,* 309**,** 10-20.

LISIECKI, L. E. & RAYMO, M. E. 2005. A Pliocene-Pleistocene stack of 57 globally distributed benthic $\delta^{18}O$ records. *Paleoceanography,* 20.

LOFVERSTROM, M., CABALLERO, R., NILSSON, J. & KLEMAN, J. 2014. Evolution of the large-scale atmospheric circulation in response to changing ice sheets over the last glacial cycle. *Climate of the Past,* 10**,** 1453-1471.

LORD, N. S. 2017. *Projecting long-term past and future climate change within the context of post-closure performance assessments for disposal of radioactive waste.* PhD Thesis, University of Bristol, UK.

LORD, N. S., CRUCIFIX, M., LUNT, D. J., THORNE, M. C., BOUNCEUR, N., DOWSETT, H., O'BRIEN, C. L. & RIDGWELL, A. 2017. Emulation of long-term changes in global climate: Application to the mid-Pliocene and future. *Climate of the Past,* 13**,** 1539-1571.

LORD, N. S., RIDGWELL, A., THORNE, M. C. & LUNT, D. J. 2015. The 'long tail' of anthropogenic CO_2 decline in the atmosphere and its consequences for post-closure performance assessments for disposal of radioactive wastes. *Mineralogical Magazine,* 79**,** 1613-1623.

LORD, N. S., RIDGWELL, A., THORNE, M. C. & LUNT, D. J. 2016. An impulse response function for the "long tail" of excess atmospheric CO_2 in an Earth system model. *Global Biogeochemical Cycles,* 30**,** 2-17.

LUTHI, D., LE FLOCH, M., BEREITER, B., BLUNIER, T., BARNOLA, J. M., SIEGENTHALER, U., RAYNAUD, D., JOUZEL, J., FISCHER, H., KAWAMURA, K. & STOCKER, T. F. 2008. High-resolution carbon dioxide concentration record 650,000-800,000 years before present. *Nature,* 453**,** 379-382.

MAHOWALD, N., KOHFELD, K., HANSSON, M., BALKANSKI, Y., HARRISON, S. P., PRENTICE, I. C., SCHULZ, M. & RODHE, H. 1999. Dust sources and deposition during the last glacial maximum and current climate: A comparison of model results with paleodata from ice cores and marine sediments. *Journal of Geophysical Research-Atmospheres,* 104**,** 15895-15916.

MCGLADE, C. & EKINS, P. 2015. The geographical distribution of fossil fuels unused when limiting global warming to 2°C. *Nature,* 517**,** 187-190.

MEINSHAUSEN, M., SMITH, S. J., CALVIN, K., DANIEL, J. S., KAINUMA, M. L. T., LAMARQUE, J. F., MATSUMOTO, K., MONTZKA, S. A., RAPER, S. C. B., RIAHI, K., THOMSON, A., VELDERS, G. J. M. & VAN VUUREN, D. P. P. 2011. The RCP greenhouse gas concentrations and their extensions from 1765 to 2300. *Climatic Change,* 109**,** 213-241.

MEISSNER, K. J., MCNEIL, B. I., EBY, M. & WIEBE, E. C. 2012. The importance of the terrestrial weathering feedback for multimillennial coral reef habitat recovery. *Global Biogeochemical Cycles,* 26.

MIKOLAJEWICZ, U., GROGER, M., MAIER-REIMER, E., SCHURGERS, G., VIZCAINO, M. & WINGUTH, A. M. E. 2007. Long-term effects of anthropogenic CO_2 emissions simulated with a complex earth system model. *Climate Dynamics,* 28**,** 599-631.

MODARIA WORKING GROUP 6 2016. Development of a common framework for addressing climate change in post-closure radiological assessment of solid radioactive waste disposal.

MUNHOVEN, G. 2002. Glacial-interglacial changes of continental weathering: estimates of the related CO2 and HCO3- flux variations and their uncertainties. *Global and Planetary Change,* 33**,** 155-176.

NEW, M., HULME, M. & JONES, P. 1999. Representing twentieth-century space-time climate variability. Part I: Development of a 1961-90 mean monthly terrestrial climatology. *Journal of Climate,* 12**,** 829-856.

OTTO-BLIESNER, B. L., BRADY, E. C., CLAUZET, G., TOMAS, R., LEVIS, S. & KOTHAVALA, Z. 2006. Last Glacial Maximum and Holocene climate in CCSM3. *Journal of Climate,* 19**,** 2526-2544.

PAILLARD, D. 1998. The timing of Pleistocene glaciations from a simple multiple-state climate model. *Nature,* 391**,** 378-381.

PATTON, H., HUBBARD, A., ANDREASSEN, K., AURIAC, A., WHITEHOUSE, P. L., STROEVEN, A. P., SHACKLETON, C., WINSBORROW, M., HEYMAN, J. & HALL, A. M. 2017. Deglaciation of the Eurasian ice sheet complex. *Quaternary Science Reviews,* 169**,** 148-172.

PAUSATA, F. S. R., LI, C., WETTSTEIN, J. J., KAGEYAMA, M. & NISANCIOGLU, K. H. 2011. The key role of topography in altering North Atlantic atmospheric circulation during the last glacial period. *Climate of the Past,* 7**,** 1089-1101.

PELTIER, W. R. 2004. Global glacial isostasy and the surface of the ice-age earth: The ice-5G (VM2) model and grace. *Annual Review of Earth and Planetary Sciences,* 32**,** 111-149.

PETIT, J. R., JOUZEL, J., RAYNAUD, D., BARKOV, N. I., BARNOLA, J. M., BASILE, I., BENDER, M., CHAPPELLAZ, J., DAVIS, M., DELAYGUE, G., DELMOTTE, M., KOTLYAKOV, V. M., LEGRAND, M., LIPENKOV, V. Y., LORIUS, C., PEPIN, L., RITZ, C., SALTZMAN, E. & STIEVENARD, M. 1999. Climate and atmospheric history of the past 420,000 years from the Vostok ice core, Antarctica. *Nature,* 399**,** 429-436.

PIMENOFF, N., VENÄLÄINEN, A. & JÄRVINEN, H. 2011. Climate scenarios for Olkiluoto on a time scale of 120,000 years. 2011-04*,* Posiva Oy.

POLLARD, D. & DECONTO, R. M. 2009. Modelling West Antarctic ice sheet growth and collapse through the past five million years. *Nature,* 458**,** 329-332.

RENSSEN, H. & ISARIN, R. F. B. 2001. The two major warming phases of the last deglaciation at ~14.7 and ~11.5 ka cal BP in Europe: climate reconstructions and AGCM experiments. *Global and Planetary Change,* 30**,** 117-153.

RIDGWELL, A. & HARGREAVES, J. C. 2007. Regulation of atmospheric CO_2 by deep-sea sediments in an Earth system model. *Global Biogeochemical Cycles,* 21.

RIDLEY, J. K., HUYBRECHTS, P., GREGORY, J. M. & LOWE, J. A. 2005. Elimination of the Greenland ice sheet in a high CO_2 climate. *Journal of Climate,* 18**,** 3409-3427.

RIGNOT, E., MOUGINOT, J., SCHEUCHL, B., VAN DEN BROEKE, M., VAN WESSEM, M. J. & MORLIGHEM, M. 2019. Four decades of Antarctic Ice Sheet mass balance from 1979-2017. *Proceedings of the National Academy of Sciences of the United States of America,* 116**,** 1095-1103.

ROGNER, H. H. 1997. An assessment of world hydrocarbon resources. *Annual Review of Energy and the Environment,* 22**,** 217-262.

ROGNER, H. H., AGUILERA, R. F., ARCHER, C., BERTANI, R., BHATTACHARYA, S. C., DUSSEAULT, M. B., GAGNON, L., HABERL, H., HOOGWIJK, M., JOHNSON, A., ROGNER, M. L., WAGNER, H. & YAKUSHEV, V. 2012. Chapter 7 - Energy Resources and Potentials. IEA.

SCHENK, F. & WOHLFARTH, B. 2019. The imprint of hemispheric-scale climate transitions on the European climate during the last deglaciation (15.5 ka to 9 ka BP). SKB TR-18-05*,* Svensk Kärnbränslehantering AB.

SCHMIDT, P., LUND, B., NASLUND, J. O. & FASTOOK, J. 2014. Comparing a thermo-mechanical Weichselian Ice Sheet reconstruction to reconstructions based on the sea level equation: aspects of ice configurations and glacial isostatic adjustment. *Solid Earth,* 5**,** 371-388.

SIEGENTHALER, U., STOCKER, T. F., MONNIN, E., LUTHI, D., SCHWANDER, J., STAUFFER, B., RAYNAUD, D., BARNOLA, J. M., FISCHER, H., MASSON-DELMOTTE, V. & JOUZEL, J. 2005. Stable carbon cycle-climate relationship during the late Pleistocene. *Science,* 310**,** 1313-1317.

SINGARAYER, J. S. & VALDES, P. J. 2010. High-latitude climate sensitivity to ice-sheet forcing over the last 120 kyr. *Quaternary Science Reviews,* 29**,** 43-55.

SKB 2010. Climate and climate-related issues for the safety assessment SR-Site. SKB TR-10-49*,* Svensk Kärnbränslehantering AB.

SKB 2011. Long-term safety for the final repository for spent nuclear fuel at Forsmark. Main report of the SR-Site project. SKB Report TR-11-01*,* Svensk Kärnbränslehantering AB.

SMITH, R. S. & GREGORY, J. 2012. The last glacial cycle: transient simulations with an AOGCM. *Climate Dynamics,* 38**,** 1545-1559.

SPRATT, R. M. & LISIECKI, L. E. 2016. A Late Pleistocene sea level stack. *Climate of the Past,* 12**,** 1079-1092.

STENNI, B., MASSON-DELMOTTE, V., SELMO, E., OERTER, H., MEYER, H., ROTHLISBERGER, R., JOUZEL, J., CATTANI, O., FALOURD, S., FISCHER, H., HOFFMANN, G., IACUMIN, P., JOHNSEN, S. J., MINSTER, B. & UDISTI, R. 2010. The deuterium excess records of EPICA Dome C and Dronning Maud Land ice cores (East Antarctica). *Quaternary Science Reviews,* 29**,** 146-159.

STONE, E. J., LUNT, D. J., RUTT, I. C. & HANNA, E. 2010. Investigating the sensitivity of numerical model simulations of the modern state of the Greenland ice-sheet and its future response to climate change. *Cryosphere,* 4**,** 397-417.

SVENDSEN, J. I., ALEXANDERSON, H., ASTAKHOV, V. I., DEMIDOV, I., DOWDESWELL, J. A., FUNDER, S., GATAULLIN, V., HENRIKSEN, M., HJORT, C., HOUMARK-NIELSEN, M., HUBBERTEN, H. W., INGOLFSSON, O., JAKOBSSON, M., KJAER, K. H., LARSEN, E., LOKRANTZ, H., LUNKKA, J. P., LYSA, A., MANGERUD, J., MATIOUCHKOV, A., MURRAY, A., MOLLER, P., NIESSEN, F., NIKOLSKAYA, O., POLYAK, L., SAARNISTO, M., SIEGERT, C., SIEGERT, M. J., SPIELHAGEN, R. F. & STEIN, R. 2004. Late quaternary ice sheet history of northern Eurasia. *Quaternary Science Reviews,* 23**,** 1229-1271.

TEGEN, I. 2003. Modeling the mineral dust aerosol cycle in the climate system. *Quaternary Science Reviews,* 22**,** 1821-1834.

TEXIER, D., DEGNAN, P., LOUTRE, M. F., PAILLARD, D. & THORNE, M. C. 2003. Modelling sequential BIOsphere systems under CLIMate change for radioactive waste disposal. Project BIOCLIM. Proceedings of the 10th International High-Level Waste Management Conference, 30 March – 2 April 2003 Las Vegas, Nevada.

THORNE, M. C., WALKE, R. C. & ROBERTS, D. 2016. Downscaling of climate modelling results for application to potential sites for a geological disposal facility. AMEC/200041/002; QRS-1667A-2, Issue 2*,*

TORRENCE, C. & COMPO, G. P. 1998. A practical guide to wavelet analysis. *Bulletin of the American Meteorological Society,* 79**,** 61-78.

TZEDAKIS, P. C., CHANNELL, J. E. T., HODELL, D. A., KLEIVEN, H. F. & SKINNER, L. C. 2012a. Determining the natural length of the current interglacial. *Nature Geoscience,* 5**,** 138-141.

TZEDAKIS, P. C., CRUCIFIX, M., MITSUI, T. & WOLFF, E. W. 2017. A simple rule to determine which insolation cycles lead to interglacials. *Nature,* 542**,** 427-432.

UCHIKAWA, J. & ZEEBE, R. E. 2008. Influence of terrestrial weathering on ocean acidification and the next glacial inception. *Geophysical Research Letters,* 35.

VASARI, Y. 1999. The history of Dryas octopetala L. in eastern Fennoscandia. *Grana,* 38**,** 250-254.

VRAC, M., MARBAIX, P., PAILLARD, D. & NAVEAU, P. 2007. Non-linear statistical downscaling of present and LGM precipitation and temperatures over Europe. *Climate of the Past,* 3**,** 669-682.

WANG, Y. J., CHENG, H., EDWARDS, R. L., AN, Z. S., WU, J. Y., SHEN, C. C. & DORALE, J. A. 2001. A high-resolution absolute-dated Late Pleistocene monsoon record from Hulu Cave, China. *Science,* 294**,** 2345-2348.

WANG, Y. J., CHENG, H., EDWARDS, R. L., KONG, X. G., SHAO, X. H., CHEN, S. T., WU, J. Y., JIANG, X. Y., WANG, X. F. & AN, Z. S. 2008. Millennial- and orbital-scale changes in the East Asian monsoon over the past 224,000 years. *Nature,* 451**,** 1090-1093.

WARREN, S. G. 1984. Impurities in Snow - Effects on Albedo and Snowmelt Review. *Annals of Glaciology,* 5**,** 177-179.

WHITEHOUSE, P. 2009. Glacial isostatic adjustment and sea-level change. State of the art report. SKB TR-09-11*,* Svensk Kärnbränslehantering AB.

WINKELMANN, R., LEVERMANN, A., RIDGWELL, A. & CALDEIRA, K. 2015. Combustion of available fossil-fuel resources sufficient to eliminate the Antarctic ice sheet. *Science Advances,* 1.

WOLFF, E. W., FISCHER, H. & ROTHLISBERGER, R. 2009. Glacial terminations as southern warmings without northern control. *Nature Geoscience,* 2**,** 206-209.

ZICKFELD, K., EBY, M., WEAVER, A. J., ALEXANDER, K., CRESPIN, E., EDWARDS, N. R., ELISEEV, A. V., FEULNER, G., FICHEFET, T., FOREST, C. E., FRIEDLINGSTEIN, P., GOOSSE, H., HOLDEN, P. B., JOOS, F., KAWAMIYA, M., KICKLIGHTER, D., KIENERT, H., MATSUMOTO, K., MOKHOV, I. I., MONIER, E., OLSEN, S. M., PEDERSEN, J. O. P., PERRETTE, M., PHILIPPON-BERTHIER, G., RIDGWELL, A., SCHLOSSER, A., VON DEIMLING, T. S., SHAFFER, G., SOKOLOV, A., SPAHNI, R., STEINACHER, M., TACHIIRI, K., TOKOS, K. S., YOSHIMORI, M., ZENG, N. & ZHAO, F. 2013. Long-Term Climate Change Commitment and Reversibility: An EMIC Intercomparison. *Journal of Climate,* 26**,** 5782-5809.

LIST OF REPORTS

POSIVA-REPORTS 2019

_____

POSIVA 2019-01   Postglacial Faults In Finland - A Review of PGSdyn Project Results
Antti E.K. Ojala, Jussi Mattila, Timo Ruskeeniemi, Mira Markovaara-Koivisto, Jukka-Pekka Palmu, Nicklas Nordbäck, Antero Lindberg, Raimo Sutinen (Geological Survey of Finland) Ismo Aaltonen, Johanna Savunen (Posiva Oy)
ISBN 978-951-652-271-8
ISSN 2343-4740

POSIVA 2019-02   Surface and Near-Surface Hydrological Modelling in Olkiluoto
Tuomo Karvonen (WaterHope)
ISBN 978-951-652-272-5
ISSN 2343-4740

POSIVA 2019-03   HYDCO Summary Report
Johan Öhman, Kent Hansson (Geosigma), Henry Ahokas, Eero Heikkinen (Pöyry Finland Oy), Antti Poteri, Antti Joutsen (Posiva Oy)
ISBN 978-951-652-273-2
ISSN 2343-4740

POSIVA 2019-04   Modelling Changes in Climate Over the Next 1 Million Years
Dr. Natalie S. Lord, Prof. Dan Lunt (University of Bristol), Dr. Mike Thorne (Mike Thorne and Associates Limited)
ISBN 978-951-652-274-9
ISSN 2343-4740